Graz University of Technology

Institute of Applied Geosciences

Master´s Thesis

3D FRACTURE SYSTEM MODELS BASED ON ACOUSTICAL AND OPTICAL BOREHOLE MEASUREMENTS FOR TUNNELING – EXAMPLES OF KORALM COMPLEX

Katrin Hollersbacher, BSc.

Graz, Austria, November 2014

Advisor

Ao. Univ.-Prof. Dr. Qian Liu

Institute of Applied Geosciences

Deutsche Fassung:
Beschluss der Curricula-Kommission für Bachelor-, Master- und Diplomstudien vom 10.11.2008
Genehmigung des Senates am 1.12.2008

EIDESSTATTLICHE ERKLÄRUNG

Ich erkläre an Eides statt, dass ich die vorliegende Arbeit selbstständig verfasst, andere als die angegebenen Quellen/Hilfsmittel nicht benutzt, und die den benutzten Quellen wörtlich und inhaltlich entnommenen Stellen als solche kenntlich gemacht habe.

Graz, am ..
(Unterschrift)

Englische Fassung:

STATUTORY DECLARATION

I declare that I have authored this thesis independently, that I have not used other than the declared sources / resources, and that I have explicitly marked all material which has been quoted either literally or by content from the used sources.

date ..
(signature)

Acknowledgements

First, I want to thank my Advisor Professor Dr. Qian Liu, who helped and supported me during the planning and development of this thesis. Consequently, he stood by my side with suggestions, enthusiastic encouragement and useful critiques.

Then, I would like to thank all members of the Institute of Applied Geosciences and my fellows for their support in every conceivable way.

Deserving special mention is Mag. Ing. Gerhard Harer, who provided the borehole image data. Without this data, it would never have been possible to write this thesis.

Firmly I would like to thank Dr. Gerald Pischinger for his technical support and assistance.

Additionally, I want to thank my family and my friends for all their endless support and encouragement throughout my study. Finally, my heartfelt thanks belong to my boyfriend Philipp for his suggestions, encouraging help and patience when it was most required.

Abstract

Rock mass characterisation based on the international and regional standards is time consuming as well as cost-intensive. This premise gave the incentive for developing a method to facilitate the process by estimating the rock mass behaviour via three-dimensional fracture models.

To develop such a method, the rock mass surrounding the exploratory tunnel Paierdorf, located on the west side of the Koralm near the Tertiary Lavanttal brittle fault system, was investigated. Intensive desk studies were made to get an idea of the geological and tectonical situation and to identify possible hazards and risks. However, the main part of the investigation was the evaluation of fracture parameters out of borehole images. Further, the subdivision into homogeneous zones based on defined parameters (e.g. lithology, fracture orientation, -size, -intensity, -aperture) was required to model the 3D fracture systems. The modelling process of the simplified mathematical representation of fracture networks and the following block stability analysis were carried out with the computer software FracMan.

In the resulting 3D fracture models, four homogeneous zones were identified. Zone one is located on the west side of the Koralm, near the Lavanttal fault system. The other zones lie to the east of zone one. The unstable blocks of zone one show the highest maximum volume with 9.56 m^3 and the maximum apex with 1.94 m, indicating a poorer rock quality. In contrast, off the Lavanttal fault system higher fracture intensities and trace lengths were discovered. However, due to the good rock quality and the low mechanical effects of the schistosity planes in these zones, the impact on the stability of the blocks is relatively small. In addition, the tectonic setting in the exploratory area was examined. The obtained orientation patterns were compared to the results of neogene tectonic evolution studies. Although the whole area shows remarkable signs of E-W extension, NNW-SSE compression as well as NE-SW compression could be identified. Additionally, orientation patterns signifying the Pliocene compression in E-W direction were found.

In summary, the method proved to be a promising approach for a basic rock mass characterization and could be used as a supplement and support for international and regional standard investigations. Of course, the reliability of the method depends on the quality of the borehole images and geological and geotechnical interpretation. Hopefully the method may proof useful in saving money and time in the initial phase of exploration as well as to improve risk and danger management in the subsurface construction sector.

Kurzfassung

Gebirgscharakterisierungen nach regionalen und internationalen Standards sind meist sehr zeit- und kostenintensiv. Diese Tatsache gab den Ansporn, eine Methode zu finden diese Prozedere zu vereinfachen: die Modellierung von 3D-Trennflächensystemen. Mit Hilfe dieser Modelle soll eine erste Einschätzung des Gebirgsverhaltens möglich werden.

Untersucht wurde das Gebirge im Bereich des Erkundungstunnels Paierdorf. Dieser befindet sich auf der westlichen Seite der Koralm, nahe der tertiären Lavanttal-Störung. Zu Beginn wurde die geologische und tektonische Situation eingeschätzt, um etwaige Gefahrenstellen zu identifizieren. Das Hauptaugenmerk lag jedoch auf der Untersuchung und der Ermittlung wichtiger trennflächenbezogener Parameter und der Lithologie in akustischen und optischen Bohrlochmessungen. Diese Parameter (z.B. Lithologie, Trennflächenorientierung, -größe, -intensität und -öffnung) dienten als Basis für die Einteilung in einzelne homogene Zonen und waren für die Modellierung von großer Bedeutung. Der Prozess dieser vereinfachten mathematischen Darstellung sogenannter Trennflächensysteme und die anschließende Blockstabilitätsanalyse wurden mit dem Computerprogramm FracMan durchgeführt.

Es wurden vier homogene Zonen ermittelt. Die erste Zone befindet sich auf der Westseite der Koralm, nahe der Lavanttal-Störung, alle weiteren Zonen liegen östlich dieser Zone. Zone Eins zeigte mit 9,56 m^3 ein maximales Volumen von instabilen Blöcken und mit 1,94 m einen maximalen Apex. Dies lässt auf schlechtere Gebirgsqualität in Zone Eins schließen. Im Gegensatz dazu wurden entfernt der Lavanttal-Störung höhere Trennflächenintensitäten und -ausbisslängen ermittelt. Auf die Stabilität der Blöcke hatte dies jedoch nur wenig Einfluss. Gute Gebirgsqualität und geringe mechanische Wirkung der Schieferung könnten der Grund dafür sein. Zusätzlich wurde die tektonische Situation analysiert. Die Ergebnisse wurden mit vorhandenen Studien über neogene, tektonische Entwicklungen verglichen. Es zeigte sich, dass das gesamte Gebiet stark von in E-W gerichteter Dehnung gekennzeichnet ist. Außerdem wurden Anzeichen einer Einengung in NNW-SSE und in NE-SW-Richtung festgestellt. Eine weitere Einengung in E-W-Richtung hat zusätzlich ihre Spuren hinterlassen.

Zusammenfassend erwies sich die Gebirgseinschätzung anhand der modellierten 3D-Trennflächensysteme als sehr aussagekräftig. Sie könnte der Erweiterung und Verbesserung standardisierter Gebirgscharakterisierungen dienen und darüber hinaus Zeit und Geld im Bereich der Vorerkundung einsparen. Die Zuverlässigkeit der Methode ist jedoch von qualitativ hochwertigen, akustischen und optischen Bohrlochmessungen sowie ingenieurgeologischer Interpretation abhängig.

Index

1 INTRODUCTION 1

1.1 BACKGROUNDS AND MOTIVATION 1
1.2 PROBLEM DEFINITION 2
1.3 CONTRIBUTION 2
1.4 STRUCTURE OF THIS DOCUMENT 3

2 PRELIMINARIES 5

2.1 FRACTURE DEFINITIONS 5
2.2 ORIENTATION OF FRACTURE PLANES ALONG THE MAIN STRESS AXES 7
2.3 FAULT AND FAULT ZONES 8

3 STUDY SITE 13

3.1 GEOGRAPHICAL SITUATION 13
3.2 GEOLOGICAL SITUATION 14
3.3 TECTONIC EVOLUTION 15
3.4 RELATED WORK – KORALM TUNNEL 18

4 METHODS 23

4.1 COMPUTER PROGRAMS 23
4.1.1 SPHAIRA 23
4.1.2 FRACMAN 24
4.1.3 R 24
4.2 DESK STUDIES 24
4.3 BOREHOLE IMAGE ANALYSIS 25
4.4 DETERMINATION OF THE HOMOGENEOUS ZONES 27
4.5 3D FRACTURE SYSTEM MODELLING 27
4.6 3D FRACTURE SYSTEM MODELLING WITH THE COMPUTER PROGRAM FRACMAN 28
4.7 EVALUATION OF THE RESULTS WITH THE STATISTIC COMPUTER PROGRAM R 29

5 RESULTS 31

5.1 RAW DATA PREPARATION - ENGINEERING DATA CLUSTERING 31
5.1.1 LITHOLOGY 31
5.1.2 DISCONTINUITY ORIENTATION 32
5.2 DATA PROCESSING 39
5.2.1 DISCONTINUITY APERTURES 40
5.2.2 FRACTURE INTENSITY 43
5.2.3 TRACE LENGTH 48
5.3 DATA EVALUATION 50
5.3.1 CLASSIFICATION OF HOMOGENEOUS ZONES 50
5.3.2 FRACMAN – GENERATION OF 3D FRACTURE SYSTEM MODELS 51
5.4 DATA ANALYSIS 57
5.4.1 STATISTIC COMPUTER SOFTWARE R 57
5.4.2 VOLUME AND APEX DISTRIBUTIONS OF THE ROCK BLOCKS 61

6 DISCUSSION 71

7 CONCLUSION 75

8 APPENDIX 77

8.1 LIST OF FIGURES 77
8.2 LIST OF TABLES 81
8.3 LIST OF REFERENCES 82
8.4 GEOLOGICAL MAP 85

1 Introduction

Contents

1.1 Backgrounds and Motivation
1.2 Problem Definition
1.3 Contribution
1.4 Structure of this Document

1.1 Backgrounds and Motivation

Three-dimensional modelling is becoming more and more important in the field of geological and geotechnical investigation. A reason for this is that we easily obtain three-dimensional access to regions where geological sections are not exposed. To this end, we wanted to model three-dimensional fracture systems of an exploratory region to further improve the field of rock mass characterization. Indeed, it is very helpful to make simplified mathematical representations of three-dimensional fracture systems. We can use them to get a better understanding of the relationship between the fracture patterns and their environment and reduce the need for complex geological investigation techniques. The obtained geological information is helpful for example in hazard and risk management. Further, it is a very new researching area and offers many possibilities for future development.

1.2 Problem Definition

The problem is that rock mass characterization based on the international and regional standards, is time consuming and cost intensive. Thus, the three-dimensional geological access to gain information and carry out these characterizations is not always given. To this end, we wanted to develop a method to estimate the rock mass behaviour based on three-dimensional fracture models. Hence, we used the computer software FracMan to model simplified mathematical representations of the discontinuity systems. A benefit of the program is that it includes techniques for utilizing the orientation, size, intensity and transmissivity of fractures and easily applies three-dimensional access. With our method, we wanted to save valuable time, which could be used to interpret the physical relevance of the produced models in context to the regional geology.

1.3 Contribution

The aim of this work is to generate three-dimensional fracture system models based on borehole images and develop the way of rock mass characterisation. Our exploratory region, the surrounding rock mass of the exploratory tunnel Paierdorf is located on the west side of the Koralm near the Tertiary Lavanttal brittle fault system. First, we built up a picture of the regional geology through intensive desk studies. Therefore, we tried to identify the geological structure of the rock mass completely with its constituent units, boundaries, major features, heterogeneities and uncertainties. A conscientious literature research reduces costs and risks during the geological investigation. We used the collected information to identify geological hazards. Hence, our model should build a basis for a further characterisation of the rock mass behaviour. However, our main investigation step was the analysis of borehole images. The gained results led to a better understanding of the tectonic setting in the area. Afterwards, we investigated and calculated fracture properties like the fracture intensity, because we needed the parameters to divide the rock mass into homogeneous zones. Each zone consists of similar geological setting, lithology, orientation patterns, fracture intensities and sizes. Finally, we created three-dimensional fracture system models of each homogeneous zone and carried out a block stability analysis to characterize the rock mass. Of course, we updated the models during prolonged studies. This thesis presents the results of our latest updated models, which deliver valuable information of the ground and helps to identify common geological hazards and risks. Our results are geotechnical relevant, statistical representative, economically assessable, decisive and meaningful for further development.

1.4 Structure of this Document

From this point on the document is structured as follows. First, the preliminaries should explain the background of this thesis. We try to provide the basic knowledge for the following parts. In the following chapters, we present our study site. Then, we describe the materials and methods used in our work. Afterwards we present, analyse and discuss our results. Finally, we summarize our results and make a conclusion. Now, a more detailed outline of the paragraphs follows.

In chapter 2 we define the appearing discontinuity types. Additionally, we give the explanations of fracture system models to understand our thesis.

Chapter 3 describes the exploratory site, with their geographical, topographical, geological and tectonical setting. Subsequently, a brief introduction of the Koralm tunnel project will be given.

In chapter 4 we give a literature review and announce the applied computer software programs. Furthermore we give detailed information how we investigated the fracture key values, which are important parameters for the modelling. We also provide the theoretical background to understand the results section.

Chapter 5 presents, evaluates and analyses our results. Further, we describe the set up and the outcome of our experimental approach. Actually, all results are presented in the conducted order.

In chapter 6 we discuss and interpret the gained results and outcome. Therefore, we will compare the results with each other and try to signify similarities and differences between the distinct homogeneity zones.

Chapter 7 is a conclusion of the major facts to recapitulate this thesis.

2 Preliminaries

Contents

2.1 Fracture Definitions
2.2 Orientation of Fracture Planes along the Main Stress Axes
2.3 Fault and Fault Zones

2.1 Fracture Definitions

At the beginning of our experimental approach we had to be sure about what are fractures and why is their genesis so important? Fractures are cracks, across which the cohesion of the material is lost. They are planes or surfaces of discontinuity that were caused by rupturing of rock material (Park, 2013). The dimension of the discontinuities varies from millimetre to kilometres, depending on the extent of the rupture. Nevertheless, the "macroscopic" fractures, with dimensions much larger than the characteristic grain size of rock are more important for the rock mass behaviour (Mandl, 2005).

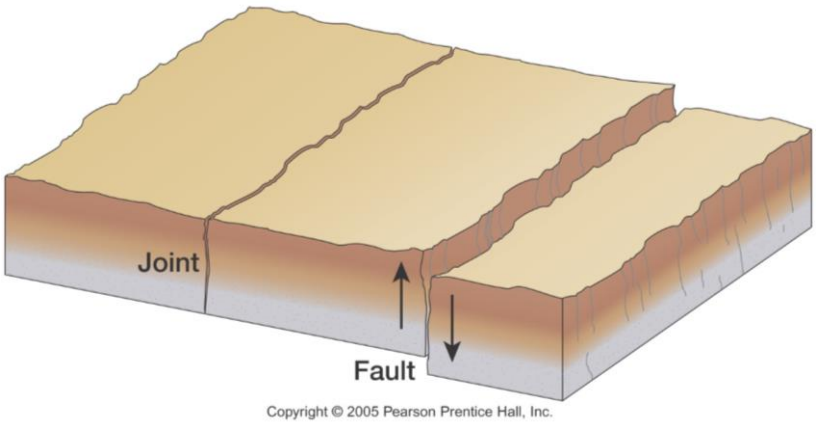

Figure 1: A three-dimensional display of a fault and a joint (Newman, 2007)

What are the most important fracture classes in rock engineering? The most important fracture classes are the joints, the faults, (Figure 1) the slickensides, the bedding planes, the foliation, the schistosity planes and the cleavage. Now, what are the differences

between them? A joint is, in the terminology of the International Society of Rock Mechanics, 2014 a break in a body of rock, which occurs single or more common in a set or system. No “visible” movement occurs parallel to the surface of the discontinuity. Joints can be open or closed and they are sometimes infilled by various materials, such as calcite, quartz or other minerals. In such a case, they are called veins. Latter can be sources of ore minerals and are useful in indicating that fractures are dilatational (Park, 2013).

In comparison to that, a fault is a fracture or fracture zone along which a noticeable displacement, in the dimensions varying from centimetres to kilometres, of the two sides relative to one another parallel to the fracture has occurred (Mandl, 2005). Additionally slickensides are pre-existing failure surfaces, which originate from faulting, landslides or expansion. They are shiny polished surfaces with striation. In a rock mass, slickensides are mostly the weakest elements since strength is often near residual.

Another discontinuity type is the bedding plane, interpreted as contact between sedimentary rocks (Brosch, 2011). Bedding planes are very persistent and may contain clay or other infilled materials, latter leads to a decrease of the shear strength. Their existence can cause a rock break down into thin parallel layers under the action of stresses (Liu, 2014). In contrast, foliation planes are continuous surfaces resulting from the orientation of mineral grains during metamorphism. They can be present as open or almost closed joints. Additionally, schistosity is described as a mode of foliation occurring during the metamorphism of certain rocks because of the parallel alignment of platy and lath-shaped mineral constituents. The changes are results of high temperatures, pressures and deformation. In contrast, cleavage is a fracture caused through extended stress for example during folding. Primarily, it is found in shales and slates. The spacing between two cleavage planes is usually very close (Kurz, 2011). In summary, all kinds of discontinuities affect the strength of rock masses but for rock engineering the bedding planes, foliations and schistosities are most important because they are mechanically very active. Consequently, their observance in engineering, quarrying, mining and geomorphology is necessary (Burg, 2011).

Further, the basis of their formation mechanism is important. Why? Because the allocation of each fracture explains the structural evolution of a region and leads to an understanding of the changes in the regional and local stress fields with time. Thus, the fracture formation mode significantly influences the engineering properties like geometry, permeability, cohesion and roughness (Liu, 2014). Additionally ductile or brittle rock behaviour indicates the location of formation. Almost every rock located near the surface area, where the temperatures and the lithostatic pressures are low, has brittle fractures. In contrast to that, rocks originated in the lower crust show ductile rock behaviours. The main factors that lead to brittle or ductile rock behaviour are the differential stress, the hydrostatic pressure, the temperature, the fluid pressure and the strain rate (Kurz, 2011).

2.2 Orientation of Fracture Planes along the Main Stress Axes

Figure 2 shows the four ways of applying a force to enable a crack to propagate in brittle rocks:

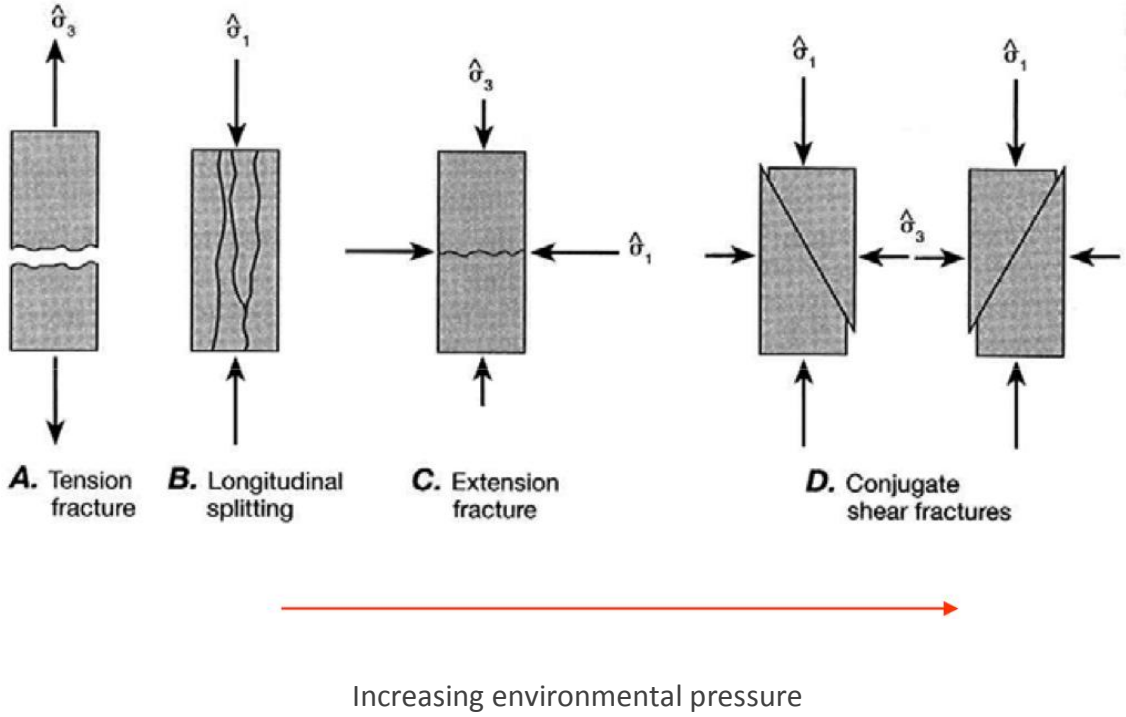

Figure 2: Types of fractures developed during experiments on rocks in the brittle field at increasing environmental pressure from A to D. (Kurz, 2011)

It comes to a tensile failure (Figure 2, A) if a tensile stress effects normal to the plane of a crack. A stable crack configuration (Figure 2, B) appears at low stress conditions in a compressive environment and leads to longitudinal splitting. In contrast, an extension failure (Figure 2, C) occurs if the maximum main stress σ1 acts parallel to the plane of crack in a compressional way (Kurz, 2011). Shear failure occurs (Figure 2, D) if all the main stresses are unequal to cero and the angles of the shear planes are less than 45° (Burg, 2011). To this end, it should be said that extensional fractures are generally more irregular than shear fractures. For instance, they have a greater cohesion because of their interlocking irregularities than shear fractures whose surfaces are often smoothed and polished by shear movement (Liu, 2014).

2.3 Fault and Fault Zones

We have already discussed the differences between important fracture types. Now we will focus on the different kinds of faults. First, why are faults important? Faults generate earthquakes and they build the boundaries between tectonic plates. Furthermore, they deform the earth's surface and affect sedimentation. Mountains arise near fault zones and they influence the fluid transport in the earth's crust. (Martel, 2011) The importance in engineering is given because faults are zones of weakness and difficulties during, for example the excavation of a tunnel, are normally related to fault zones. The weakness, the mechanical and hydraulic heterogeneities of fault rocks are responsible for stability problems during the excavation. Geological hazards in Alpine tunnels often relate to the behaviour of faults at depths, stress induced tensile failure of hard rocks, water inflow in heterogeneous fractured rock masses, plastic shear failure and squeezing of weak rocks (Loew et al., 2010). As example for the influence of faults on the rock mass and excavation, Figure 3 shows the three estimated behaviour types (Daller et al., 1994).

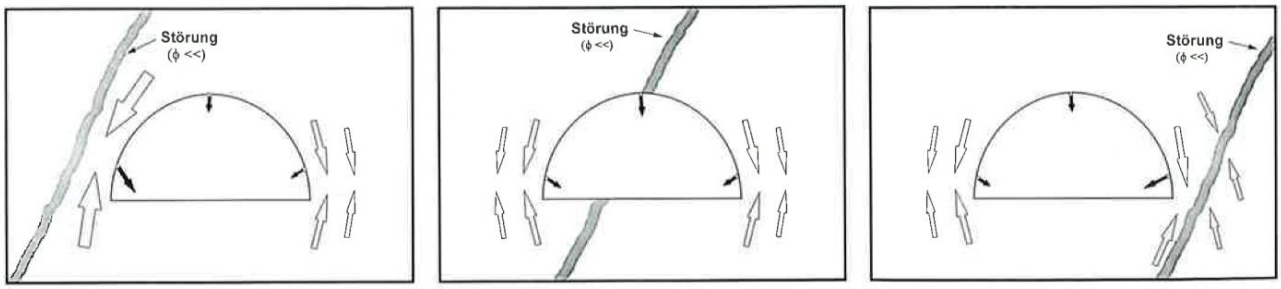

Figure 3: Estimated behaviour: a) tunnel below a fault b) fault crossing the tunnel axis c) tunnel above a fault (Daller et al., 1994)

Let us now have a look on the classification of faults. Based on the orientation of the slip vector, relative to the strike and dip of a fault, there are generally three different kinds of faults. Firstly the strike-slip fault, secondly the dip-slip fault and thirdly the oblique fault. Now, what is the slip vector? The slip is the relative displacement of originally neighbouring points and essentially parallel to the fault. These neighbouring points, also called piercing points, mark the intersection of a line with a fault. Accordingly, the slip vector connects the offset of the piercing points (Figure 4).

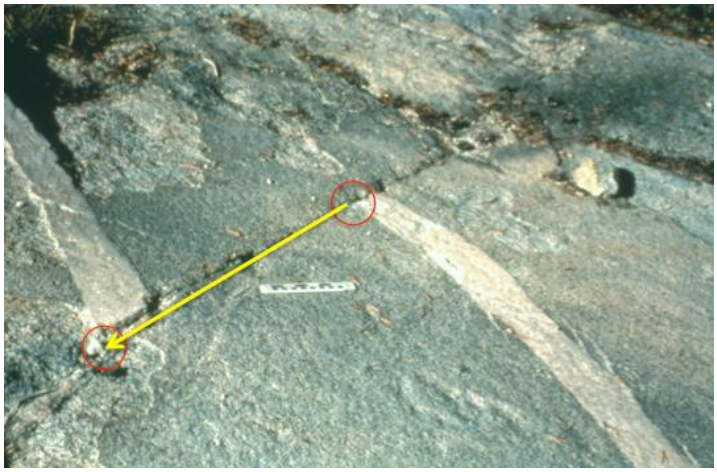

Figure 4: The red circles indicate the piercing points and the yellow arrow shows the offset (slip vector) (Martel, 2011).

Nevertheless, what is a strike slip or transversal fault? The slip-vector of a strike-slip fault is predominantly horizontal and therefore parallel or antiparallel to the line of strike. The sense of slip can be right or left lateral. Subsequently, right lateral means that in the view across a fault, a marker is offset to the right and left lateral means that the marker is offset to the left (Figure 5).

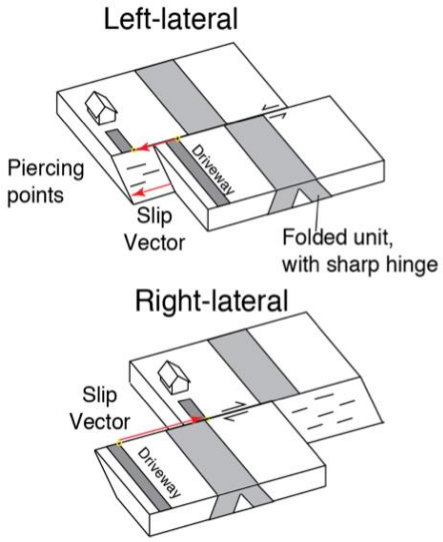

Figure 5: Explanation of a strike-slip fault (Martel, 2011)

Furthermore, how can a dip-slip fault be described? There are two kinds of dip-slip faults, the normal and the reverse or thrust fault. What is the difference between the two of them? It depends on the sense of slip (Figure 6), described as normal if the hanging wall moves down-dip relative to the footwall. These types of faults normally have high dip angles and appear in extensive environments, which is responsible for a high permeability in such fault zones. A reverse (thrust) sense of slip means that the hanging wall moves up-dip relative to the footwall. Thrust faults appear in compressive environments and usually show low dip angles, which may be difficult for engineering treatments. Normally, deeper or rather older rocks thrust over shallower and younger rocks. Additionally it is important to know that the amount and direction of slip can change with time and/or the position along a fault (Martel, 2011).

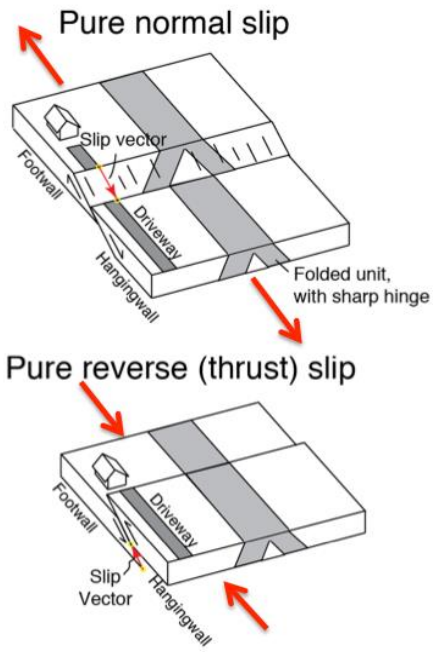

Figure 6: Explanation of dip-slip faults (Martel, 2011)

In contrast, oblique faults (Figure 7) have a strike-slip and dip-slip component with the same magnitude measurable and significant (Burg, 2011). Oblique faults are caused by a combination of shearing and tension or compressional forces (DSSC IRIS, 2014).

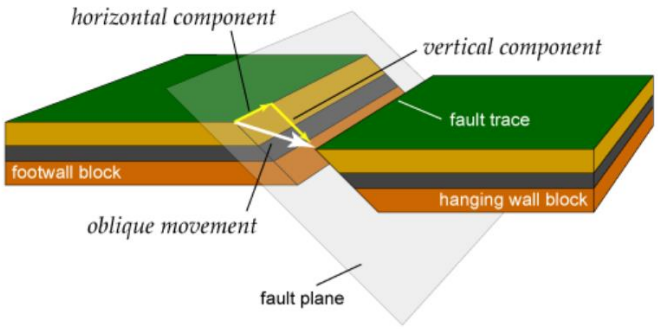

Figure 7: Explanation of an oblique fault (Myers, 2010)

We already discussed the different types of faults but why is their differentiation so important? It is because the sense of slip also indicates the stress distribution and this further leads to the indication of the formation environment. For example, strike-slip faults form at transversal plate boundaries like the San Andreas Fault. In contrast, normal faults form in extensional regimes were tensional stresses pull the earth lithosphere apart, for example along mid ocean ridges. Subsequently, reverse faults form along convergent plate boundaries were horizontal compression appears. Along these boundaries oceanic plates subduct, for example Japan and continental plates collide were the Alps and the Himalayas arise.

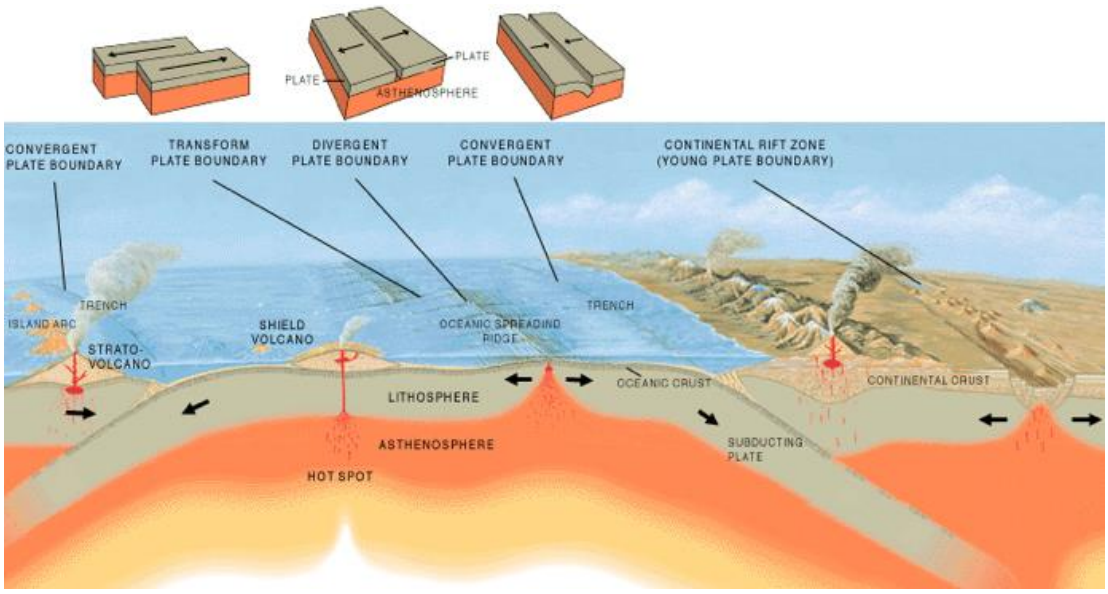

Figure 8: Plate boundaries and their sense of motion illustrating plate tectonic processes (U.S. Geological Survey, 2004)

3 Study Site

Contents

3.1 Geographical Situation
3.2 Geological Situation
3.3 Tectonic Evolution
3.4 Related Work – Koralm Tunnel

3.1 Geographical Situation

Our investigation site (red square in Figure 10), the exploratory tunnel Paierdorf is a part of the Koralm Railway Tunnel situated in the southwest of Graz and the northeast of Klagenfurt. From a topographical point of view, the Koralm is limited by the "Lavanttal Basin" in the west, by the Pack Saddle in the north, by the West Styrian Basin in the east and by the Soboth, a mountain saddle between the Drautal and Sulmtal, in the south.

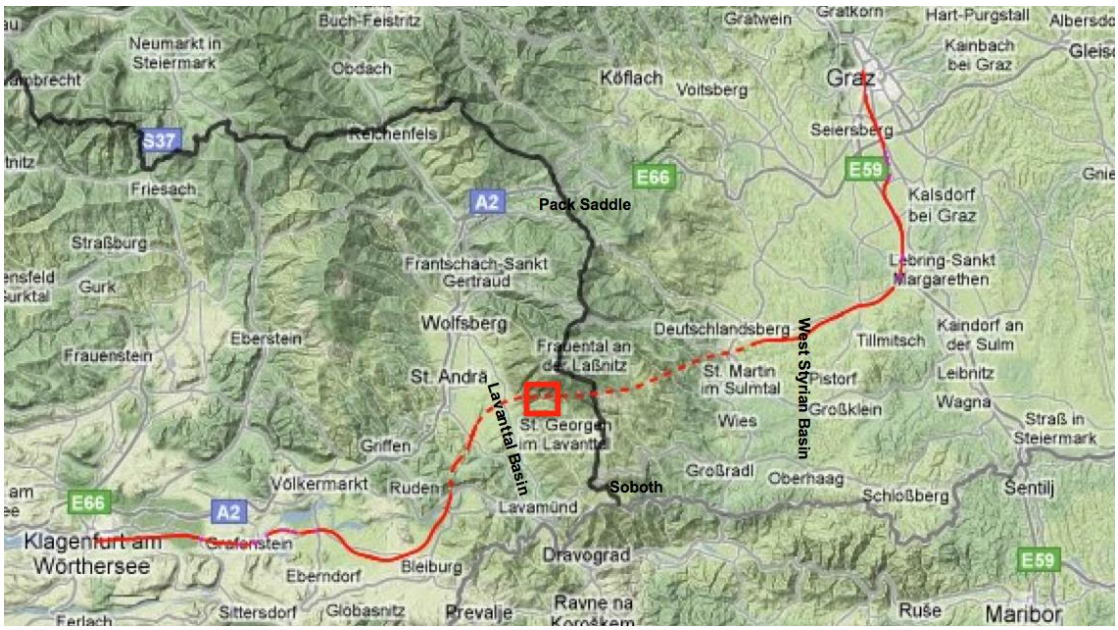

Figure 9: WebMap Koralmbahn Graz–Klagenfurt on a scale of 1:1091958 (red line: Koralm railway; red doted line: Koralm tunnel; red square: exploration region; thick black line: border between Styria and Carinthia; thick grey line in the south: border between Austria and Slovenia; light grey lines: rivers) (Leitner, 2011)

3.2 Geological Situation

Our exploratory region the Koralm (red square in Figure 10) is a mountain range of the Noric Alps and a part of the Koralpe-Wölz high-pressure nappe system, which is a part of the Upper Austroalpine basement nappes and they are a part of the Eastern Alps shown in Figure 10 (Schmid et al., 2004).

The rock mass surrounding the exploratory tunnel Paierdorf predominantly consists of polymetamorphic crystalline basement, originated from Precambrian and Paleozoic sediments (Harer, 2009). The main lithology in the region is composed of different gneiss and micaschist types and subordinate marble, quartzite, amphibolite and eclogite (Harer & Riedmüller, 1999). In the west, the exploratory area is bounded by the NW-SE trending Lavanttal fault system, which has generated the tertiary Lavanttal basin consisting of mainly fine-grained, classic deposits of fluviatile and marine origin (Steidl et al., 2001). The morphological structures found today were formed during Tertiary and Quarternary brittle faulting, weathering and erosion (Harer & Riedmüller, 1999).

To understand the Koralpe-Wölz high-pressure nappe system it is important to understand the orogenic evolution of the Alps, located in south-central Europe, which is discussed in (Schmid et al., 2004) by using a combination of maps and paleogeographical reconstructions. The latest research results show that the Alps are the product of two Orogenies, a Cretaceous followed by a Tertiary one. These Orogenies took place in the Mediterranean region during a convergence of the African and European plates. The Cretaceous one is connected to the closure of an embayment of the Meliata Ocean into Apulia and the Tertiary one is due to the closure of the Alpine Tethys between Apulia and Europe (Schmid et al., 2004).

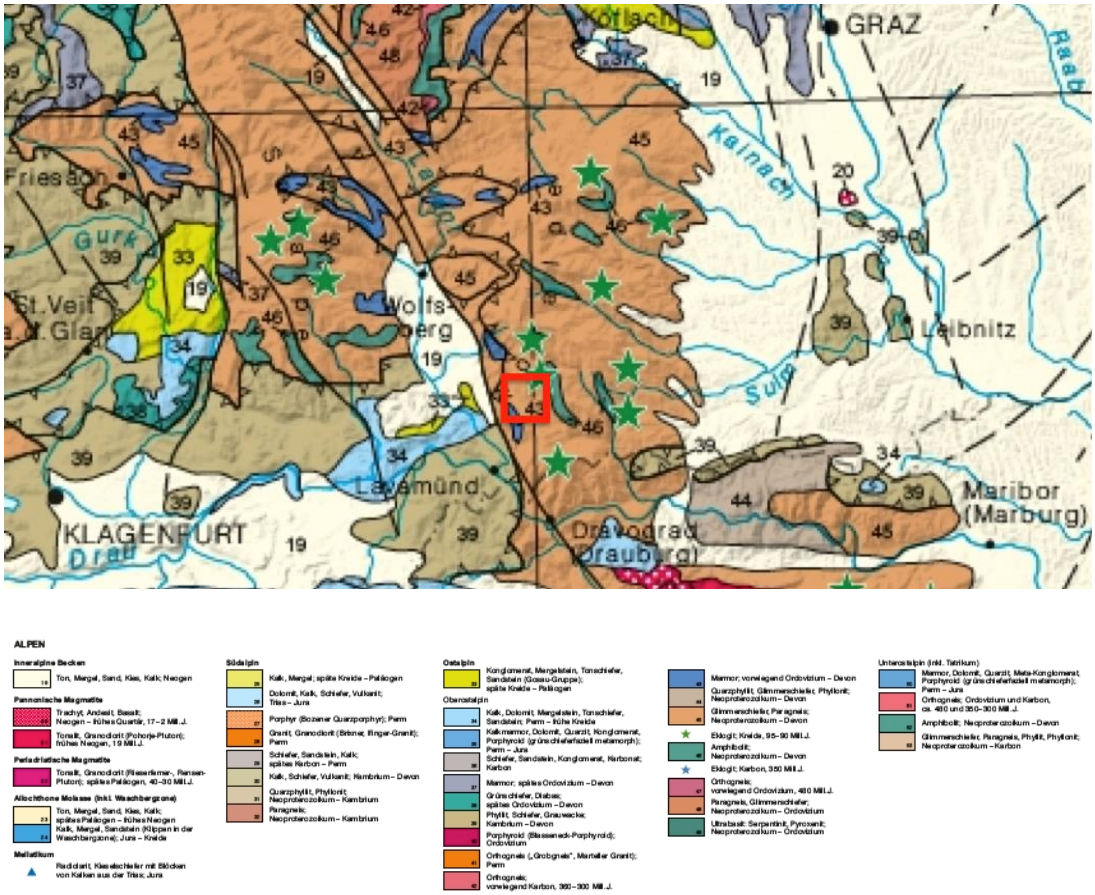

Figure 10: A part of the geological overview map of the republic of Austria enlarged by a factor of 500 000 (Geologische Bundesanstalt, 2014)

3.3 Tectonic Evolution

The final design of the Alpine orogen is mainly characterised by late orogenic strike-slip and extensional faulting during the Miocene (Frisch et al., 2000). After Pischinger et al. 2007 the neogene tectonic evolution in the Miocene and Pliocene could be subdivided into four or precisely six different deformation regimes (D1-1 and D1-2, D2, D3-1 and D3-2, D4). After our completed orientation studies we will assign the results to the regimes. Now a description with the main characteristics of each deformation regime follows.

(D1-1): NNW-SSE compression Karpatian (>18 Ma) and (D1-2) (N)NE-(S)SW extension, late Karpatian (18-17 Ma)

- Activation of WNW-trending fractures in the southern part of the Koralm as dextral strike-slip faults.
- WNW trending troughs filled up with coarse block debris
- W- to WNW trending fractures were reactivated as normal faults, indicating N-S extension
- Assumption: Subsidence and block debris sedimentation

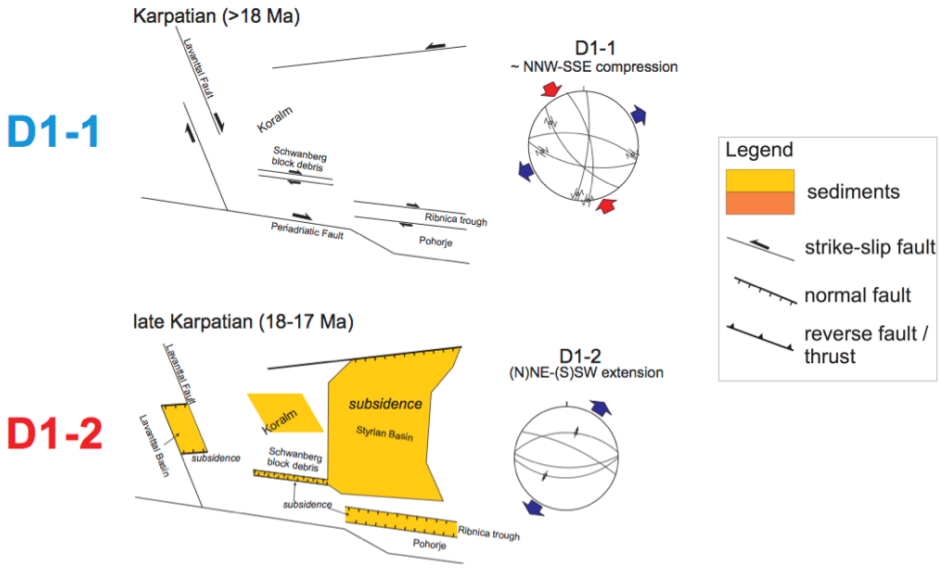

Figure 11: Chart of the deformation regimes D1-1 and D1-2 (Pischinger et al., 2007)

(D2): E-W extension, late Karpatian/early Badenian (17-16 Ma)

- E-W directed extension coincided with uplift of the Sausal Mountains
- Tilting of crustal blocks, divided the Styrian basin into an eastern and western part by the Middle Styrian Swell
- Mainly oblique normal displacement along the Lavanttal fault
- Western Styrian Basin – coarse grained alluvial and coastal deposits
- No Sarmatian (12,7-11,6 Ma) and Pannonian (11,6-7,2 Ma) Sediments during this age!

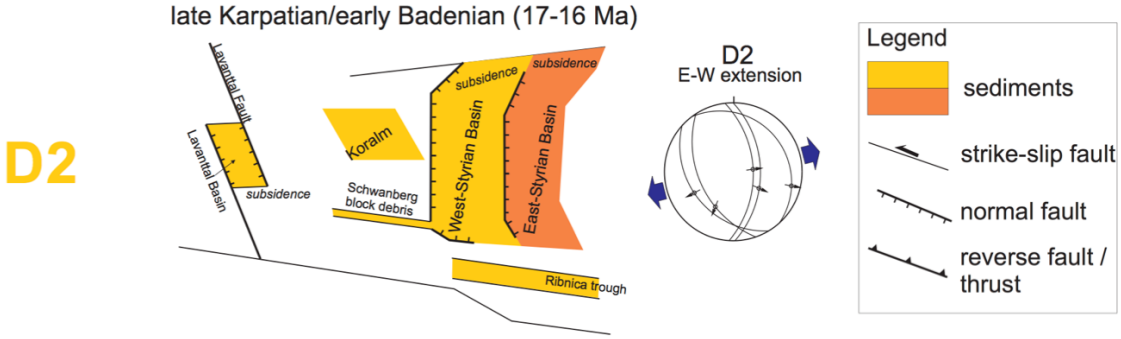

Figure 12: Chart of the deformation regime D2 (Pischinger et al., 2007)

(D3-1): NE-SW compression and (D3-2): NW-SE extension, Sarmatian/Pannonian (13-10 Ma)

- Post-Sarmatian uplift, coinciding with a reactivation of N-trending normal faults (Koralm basement and W-Styrian basin)
- Uplift of the Koralm complex partly together with the W-Styrian basin (approx. 10 Ma, early Pannonian)
- Elevation approx. 600 m
- Associated with E-W extension, N-S striking normal faults
- Shown by: pronounced relief, resulting in enhanced erosion and subsequent deposition (coarse grained clastics in adjacent basins)

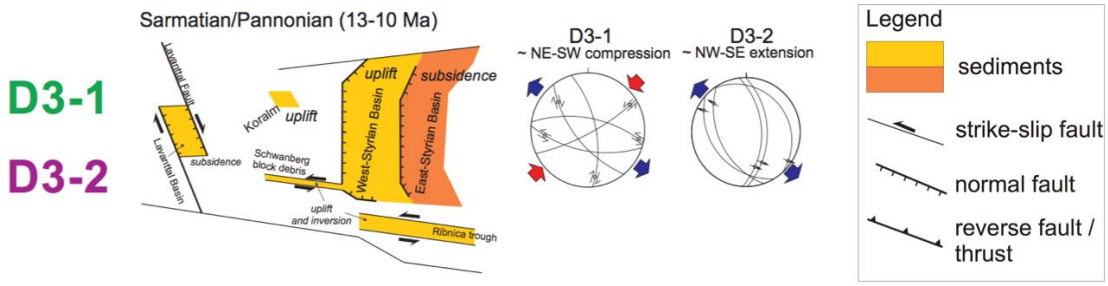

Figure 13: Chart of the deformation regimes D3-1 and D3-2 (Pischinger et al., 2007)

(D4) E-W compression, Pliocene (9-6 Ma)

- Erosion of the Styrian Basin coinciding with basin inversion
- Reactivation of low-angle normal faults along the eastern margin of the Koralm as reverse faults
- Related to E-W directed contraction, indicated by a sub-horizontal E-W orientation of the maximum principal paleostress axes
- Result: Inversion of the Styrian and Lavanttal Basins (Pischinger et al., 2007)

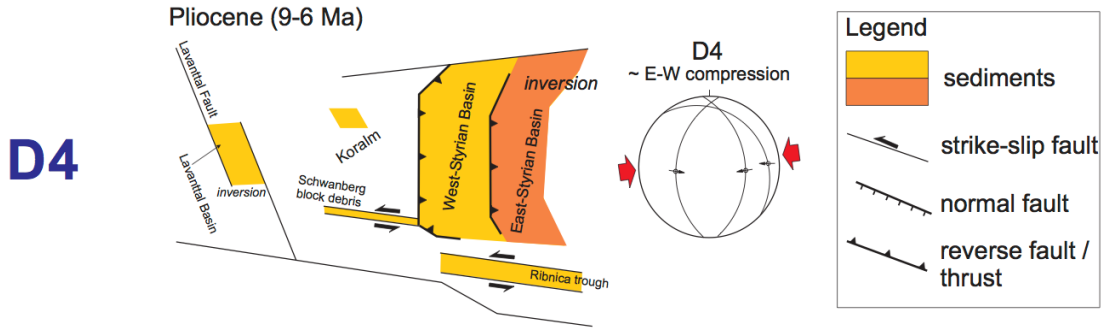

Figure 14: Chart of the deformation regime D4 (Pischinger et al., 2007)

3.4 Related Work – Koralm tunnel

The Koralm railway is part of the Pontebbana axis, the easternmost European crossing of the Alps (Dörrer, et al., 2000). This axis should connect the PAN-European corridor VI from the Baltic countries (e.g. Poland, Czech Republic and Slovakia) via Vienna with Italy and the Mediterranean Sea. In a regional scale, the railway line, with an overall length of approximately 127 km, is a very important link between Graz and Klagenfurt (Harer, 2009). The reason for that is that the travel time will be reduced from present three hours to one hour and further will form the basis for an improved passenger and goods transport (Vavrovsky et al., 2001).

Figure 15: Overview of a part of the Pontebbana axis with the Koralm railway between Graz and Klagenfurt (Harer, 2009)

The planning work for the Koralm railway including the Koralm tunnel started in August 1995 and was conducted by the Austrian Federal Railways, authorised by the Austrian Government. The estimated length of the tunnel system with the double tubes will be around 32,8 km with a maximum overburden of about 1700 m. Consequently, qualified employees precisely had to determine the underground-, groundwater, geological and hydrogeological situation (Harer & Otto, 1999). Preliminary work and fundamental considerations are proposed in Harer & Vavrovsky, 1998 and Harer & Riedmüller, 1999. Essential aspects in preselecting a first route were the geological situation (e.g. fracture and fault systems, lithology and overburden) the length of the tunnel, the safety, the time, the costs and the geotechnical risks (Harer & Riedmüller, 1999). In this case, desk studies combined with a first geological and hydrogeological site investigation were very important (Harer & Otto, 1999). Hence, a first route was selected in 1997 (ÖBB Infrastruktur AG, 2014).

In 1999 the first investigation campaign started. Subsequently, the test field Stullneggbachgraben was geologically and geotechnically characterised to develop and apply modern investigation methods. The examination based on a geological map on a scale of 1:10000 and was created by Riedmüller et al., 1998. The campaign further based on a combination of different tests like two core drillings with structural analysis, in-situ borehole measurements (e.g. dilatometer, water pressure and geophysical tests), laboratory tests carried out by (Skalla, 1998), seismic and geoelectrical tests. All results were presented in CAD and GIS shown in Figure 16 (Harer & Otto, 1999).

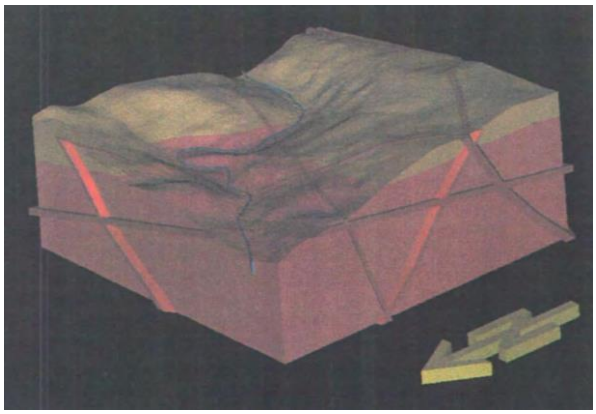

Figure 16: 3D model of the exploratory region "Stullneggbachgraben" (brown: gneiss-micaschist, dark red: "Plattengneis", red: faults, blue: "Stullneggbach) (Harer & Otto, 1999)

In the following years even more geological, hydrogeological and geotechnical ground characterisations for the Koralm area were carried out. Hence, to gain more information about the brittle fault systems on the eastern and western boarder of the Koralm crystalline region, a system of investigation shafts and tunnels with an estimated length of 11 km was constructed in 2003 (Harer, 2009). Particularly, the exploratory tunnel Paierdorf was constructed to obtain information about the western border between the Lavanttal fault system and the central Koralm crystalline region. Additionally, this is the region where our eleven exploratory predrillings, shown in Figure 17, are located. The main reason of this exploratory tunnel and the acoustical and optical borehole measurements, carried out by the Fugro Austria GmbH, was the occurrence of a high amount of marble lenses and consequently the suspected complex hydrogeological situation. The obtained borehole images furthermore built the basis of our structural investigations. Finally, we used the results for the modelling of our 3D fracture systems and a basic rock mass characterisation in the examined region.

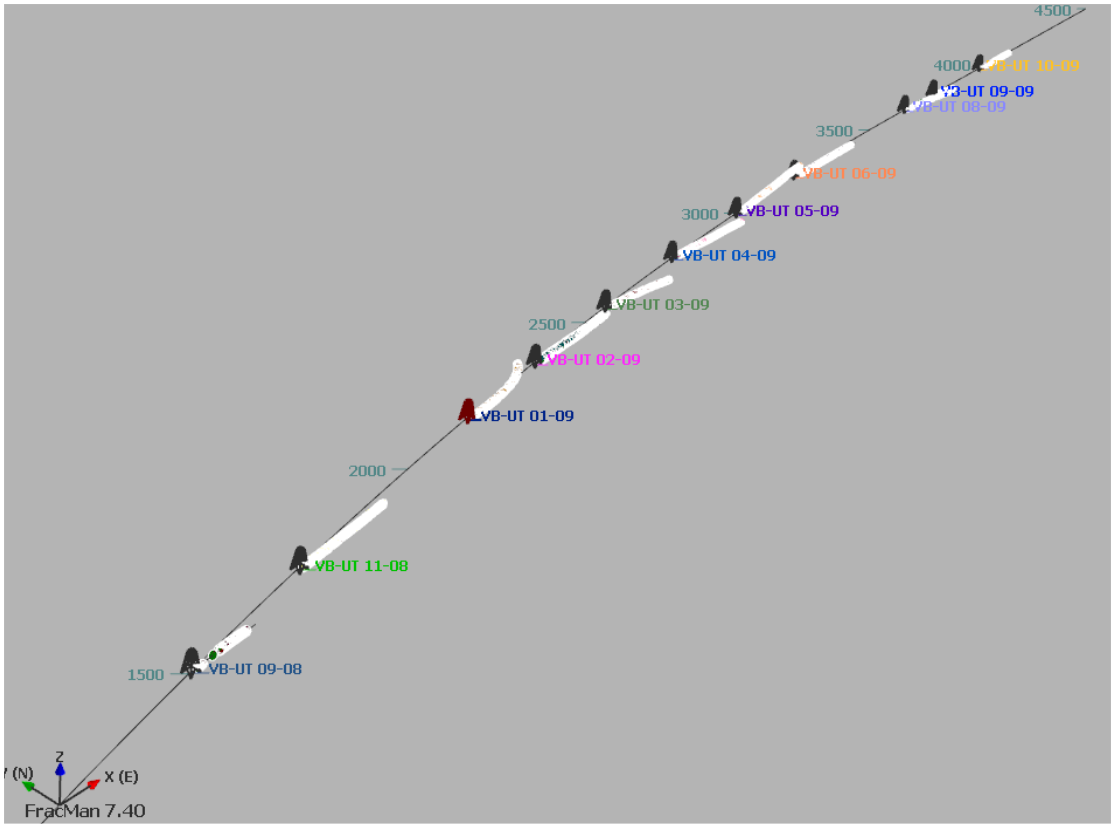

Figure 17: FracMan chart of the axis of the exploratory tunnel Paierdorf with the eleven predrillings from the west to the east.

The following geotechnical investigations included outcrop studies and detailed geological field mappings on a scale of 1:5000. Further, 34 boreholes up to a depth of 650 m and a total length of 6260 m were drilled and studied. Afterwards they were used for in-situ tests (e.g. hydraulic fracture tests, geophysical borehole surveys and hydraulic tests). In several laboratory tests, the mechanical and mineral properties of the core samples were determined (Steidl et al., 2001).

Additional info was gained out of the combined application of different geophysical methods. The combination of seismic and geoelectric measurements shows the lithological boundaries and fault zones down to a depth of 550 m. Hence, with imaging logging systems (e.g. Acoustic televiewer and optical televiewer) a quantitative and qualitative structural analysis and identification of located discontinuities were carried out. This analysis built the basis for the kinematic discontinuity analysis (KDA) and geotechnical rock mass description published in Vanek et al., 2001 and Brosch et al., 2001. The kinematic discontinuity analysis appears to be a promising approach and provided valuable, good quality tectonic data from the subsurface space (Figure 18). The method is particularly recommended in areas with poor surface outcrop conditions.

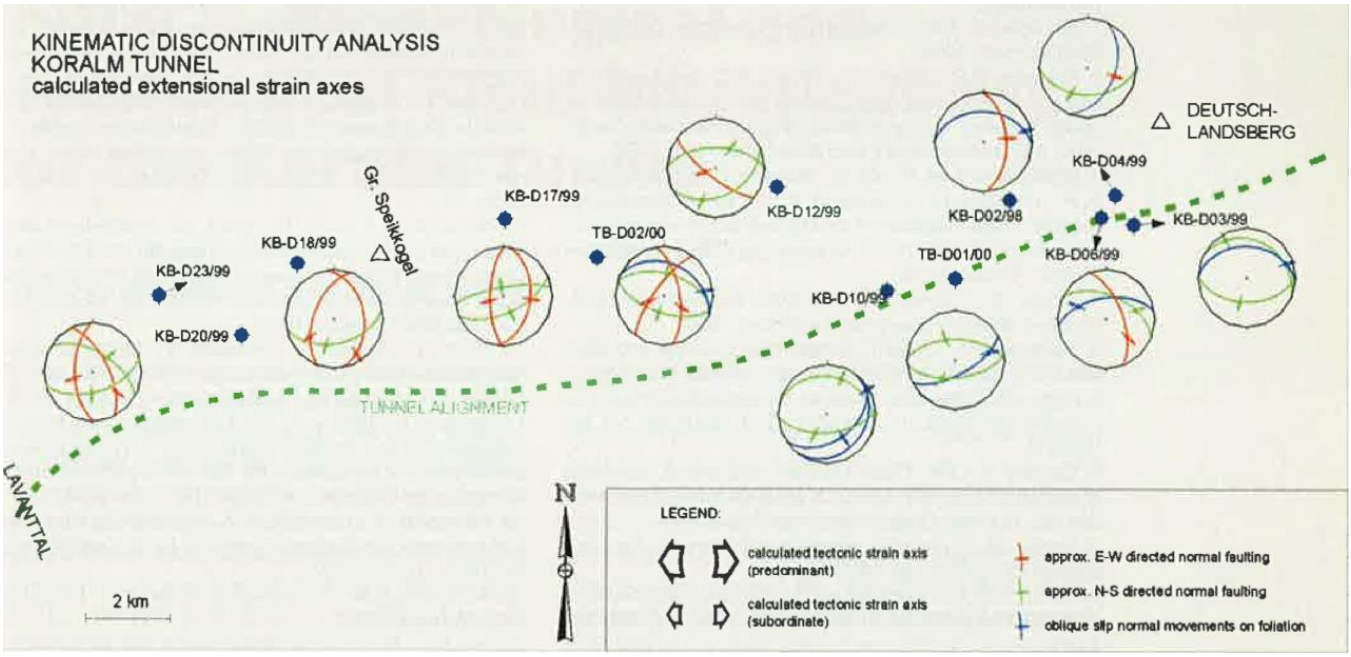

Figure 18: Kinematic Discontinuity Analysis results carried out by Vanek et al., 2001

As an excellent supplement and support of the recorded imaging loggings, applied classical geophysical well log measurements were carried out (e.g. caliper log, gamma-gamma density log, sonic log, etc.) (Dörrer, et al., 2000). The intensive geophysical investigations combined with geological maps render to achieve a basic three-dimensional understanding of the rock mass surrounding the tunnel and show that expensive boreholes were not always important. The boreholes were only located in geophysical determined important areas. A necessity of geophysicists, geologists and engineer's working together to investigate the complex problems in the polymetamorphic ground of the Koralm was given (Aßmann et al., 2001).

Additional investigations were made to estimate the hydrogeological and hydrological situation in the study area. At the beginning, a hydrogeological map to locate water features (e.g. springs and wells) was created to collect relevant data, which may affect the tunnel. Additionally, the water balance of the area was determined and a hydrogeological monitoring (e.g. surface runoff, spring discharge, depth of groundwater level, specific electrical conductivity, in-situ water temperature measurements, pH-measurements and water sample analysis) was carried out (Reichl et al., 2001).

Consequently, a hydraulic and geothermal 3D Finite-Element model was used to estimate the interaction of the planned Koralm tunnel with the regional groundwater system. Aerial hydrological parameters, the mean monthly low run off yield (MoMNq), the monthly run off yield (MQ), the air temperature, the precipitation as well as a 3D geological model and a conceptual hydrogeological model built the basis for the hydraulic-geothermal model. With the model important knowledge about the possible influences of the tunnel on the surface flow, the spring discharge, the drawdown of the groundwater table, short- and long-term tunnel inflow was obtained. In addition, a first approximation of the boundary conditions, the uncertainties of the input parameters, the unsaturated flow and interflow and the hydrogeological condition was made. The modelling results were helpful for following investigations and needed for further models with specific questions (Graf et al., 2001).

Summarized, three major investigation campaigns, performed under high quality standards, were carried out within five years of planning. Each campaign consisted of engineering geological mapping, core drilling and geophysical survey. The results led to an excellent knowledge of the ground conditions in the Koralm exploratory region. In total 100 km^2 of engineering geological mapping, 130 core drillings with a total length of approximately 21,000 m and 60 km of geophysical profiles were carried out. Thus, the investigation results are summarized in the Geographical Information System (GIS) and presented in Figure 19. They have formed the basis for the feasibility study, the route selection, the environmental impact assessment as well as the detailed and tender design. In this case, the large amount of investigations significantly saved time and money and provided sufficient geological data for every project phase (Harer, 2009). Finally, the excavation in section one, located on the east side of the Koralm, started in 2009. Hopefully, the construction work will be concluded and the traffic along the Koralm railway could start in 2023 (ÖBB Infrastruktur AG, 2014).

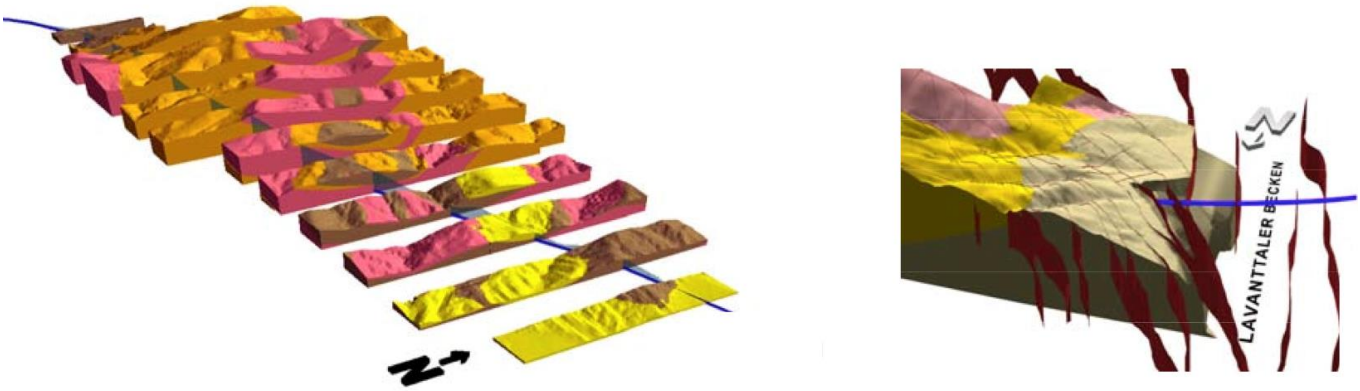

Figure 19: left: Final 3D geological model of the Koralm, right: western, fault bounded transition zone between the crystalline basement and the Tertiary basin (Harer, 2009)

4 Methods

Contents

4.1 Computer Programs
4.2 Desk Studies
4.3 Borehole Image Analysis
4.4 Determination of the Homogeneous Zones
4.5 3D Fracture System Modelling
4.6 3D Fracture System Modelling with the Computer Program FracMan
4.7 Evaluation of the Results with the Statistic Computer Program R

4.1 Computer Programs

4.1.1 Sphaira

The computer software Sphaira is a program to graphically depict orientation data. Hence, the spherical projections should show the respective angular relationship of the orientation data and their statistical distribution. Subsequently, all measured planes are presented as great circles and the measured linear elements are presented as points (Figure 20, left) (Wallbrecher, 1986). Obtained statistical parameters are for example the concentration and the high-density regions (Figure 20, right). The program is useful to identify different discontinuity sets and analyse their important statistic parameters.

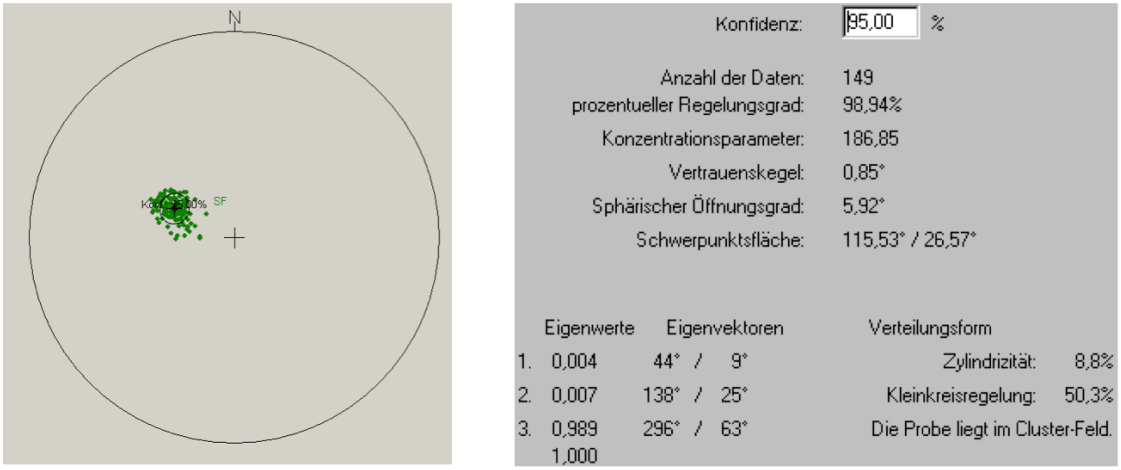

Figure 20: (left) VB-09/08: schistosity plane pole point projection and concentration at a confidence level of 95% (right) according statistic parameters (e.g. confidence level, data number, degree of preferred orientation, concentration, cone of confidence, spherical aperture, high density region, eigenvalue, eigenvectors and the distribution of cylindricity and small circle arrangement)

4.1.2 FracMan

FracMan is a computer program to model the geometry of discrete features, which can be for example faults, fractures, karsts or stratigraphic channels. It is helpful in modelling fractured rock mass, which finds its application in several fields for instance in rock mechanics, underground construction or waste management.

The software provides features to transform raw data into the formats needed for modelling the discrete fractures. Further, it enables a three-dimensional visualization through stochastic fracture pattern simulation. Additionally, an exploration simulation improves the design and interpretation of site characterization programs for the collection of fracture data. The capabilities of data analysis in FracMan include techniques for utilizing the orientation, size, intensity and transmissivity of fractures.

Another benefit of this program is that it has a graphical user interface, which is helpful for the understanding of each modelling step. The control of the user is given by choosing options from a system of drop-down menus. Subsequently, the two and three-dimensional graphical displays afford the users insight into the system of fractures being modelled. Hence, FracMan is a helpful tool for geologists and engineers to simulate three dimensional fracture patterns. Finally, it saves time and this time can be used for the thinking about the physical relevance of the produced models (Golder Associates Inc., 2010).

4.1.3 R

The statistical computing system R is a language and environment for statistical calculations and production of charts (Liu, 2012). Further, the statistical and graphical techniques are for example linear and nonlinear modelling, time-series analyses, classical statistic tests or data clustering. R is helpful to produce well-designed publication-quality plots with mathematical symbols and formulae where needed. Although the user has the full control of the input parameters, the design choices in graphics are low. Hence, it is a very flexible system compared to statistical software like SAS or SPSS, which means that much code written for S runs unaltered under R. Fortunately, R is a free software under the terms of the Free Software Foundation's GNU General Public License in source code form and runs on a wide variety of UNIX platforms and similar systems (Gentleman & Ihaka, 1997).

4.2 Desk Studies

How to start the investigations? It is a mistake to start with a detailed borehole image analysis because the gained information should be seen in context with the overall geology. That is why first, a literature research and preliminary geological interpretation were made to build up a basic geological model of the exploratory area. Therefore, records of constructions (e.g. Koralm tunnel) and occurring structural performance problems (e.g. the Lavanttal tertiary fault system on the west side of the

exploratory area) were analysed. Additionally, reports, geological survey maps, publications and websites e.g. Harer & Riedmüller, 1999 were examined to gain geological and spatial information of the underground to estimate the structural, geological and geotechnical properties of the rock mass. The geological documentation of the 3G-geotechnical group was very important to become detailed information about the lithology in the area. Further, a first assessment of the geological hazards and risks was carried out based on the results of the desk studies. The basic geological model was used as review and was updated several times during the development process (Brosch, 2011).

4.3 Borehole Image Analysis

Borehole images deliver a continuous documentation of the structural profile in the exploratory area. Hence, the acoustic borehole images (ABI) and the optical borehole images (OBI) were used for a quantitative and qualitative evaluation of the located and identified discontinuities.

The fracture parameters (e.g. orientation, fracture intensity and aperture) obtained out of the borehole image analysis built the basis for the fracture system models. First, the optical and acoustical borehole measurements were analysed to do a kind of engineering data clustering based on the orientation and the fracture type. Therefore all fractures were divided into three classes. Firstly the schistosity planes, secondly the joint planes and thirdly the fault planes. Why just three classes? A further differentiation was impossible based on the examined imaging logs. Then, the results of each predrilling were plotted with the computer software Sphaira. After the completed orientation utilisation, a first model of the fracture distributions of one predrilling was generated with the software program FracMan.

The next step was the establishment of the discontinuity apertures. It was a very difficult procedure, because the quality of the imaging logs was very bad at several parts along the predrillings.

Afterwards, the fracture intensity study was conducted. First, the cumulative fracture frequency was determined for each fracture type based on Equation 3. Then, the one-dimensional fracture intensity P_{10} was calculated in Equation 4 Afterwards, the volumetric fracture density P_{32} had to be determined because it is a very important parameter for the modelling with the computer software FracMan. It was impossible to measure P_{32}. Therefore, the volumetric fracture density was evaluated in Equation 6.

The next investigated parameter was the trace length, which was important for the determination of the fracture size, called as equivalent radius. The mathematical description of the equivalent radius is shown in Equation 1. Latter is defined as a simplification of the fracture size. *Re* is the radius of a circular disk with the same area as the fracture. Figure 21 is a simplification of the equivalent radius and shows that all shapes (polygonal, elliptical or circular) have the same surface area. Hence, a comparison of the fractures through just the equivalent radius was possible. The variation of *Re* is described through probabilistic distributions.

$$Re = \sqrt{\frac{Af}{\pi}} \qquad (1)$$

Equation 1: Equivalent radius (Liu, 2012)

Re…equivalent radius
Af…fracture area
π...Pi

In this case, the trace length was established through the examination of the predrilling protocols and the structure tables delivered from the ÖBB. Furthermore, the geological documentation of the 3G-geotechnical group was verified. Afterwards, the equivalent radius was calculated in Equation 5.

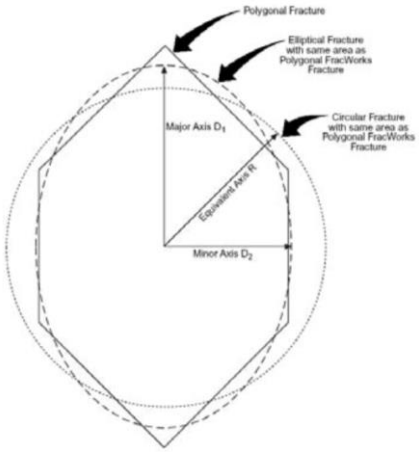

Figure 21: Simplified depiction of the equivalent radius (Liu, 2012)

Another important parameter, which could not be gained out of the imaging borehole investigations, is the termination. It can provide information about fracture shape, size, location and tectonic chronology. Hence, there are two different categories of fracture terminations. First, the fractures those terminate against intact rock (N_R). Second, the fractures those terminate at the intersection with other fractures (N_T) (Liu, 2012). The Termination percentage describes the probability that a fracture will terminate against another fracture and is determined in Equation 2 (Golder Associates Inc., 2010).

$$T_{\%}=N_T/(N_T+N_R) \qquad (2)$$

Equation 2: Termination percentage (Liu, 2012)

$T_{\%}$...Termination percentage
N_T...number of fractures, which terminates against another fracture
N_R...number of fractures, which both terminations occur in rock

4.4 Determination of the Homogeneous Zones

After intensive desk studies, borehole image analysis and calculation of the additional parameters to generate three-dimensional fracture system models with the computer program FracMan, we tried to identify homogeneous zones along the exploratory area. Which parameters characterize a homogeneous zone? For instance, the parameters of the fracture orientation pattern, -size, -intensity, -shape as well as the lithology. Therefore, all results were analysed to identify similarities and differences. Additionally, a geological map of the region, based on previous investigations, was drawn per hand to become a better overview. The map is shown in the Appendix. Subsequently, structurally equal zones were established and the combined parameters of the homogeneous zones are shown in Table 6, Table 7 and Table 8.

4.5 3D Fracture System Modelling

How to generate a 3D-fracture system model based on acoustical and optical borehole image analysis to improve rock mass characterisation? First, a geological model of the exploratory region Paierdorf was designed to build up a picture of the overall geology and tectonic setting. Thus, the design based on detailed desk studies and even more important, the evaluation of fracture parameters out of imaging borehole logs. Then, a geometrical model for the descriptions of fractures and their relation to each other in space was designed. The geometric characteristics of fractures are stochastically described by probabilistic distributions of the location and arrangement in space, the intensity, the orientation, the size, the shape, the termination and further properties of fractures (Golder Associates Inc., 2010). The listed geometric fracture characteristics were applied to a fracture set and accordingly a three-dimensional fracture system was modelled. Additionally, this was made for each fracture in each homogenous zone of the exploratory area Paierdorf. The whole process was repeated for thirty times to gain significant statistical distributions. Then, a rock wedge analysis of each fracture system model was carried out. The outcome was the properties of the stable and unstable blocks of each unit. Finally, the results were utilised to characterise the rock mass in the exploratory region. Now the modelling process of the 3D fracture systems with the computer software FracMan will be described in detail.

4.6 3D Fracture System Modelling with the Computer Program FracMan

To characterise the rock mass of the homogenous zones, 3D fracture system models were generated as follows:

1. A small box region was inserted to simplify the modelling.
2. The first fracture set, with an assumed volumetric fracture density P_{32}* value was generated.
3. A borehole was inserted, to compute the simulated linear intensity in a certain direction P_{10}*.
4. The borehole intersected with a number of fractures. Then P_{10}* was determined in Equation 7.
5. As a linear function of the measured intensity in a certain direction in the field P_{10} (Equation 4), the true intensity P_{32} was established in Equation 6 (Dershowitz & Herda, 1992).
6. That process was repeated for each fracture set in each homogeneous zone.
7. All fracture sets of one zone were generated.
8. A virtual tunnel in the drilling direction was inserted.
9. The geomechanical rock wedge analysis was carried out, based on the intersections of the fracture system model with the tunnel.
10. Real block-assemblages were evaluated through the algorithm developed by (Dershowitz & Carvalho, 1996).
11. The stability analysis of the blocks was conducted by unwrapping of a specific realization of the fracture geometry.
12. The block volume and the apex of the stable and unstable blocks were determined.
13. The whole analysis was repeated thirty times in each zone, to obtain a distribution and results that are more accurate.

4.7 Evaluation of the Results with the Statistic Computer Program R

The results were graphically depicted in a boxplot, which is also known as box-and-whisker-diagram. This way of data representation is convenient in descriptive statistics. Hence, the five important numbers in statistics, which are the minimum, the lower quartile at 25%, the median, the upper quartile at 75% and the maximum, describe the plot (Figure 22). Furthermore, the interquartile range is also the length of the box and the outliers are the values lying outside the whiskers. Finally, the results are presented and analysed in chapter 5 (Liu, 2012; Brosch, 2011).

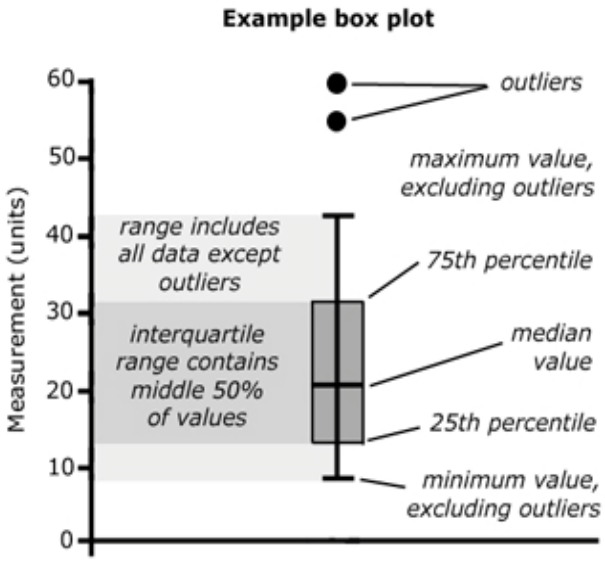

Figure 22: The main features of a boxplot (Hawkins et al.)

5 Results

Contents

5.1 Raw Data Preparation – Engineering Data Clustering
5.2 Data Processing
5.3 Data Evaluation
5.4 Data Analysis

In this chapter, we will describe the main steps of data acquisition. Beginning with the desk studies, continuing with the most important part, the intensive borehole image analysis up to the final modelling processes of the three-dimensional fracture systems and the subsequent analysis of the stable and unstable rock blocks in the investigated area.

5.1 Raw Data Preparation - Engineering Data Clustering

5.1.1 Lithology

The first step was to characterize the rock mass, based on their rock type. Therefore, we analysed the geological documentation of the 3G-geotechnical group, geological maps and literature of the exploratory area. To confirm our assumptions we analysed the optical and acoustical borehole measurements. Table 1 shows the results of our investigation. The exploratory tunnel Paierdorf consists mainly of polymetamorphic crystalline basement. Therefore, different gneiss types and micaschist, with occasional amphibolites, marbles, quartzitic-, cataclasitic-, calcitic- and clay-layers, dominate the lithology.

Table 1: Lithological classification

Predrilling	Depth [m]	Lithology	Length of advance [m]
VB-UT 09/08	1497-1729	schistgneiss, Hbl-gneiss, Grt-amphibolite, marble- and Qtz-bands, cataclastic fault zone	1.7
VB-UT 11/08	1730-2147	Hbl-, Bt- schistgneiss, micaschist, marble	3
VB-UT 01/09	2148-2337	schistgneiss, micaschist, marble, Bt-, Hbl-gneiss, amphibolite	2.35
VB-UT 02/09	2338-2549	Bt-Hbl-, schistgneiss, amphibolite, micaschist, marble	3
VB-UT 03/09	2550-2764	micaschist, Bt-Hbl-, schistgneiss, amphibolite, Cc- and Qtz-bands	3
VB-UT 04/09	2765-2983	micaschist, amphibolite, gneiss, marble, Qtz-bands, folding structure	2.2
VB-UT 05/09	2984-3192	micaschist, schistgneiss, amphibolite, marble, folding structure	2.2
VB-UT 06/09	3193-3623	micaschist, amphibolite, marble, Qtz-bands, quartzite, folding structure	2.2
VB-UT 08/09	3624-3743	micaschist, marble, schistgneiss, amphibolite, intensive folding structure, fault zone	2.6
VB-UT 09/09	3744-3944	marble, micaschist, schistgneiss, intensive folding structure	2.2
VB-UT 10/09	3945-4053	micaschist, dolomite-marble, schistgneiss, Qtz-layers, intensive folding structure	1.7

5.1.2 Discontinuity Orientation

The next step was to divide the rock mass based on their fracture orientations into distinct classes. Therefore, we needed much time to examine every single discontinuity in all boreholes, which have a total length of approximately 2410 meters. In the predrilling records, the discontinuities are represented as sine like curves, in the column STRUKTUR in Figure 23. Hence, the green curves, which define the schistosity are already analysed. The challenge was to evaluate the magenta coloured curves, which were meanwhile labelled as undefined (Figure 23).

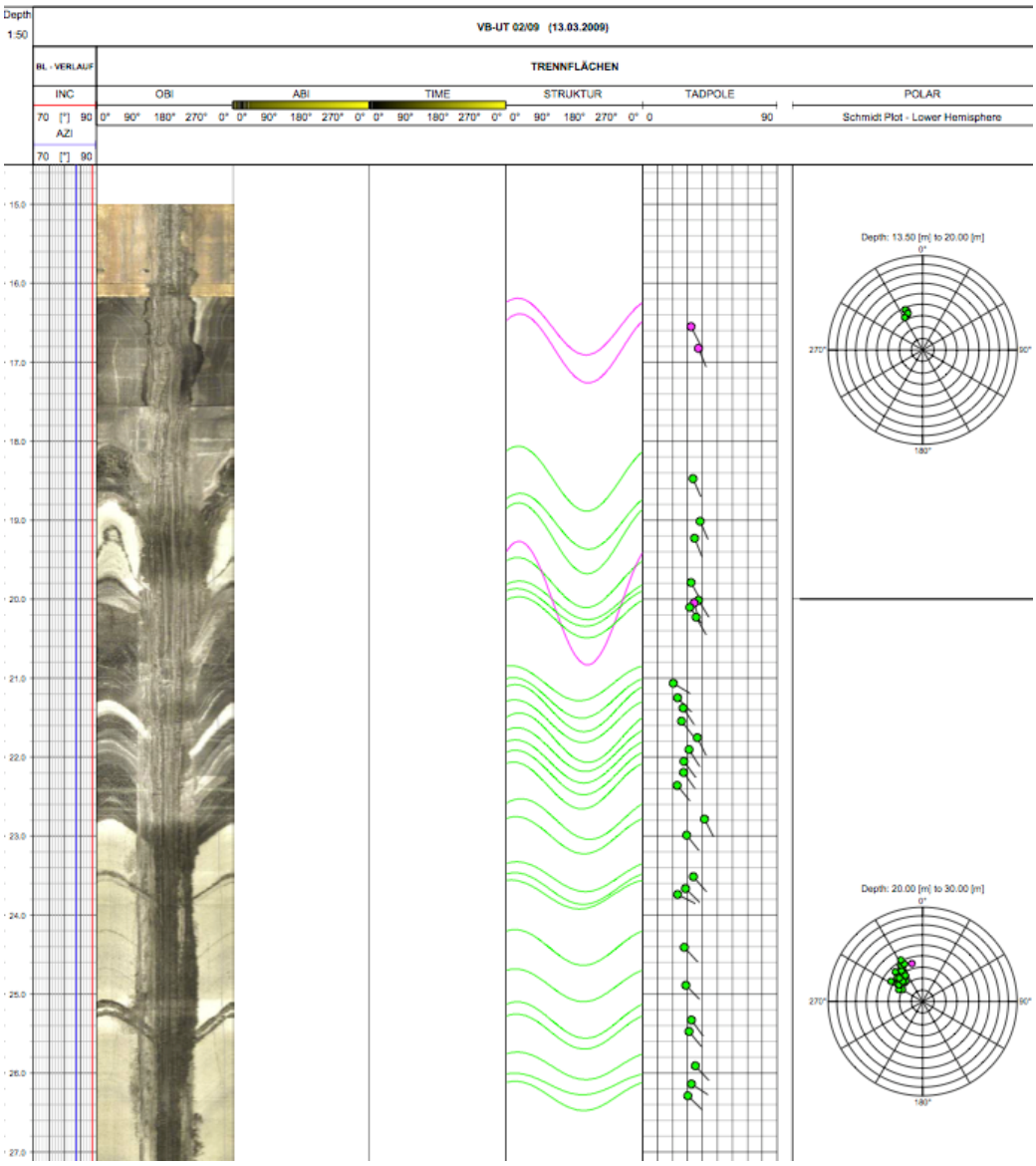

Figure 23: VB-UT 02/09 image of an optical borehole measurement (AZI.: Azimuth (drilling direction refers to geographic north), INC.: Inclination (borehole inclination refers vertically). OBI.: Optical Borehole Imager, ABI.: (Acoustic Borehole Imager), TIME.: ABI, run time, STRUKTUR.: , discontinuities from OBI/ABI, (with reference to the borehole axis, no correction) classification: green: bedding or foliation planes, magenta: indefinite, POLAR: polar diagram (Schmidt net southern hemisphere))

After a first detailed study of the undefined fractures, we compared our results to the results of the geological documentation (Figure 24) of the 3G Geotechnical group. This documentation was made during the construction of the exploratory tunnel Paierdorf. To evaluate and interpret the orientation data, we used the software Sphaira.

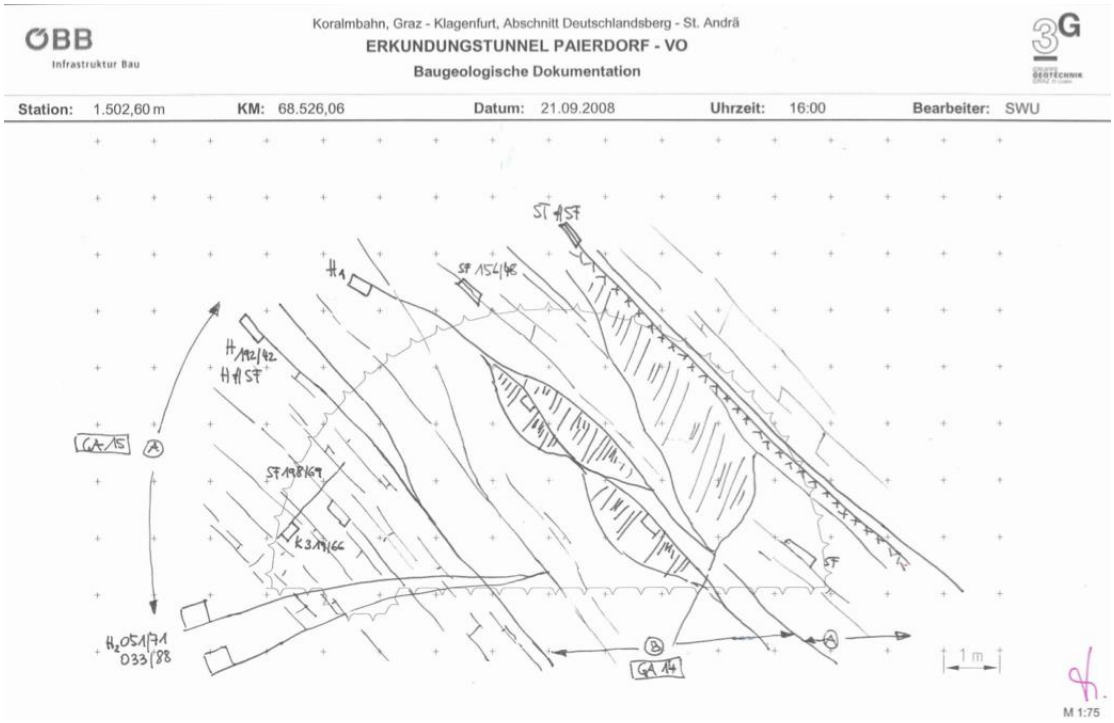

Figure 24: Geological documentation of the 3G geotechnical group in the exploratory tunnel Paierdorf at Station: 1.502,60 m, investigated in predrilling VB-UT09/08, (GA: rock mass type; SF: schistosity; ST: fault; H: slickenside; K: joint)

Figure 25 shows the stereographic plots of the results obtained from the 3G Geotechnical group and our first results in the predrilling VB-UT 01/09. The pole projections indicates a first comparison between them and helped us to ameliorate further investigations.

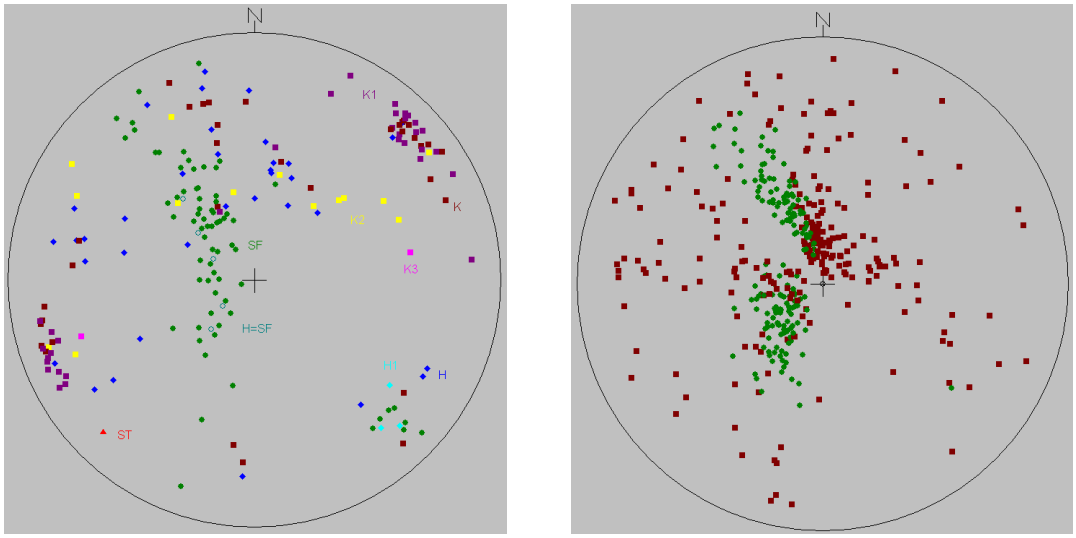

Figure 25: VB-UT 01/09, Stereographic projections (left) the results of the geological documentation of the 3G geotechnical group (green: schistosity, dark red: joints, purple: joint set one, yellow: joint set two, pink: joints set three, dark blue: slickenside, light blue: slickenside 1, bluish green: slickenside is equal to schistosity, light red: faults); (right) our first results (green: schistosity, red: joints)

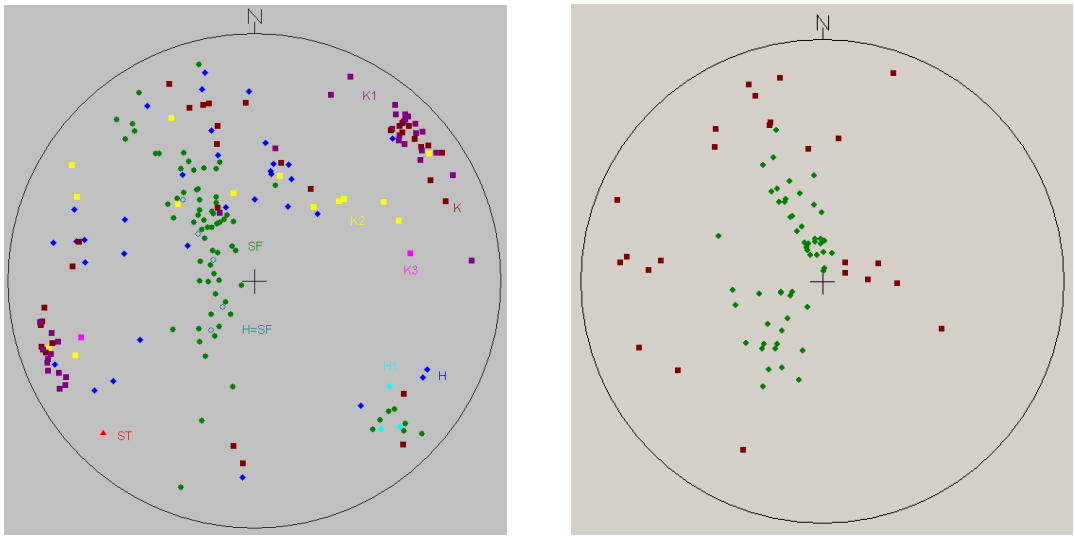

Figure 26: VB-UT 01/09, (left) Fracture pole projection received from the geological documentation of the 3G Geotechnical group (green: schistosity, dark red: joints, purple: joint set one, yellow: joint set two, pink: joints set three, dark blue: slickenside, light blue: slickenside 1, bluish green: slickenside is equal to schistosity, light red: faults); (right) Our fracture pole projection results (green: schistosity, red: joints)

Figure 26 represents our final orientation results in VB-UT 01/09, which we received after repeated processing. Thus, they are compared to the results of the 3G-geotechnical group once again to demonstrate the similarities and the differences between them. Very obvious distinctions in Figure 26 are that the southwest and northwest striking sets are missing and that we have a lower fracture amount along the same length in VB-UT 01/09. To deceive a better overview we compared all pole projections of the predrillings in Figure 27 and the schistosity contour line projections in Figure 28. Accordingly, we can see a shift of the high-density region from an east-southeast to an east-northeast trending concentration of the schistosity planes.

Further, we analysed the results and searched for homogeneous oriented zones. Therefore, VB-UT 09/08 is labelled as zone one because of the missing fracture patterns in the northeast and the southeast. Zone two comprises the predrillings VB-UT 11/08, 01/09, 02/09 and 03/09. All of them have similar fracture and schistosity orientations. Additionally the predrillings VB-UT 04/09, 05/09 and 06/09 belong to zone three and show a southeast trending schistosity and conjugated fracture planes. The last zone is zone four consisting of the predrillings VB-UT 08/09, 09/09 and 10/09 with an east-northeast trending schistosity and conjugated fracture planes in the northeast and southwest. Finally, we displayed the high-density orientation regions of each zone in Figure 29.

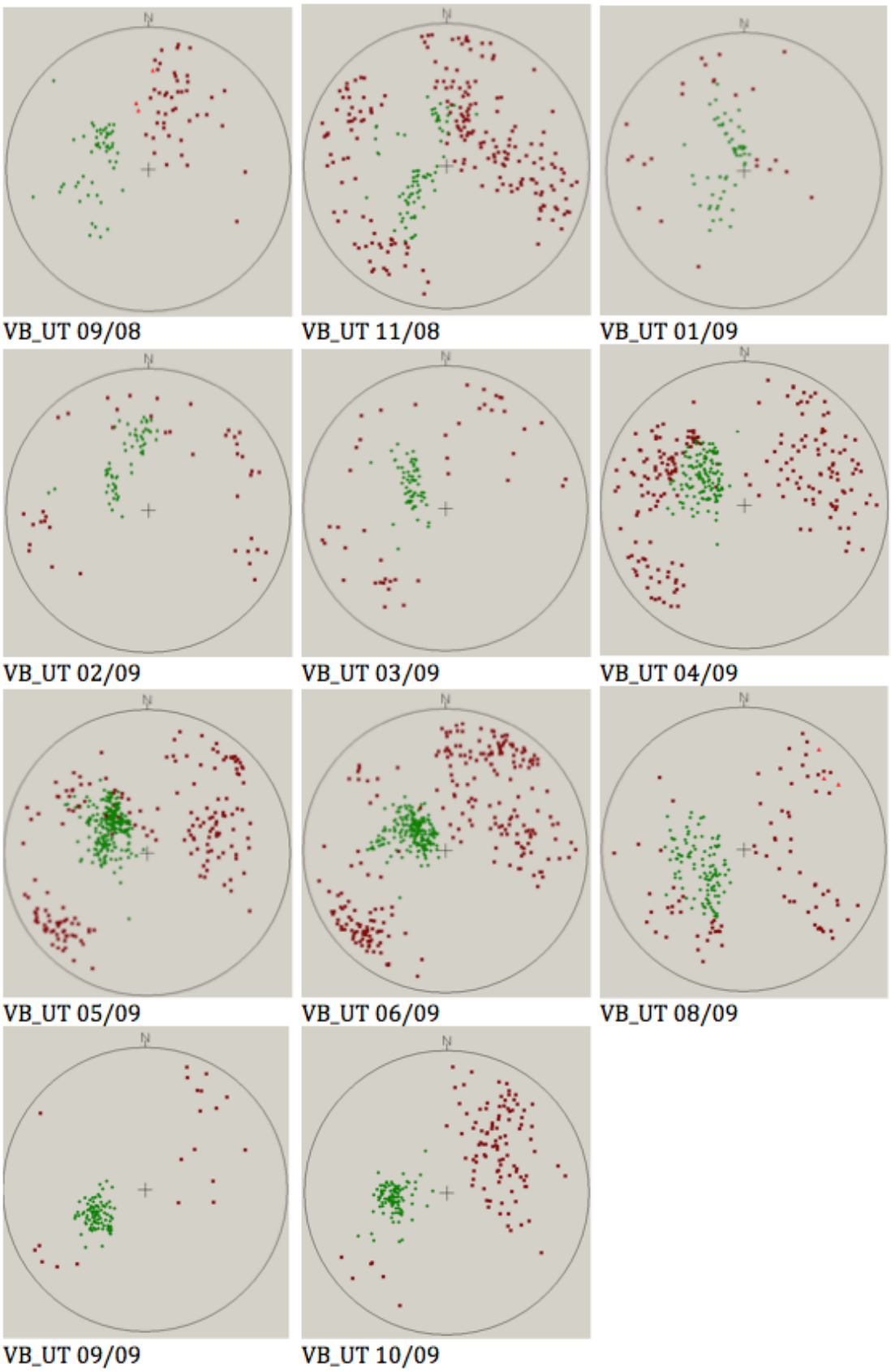

Figure 27: Pole projections of all exploratory predrillings from the west to the east (red: joints, green: schistosity)

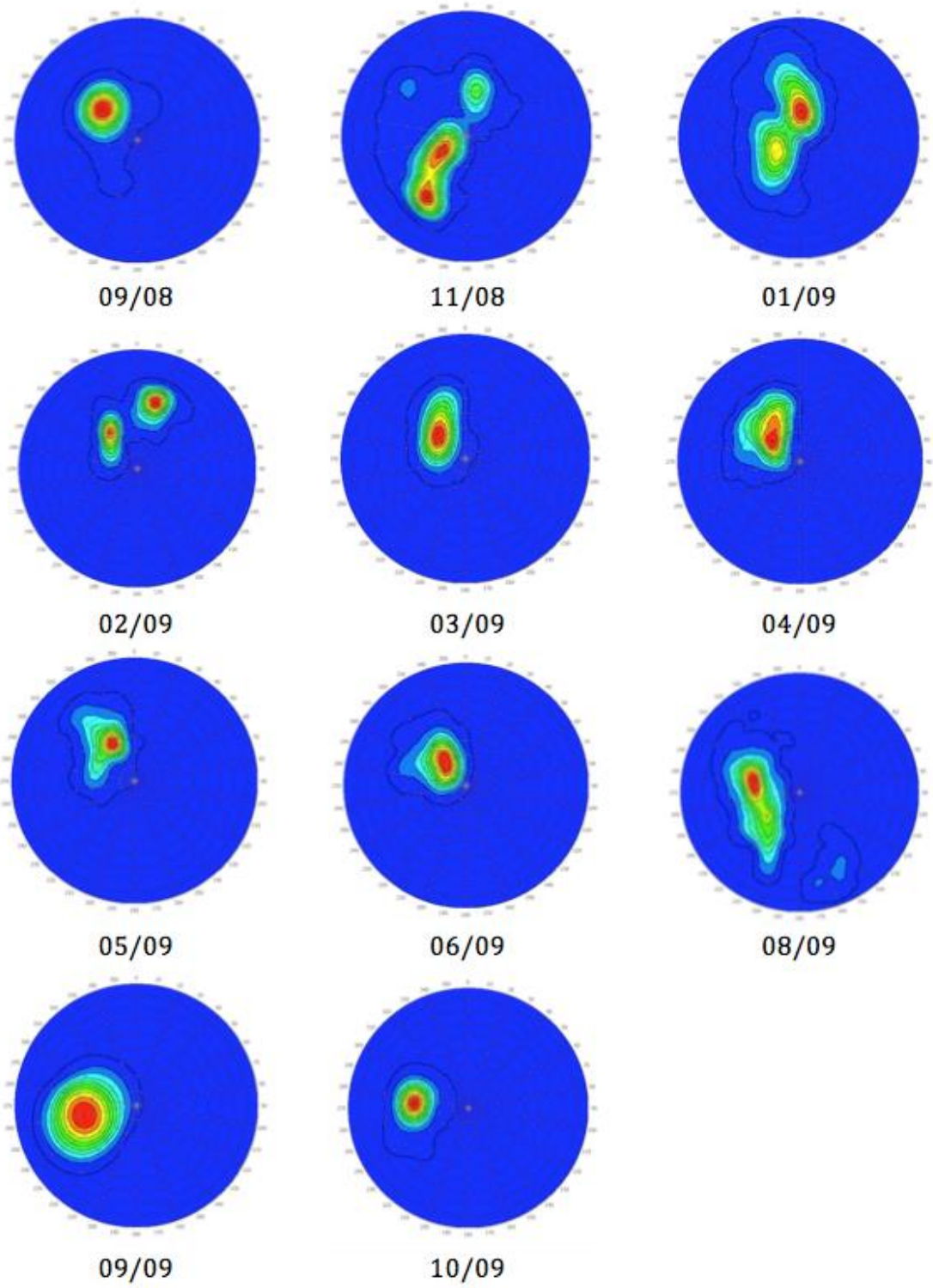

Figure 28: Contour line projections of the schistosity planes in all exploratory predrillings from the west to the east, produced with the software program FracMan.

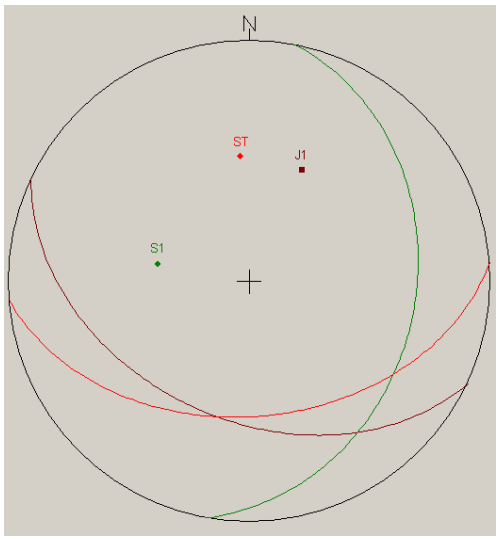

Zone 1

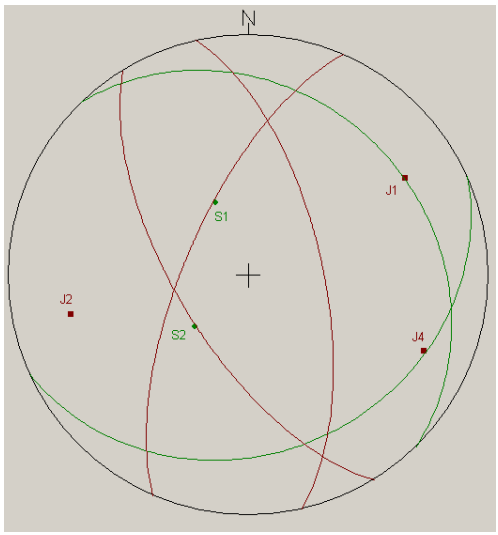

Zone 2

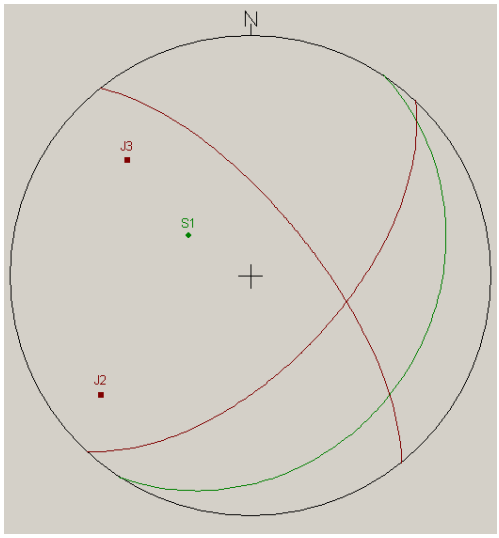

Zone 3

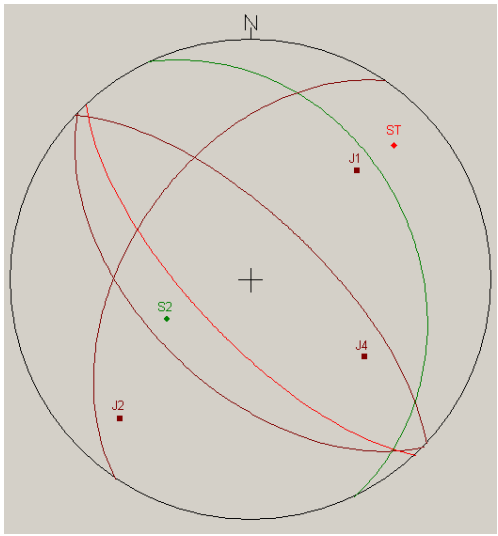

Zone 4

Figure 29: Great circle and pole point projections of the homogeneous oriented zones one to four (dark red: joints, light red: faults, green: schistosity)

Figure 29 shows the Great circle and pole projections of each homogeneous oriented zone. Therefore, the general trends in our exploratory region are:

- Schistosity set trends: Schistosity set one – southeast to east-southeast
  Schistosity set two - northeast
- Joint sets trends: Joint set one – southwest to south-southwest
  Joint set two – northeast to east-northeast
  Joints set three - southeast
  Joint set four – northwest to west-northwest
- Fault set trend: Faults set one - southwest

Now we can assign each homogeneous zone to a tectonic regime, described in chapter 3.3. Therefore, Zone one could be assigned to regime D1-1, zone two and zone 3 to regime D2 and zone four to the regimes D3-1 and D4.

5.2 Data Processing

After our completed fracture orientation studies, we imported the results of each predrilling in FracMan. In short, we inserted the tunnel axis and imported the eleven exploratory predrillings with their corresponding discontinuity planes (Figure 30, Figure 31).

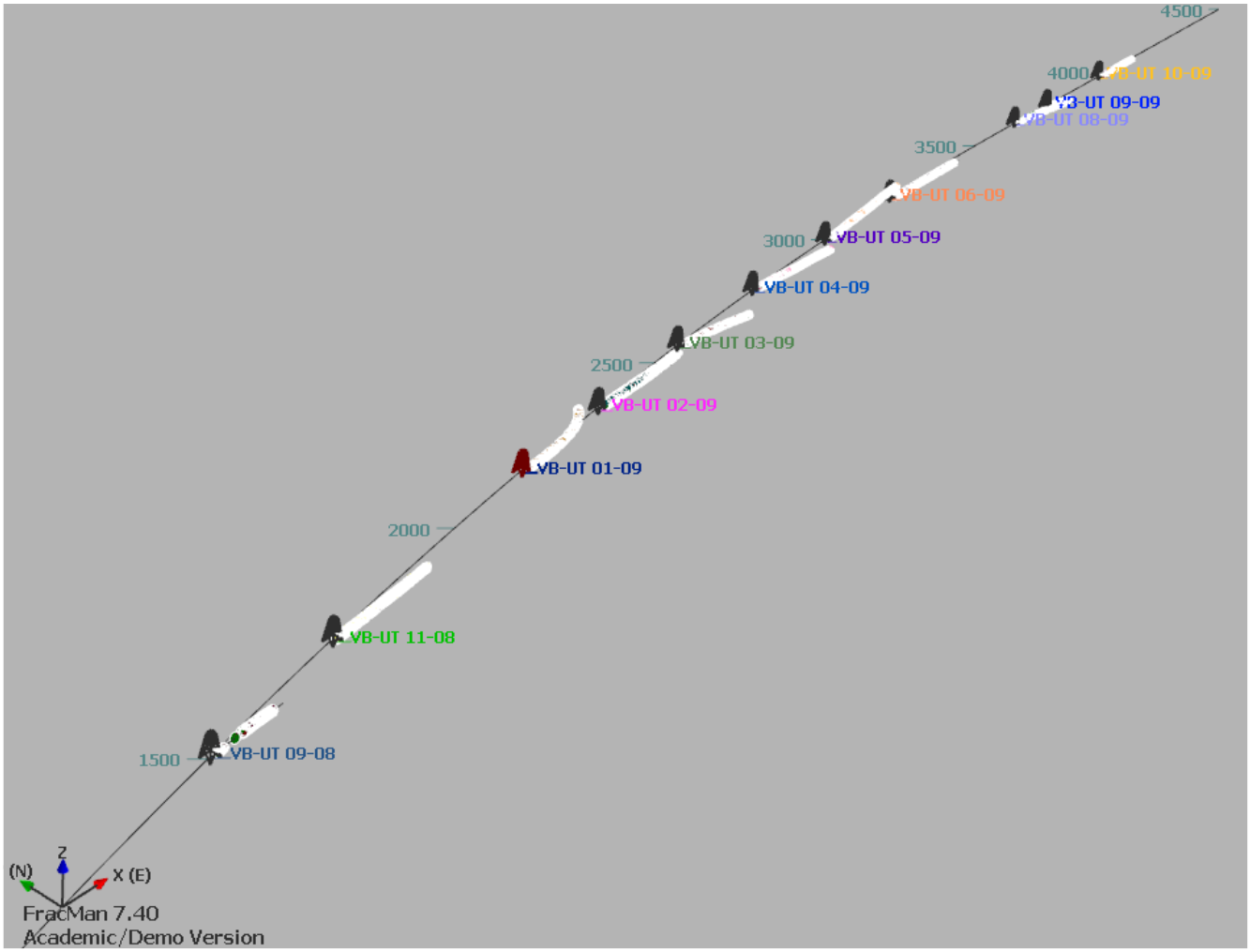

Figure 30: FracMan representation of the tunnel axis with all eleven exploratory predrillings from the west to the east.

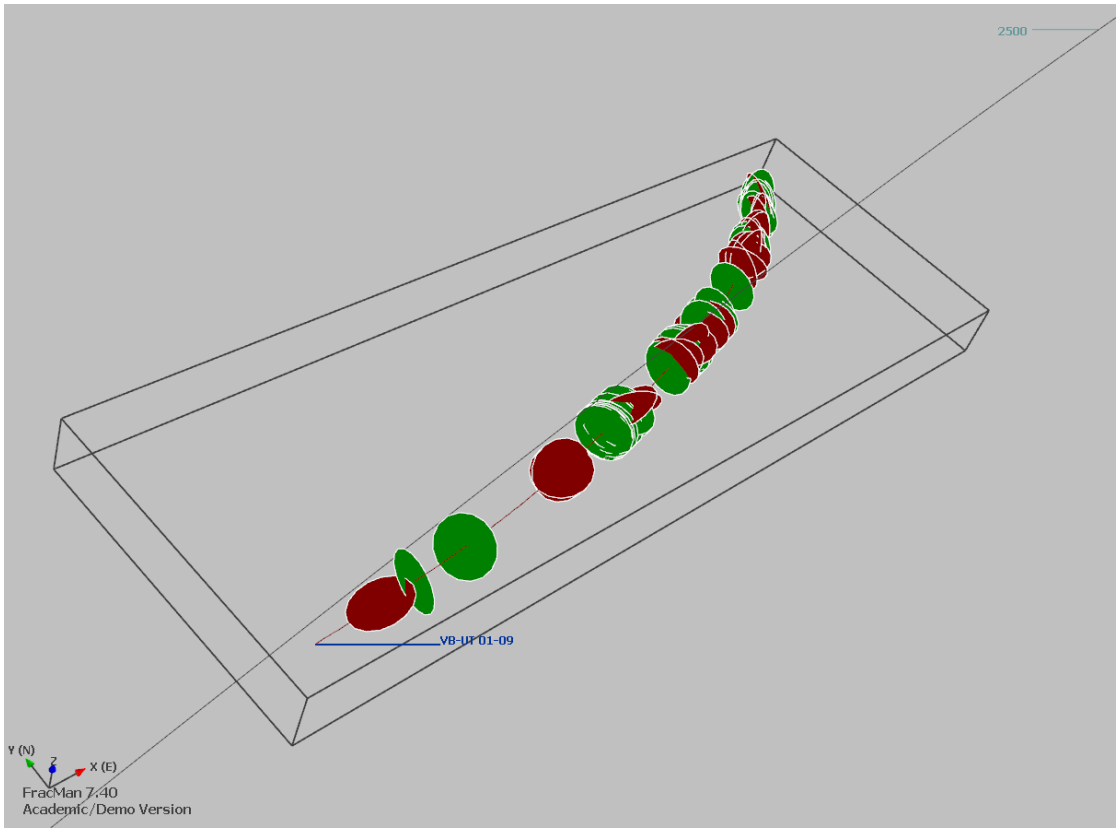

Figure 31: FracMan representation of the exploratory predrillings VB-UT 01/09 with their schistosity planes (green) and their joint planes (red)

5.2.1 Discontinuity Apertures

The next step was to establish further parameters for the 3D modelling. Consequently, we examined the fracture apertures. To this end, we analysed the discontinuities, in the predrilling records with the help of a measuring tool called Free Ruler 1.7b5 (Figure 32). Unfortunately, there were many regions along the predrillings, which were difficult to evaluate. One problem was that all optical borehole measurements needed dry or clear water filled boreholes. Therefore, the quality of the measurements was reduced in regions with a high content of solids in the flush (Brosch et al., 2001). Another problem was the change in lithology, which was concomitant with a different acoustic density. Hence, this change also appeared as a discontinuity in the predrilling records (Brosch, 2011). Additionally, classical geophysical well log measurements (e.g. caliper log, gamma-gamma density log and sonic log) would be an excellent supplement to support the imaging borehole measurements results. However, the gained results were mostly satisfying and presented in Figure 33 and Figure 34.

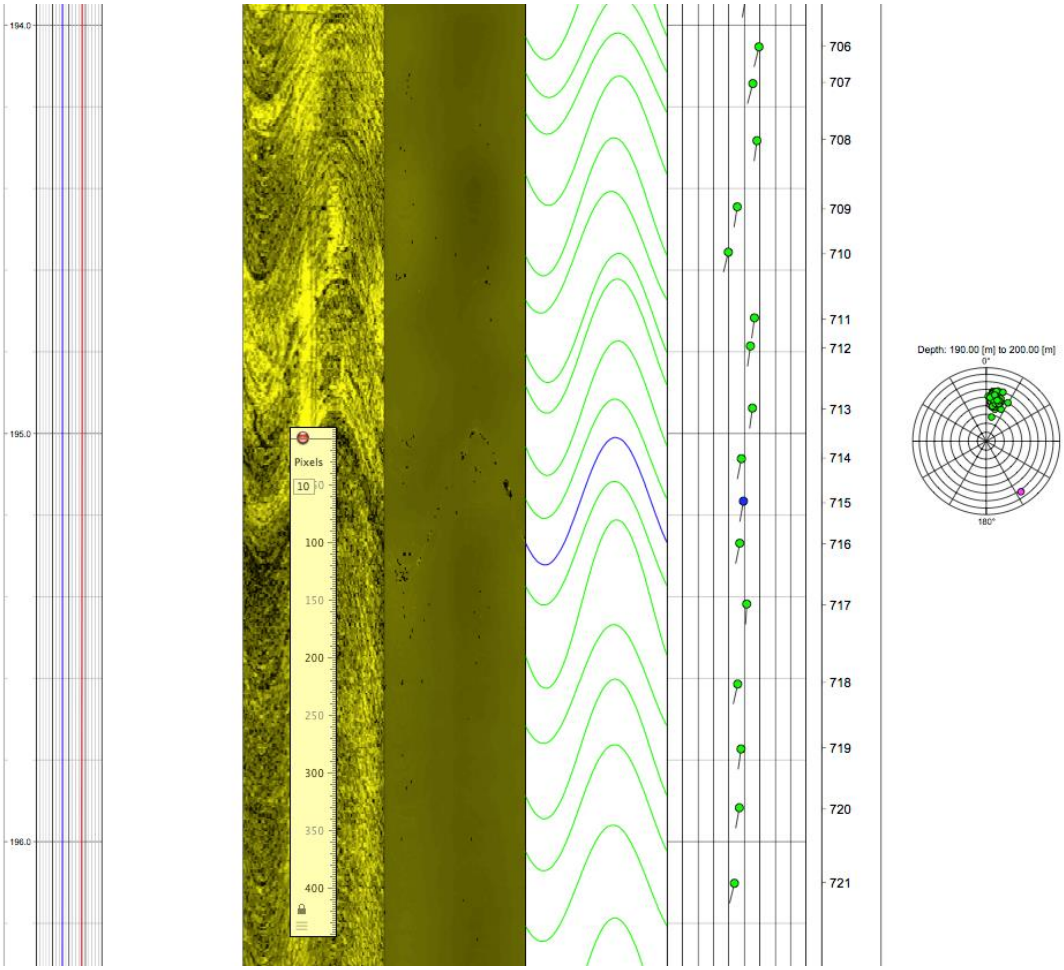

Figure 32: Acoustical borehole image of the exploratory predrilling VB-UT 02/09. Discontinuity 715 is an open joint, which displays the approximate aperture of 2 centimetres. The measurement tool shows the aperture in pixels, which is displayed in centimetres in Figure 33. (Lighter colours: dense, homogeneous polymetamorphic rock mass, Darker colours: opened single fractures and destrengthened zones (brittle) Classification: green: bedding or foliation planes, blue: joints POLAR: polar diagram (Schmidt net southern hemisphere))

Figure 33 shows the aperture distribution of predrilling VB-UT 02/09. The maximum fracture aperture in Figure 33 is approximately 3.5 centimetres wide. Accordingly, the depth, in which the maximum apertures occurred, was at approximately 170 metres. Furthermore, homogeneous aperture zones along the predrilling length were absent. Nevertheless, we compared the maximum apertures in Figure 33 and Figure 34 and saw that there is no big difference between them. In contrast, the frequency of joints is higher in predrilling VB-UT 10/09.

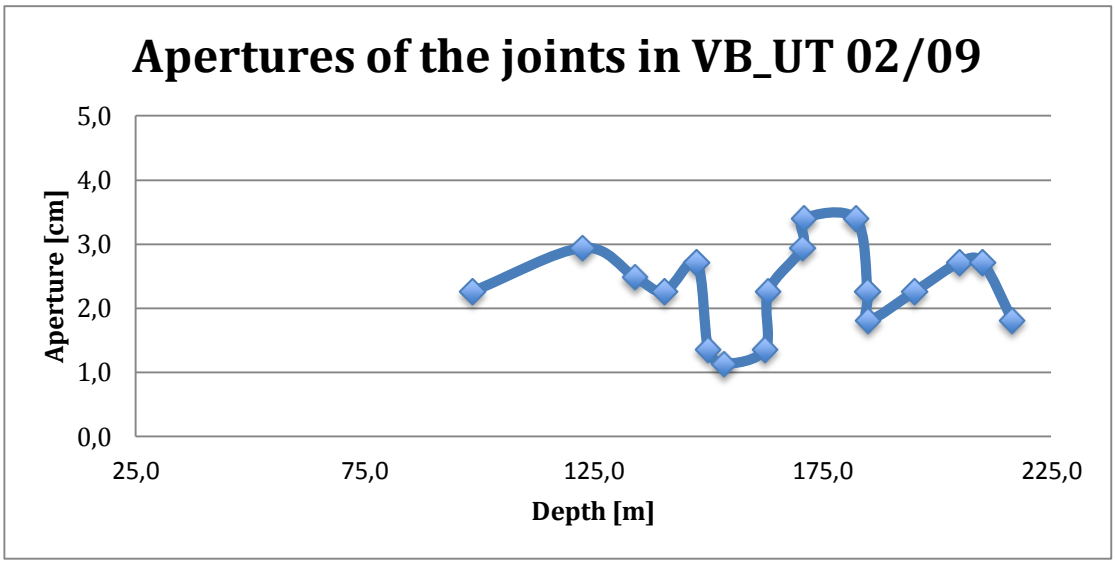

Figure 33: Fracture apertures along the exploratory predrilling VB-UT 02/09 with a maximum peak at approximately 3.5 centimetres at a depth of approximately 170 meters.

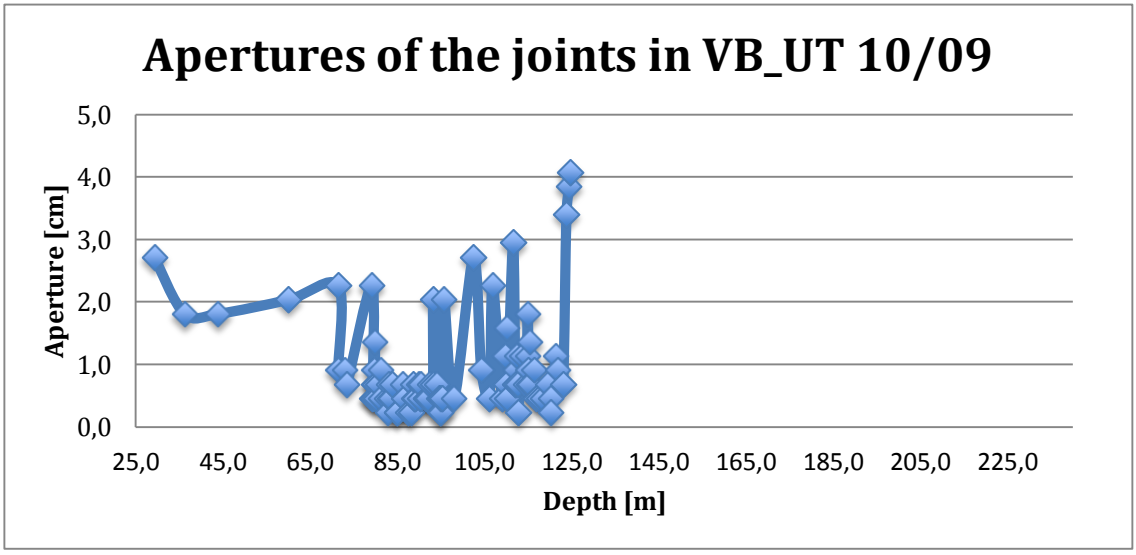

Figure 34: Fracture apertures along the exploratory predrilling VB-UT 10/09 with a maximum peak at approximately 4 centimetres at a depth of approximately 125 meters.

5.2.2 Fracture Intensity

Then, we concentrated on the determination of the fracture intensity or simply speaking the "amount" of fractures in a given rock mass. First, we detected the cumulative fracture frequency q, which we determined in Equation 3 (Liu, 2012).

$$q = \frac{i}{n+1} \qquad (3)$$

Equation 3: Determination of the cumulative fracture frequency (Liu, 2012)

q...cumulative fracture frequency
i...fracture number
n...total fracture number

We evaluated the cumulative fracture frequency q first for all fractures along the first and the last exploratory predrilling to compare them in Figure 35 and Figure 36. Then, we did the determination separately for the schistosity planes of the predrilling in Figure 37 and Figure 38. Finally, we compared the cumulative frequencies of the joint planes in Figure 39 and Figure 40. Therefore, the predrilling VB-UT 10/09 in the crystalline region shows the highest cumulative fracture frequency in all comparisons.

Additionally, we evaluated the one-dimensional fracture intensity P_{10}, which describes the number of fractures per unit length determined in Equation 4. We calculated this parameter in each predrilling separately for the schistosity planes and the joint planes (Table 2). Figure 41 shows the comparison of all P_{10} values of the schist- and joint planes along the exploratory area from the west to the east.

$$P_{10} = \frac{n}{L} \qquad (4)$$

Equation 4: Determination of the one-dimensional fracture intensity P10 (Liu, 2012)

P_{10}...one-dimensional fracture intensity
n...total fracture number
L...total predrilling length

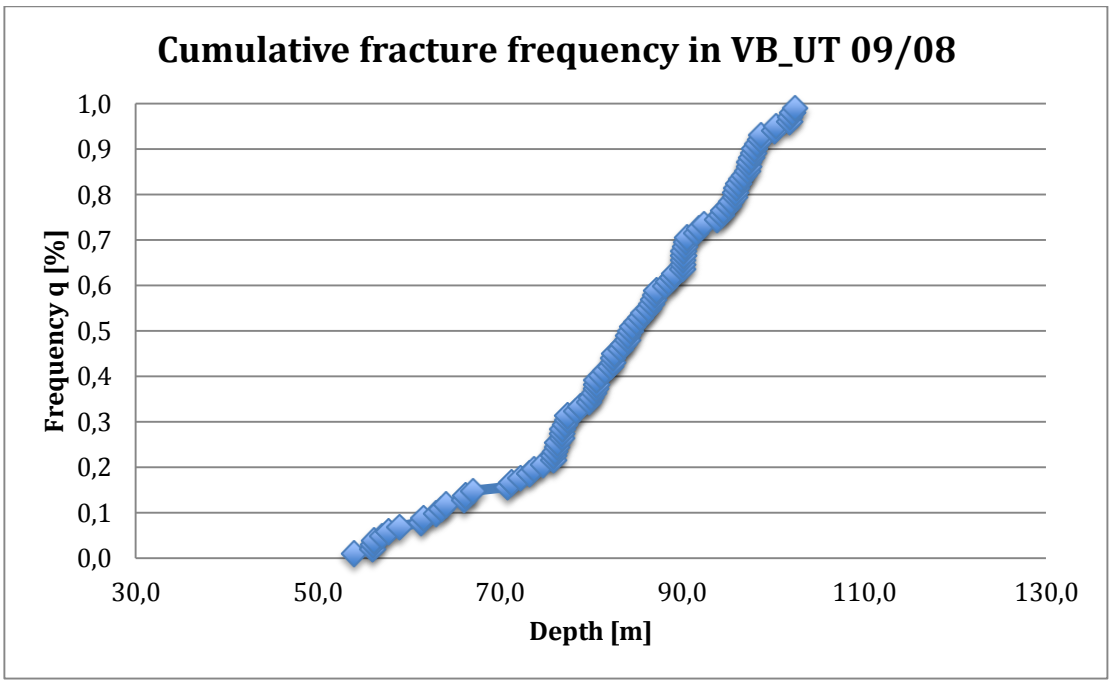

Figure 35: Cumulative fracture frequency along the predrilling VB-UT 09/08

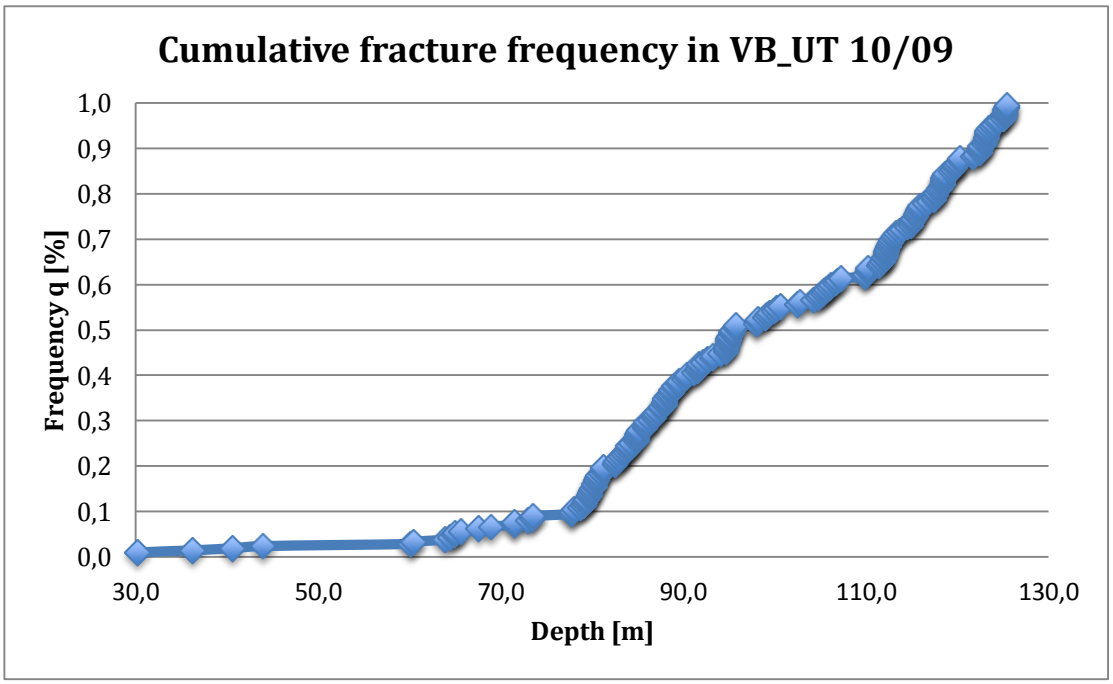

Figure 36: Cumulative frequency along the predrilling VB-UT 10/09

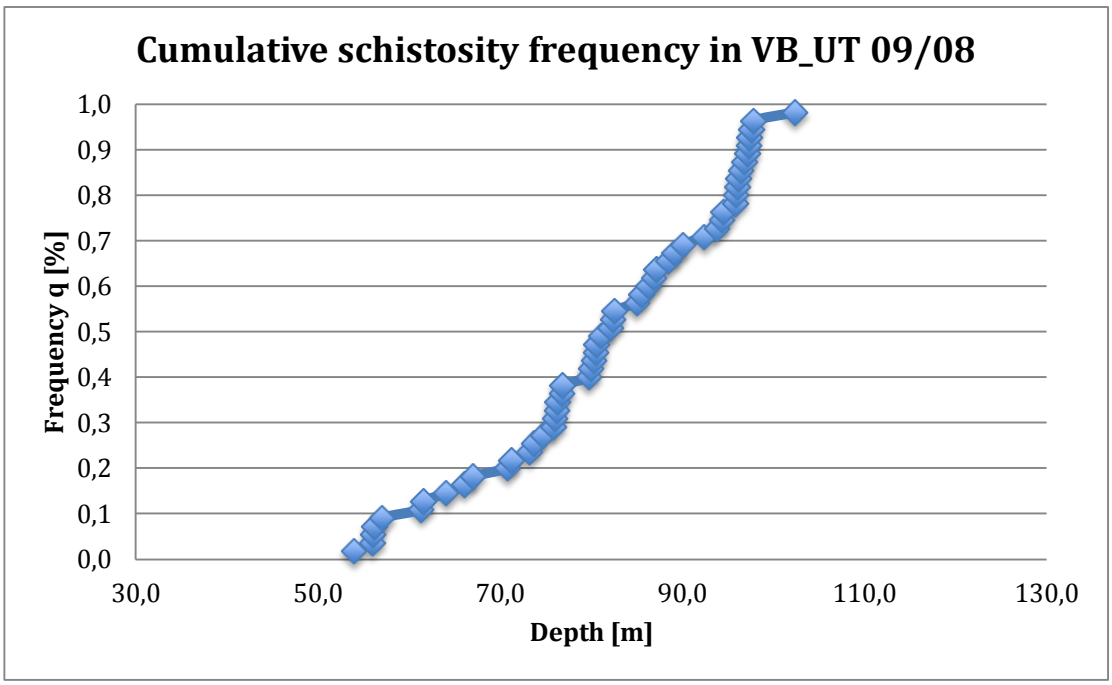

Figure 37: Cumulative schistosity frequency along the predrilling VB-UT 09/08

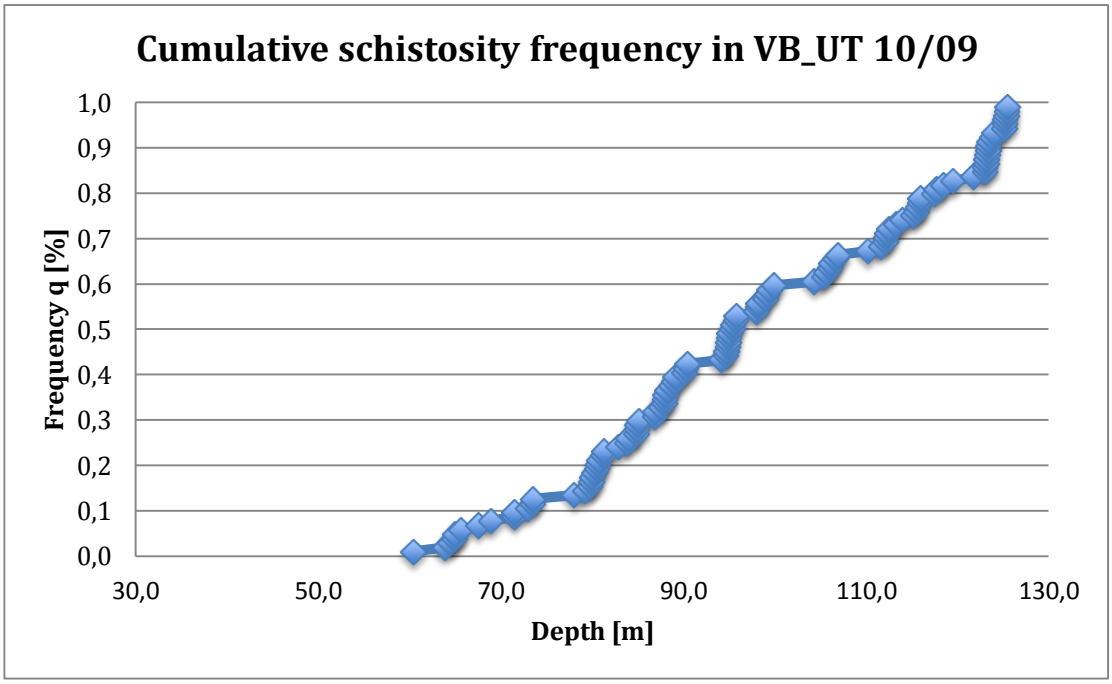

Figure 38: Cumulative schistosity frequency along the predrilling VB-UT 10/09

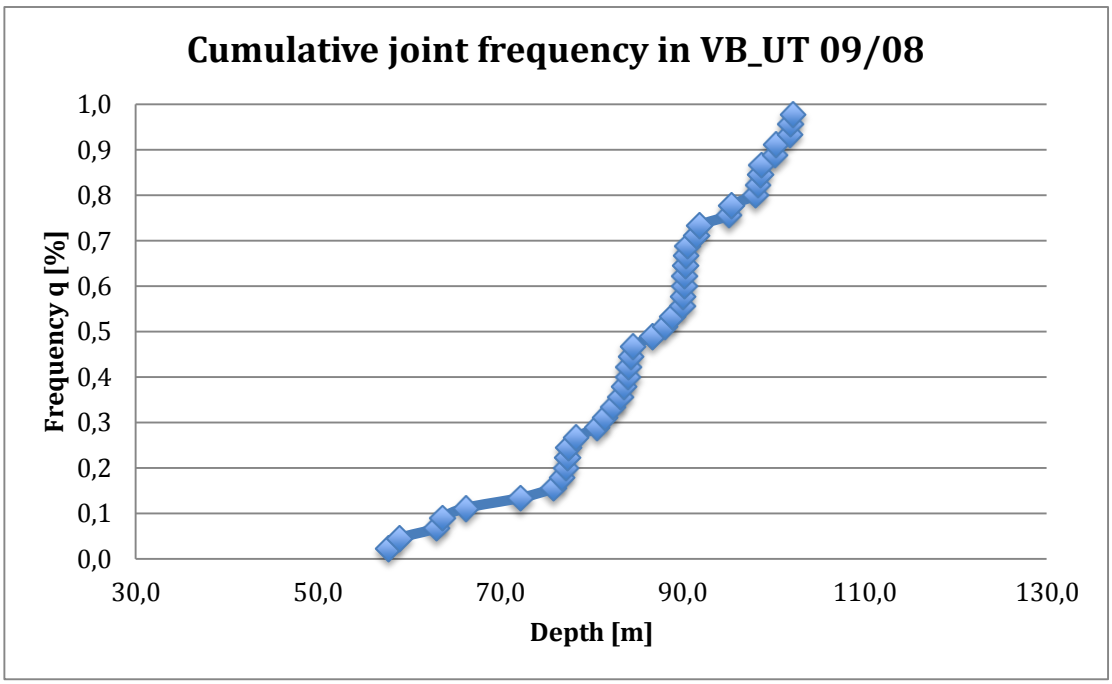

Figure 39: Cumulative joint frequency along the predrilling VB-UT 09/08

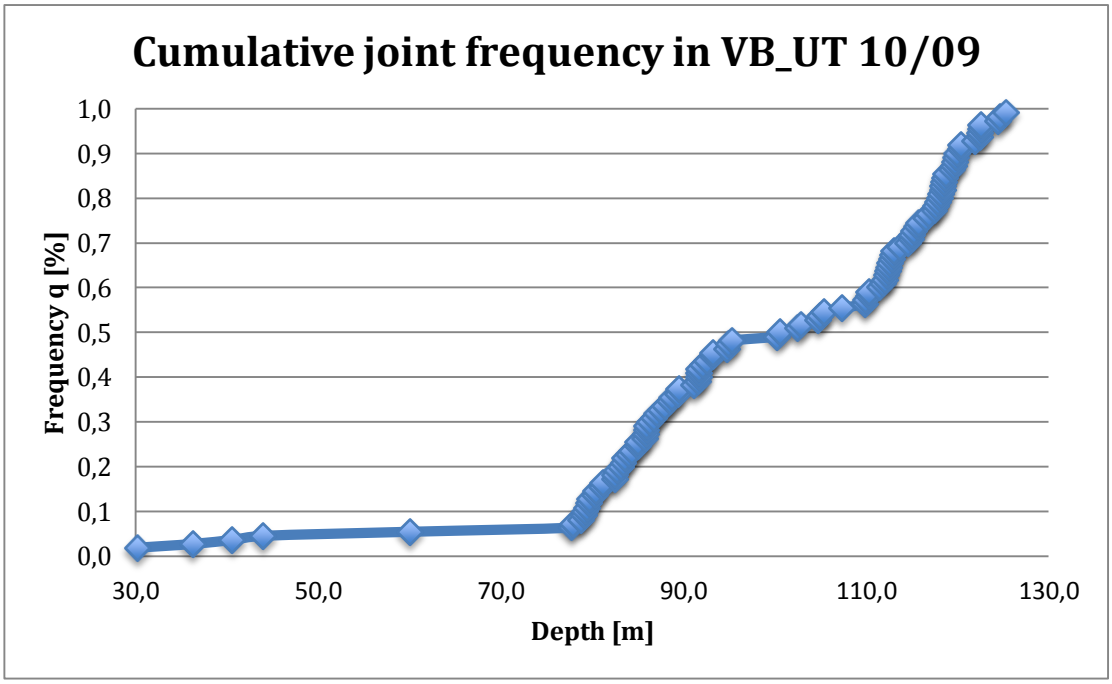

Figure 40: Cumulative joint frequency along the predrilling VB-UT 10/09

Table 2: One-dimensional fracture frequency P10 of all examined predrillings according to Figure 41 and homogeneous intensity zones (yellow: zone 1, green: zone 2, orange: zone 3 and blue: zone 4)

Number	Predrilling	P10-schistosity per m	P10-joints per m
1	VB-UT 09/08	1.093	0.887
2	VB-UT 11/08	0.210	0.395
3	VB-UT 01/09	0.141	0.040
4	VB-UT 02/09	0.265	0.043
5	VB-UT 03/09	0.344	0.077
6	VB-UT 04/09	0.714	0.394
7	VB-UT 05/09	1.555	0.358
8	VB-UT 06/09	1.161	0.454
9	VB-UT 08/09	0.661	0.158
10	VB-UT 09/09	1.824	0.146
11	VB-UT 10/09	1.061	0.371

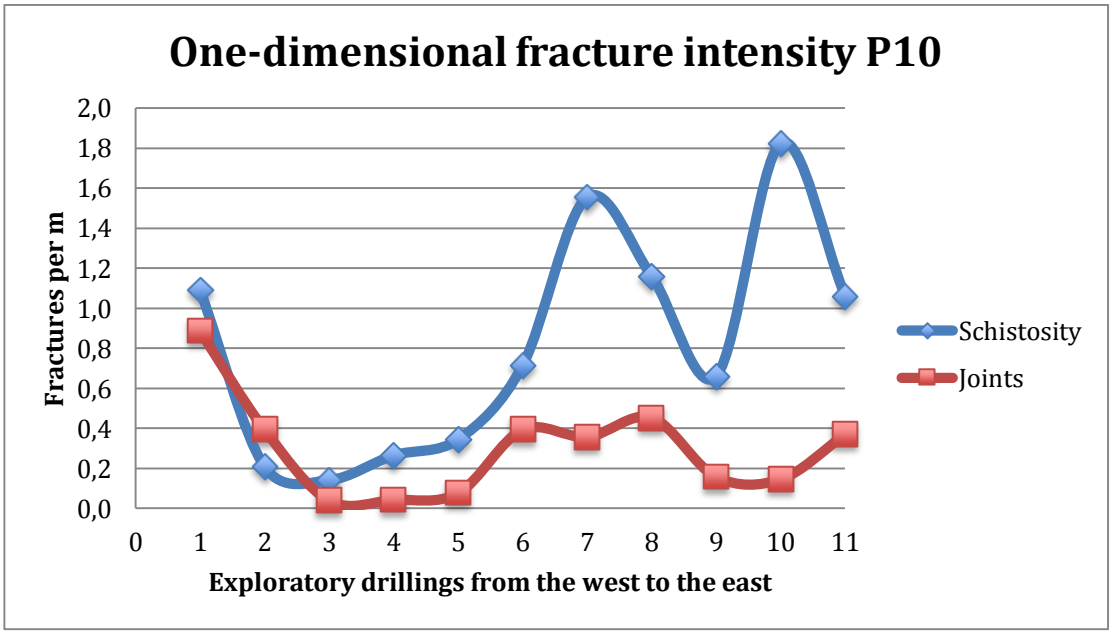

Figure 41: One-dimensional fracture intensity P10 along the exploratory region from the west to the east

To characterise homogenous fracture intensity zones along the total predrilling length, we compared all results and identified similar regions. First, we checked the one-dimensional fracture intensity patterns in Figure 41 to indicate similarities and differences. We saw a virtually equal curve progression of the schistosity and joint intensities from predrilling one to six. The predrillings seven to eleven show unequal curve progressions and remarkably higher schistosity intensities, which can be associated with a lithology change. Then we analysed Table 2, identified similar trends and subdivided the predrillings in homogeneous intensity zones. Therefore, the yellow shaded region identifies zone one, the green shaded region zone two, the orange shaded region zone three and the blue shaded region zone four.

5.2.3 Trace Length

The evaluation of the trace length was in this case very important because we needed the values for the establishment of the equivalent radius and the 3D fracture system models. The trace length could not have been detected directly out of the borehole images. Consequently we had to study the structure table of the exploratory predrillings, which we obtained from the ÖBB and furthermore the geological documentation of the 3G geotechnical group. To this end, we determined the minimum and maximum trace length and calculated the median for each discontinuity set shown in Table 3, Table 4 and Table 5. Further, we needed the equivalent radius to model the fracture systems. Therefore, we evaluated the equivalent radius in Equation 5. The gained results are shown in Table 6, Table 7 and Table 8.

$$Re = \frac{l(Median)}{2} \qquad (5)$$

Equation 5: Determination of the equivalent radius.

Re...equivalent radius
l...fracture size (Median)

Table 3: Trace length of the schistosity planes (A_R: azimuth, FA: dip angle, l: fracture size; min.: minimum, max.: maximum)

Predrilling	Set	A_R	FA	l min [m]	l max [m]	l (Median)
09/08	Set 1	112	35	0.20	2.00	1.10
11/08	Set 1	173	30	0.50	2.50	1.50
11/08	Set 2	52	29	0.10	0.50	0.30
01/09	Set 1	178	25	0.10	0.50	0.30
01/09	Set 2	50	26	0.10	0.50	0.30
02/09	Set 1	173	37	0.30	1.50	0.90
03/09	Set 1	137	27	0.30	2.50	1.40
04/09	Set 1	137	32	0.45	3.00	1.73
05/09	Set 1	139	29	0.50	3.00	1.75
06/09	Set 1	132	24	0.50	3.50	2.00
08/09	Set 2	72	31	1.00	5.00	3.00
09/09	Set 2	69	35	1.00	5.00	3.00
10/09	Set 2	93	35	0.40	4.00	2.20

Table 4: Trace length of the joint planes (A_R: azimuth, FA: dip angle, l: fracture size, min.: minimum, max.: maximum)

Predrilling	Set	A_R	FA	l min [m]	l max [m]	l (Median)
09/08	Set 1	228	47	0.30	3.50	1.90
11/08	Set 1	265	43	1.00	3.50	2.25
11/08	Set 2	42	72	0.50	2.75	1.63
11/08	Set 3	129	74	1.00	5.50	3.25
01/09	Set 1	299	21	1.50	4.00	2.75
01/09	Set 2	92	21	1.00	3.85	2.43
01/09	Set 3	184	70	1.05	3.00	2.03
02/09	Set 1	250	67	1.00	3.00	2.00
02/09	Set 2	86	74	1.00	2.50	1.75
02/09	Set 1	171	77	0.40	3.00	1.70
02/09	Set 4	326	76	1.50	2.75	2.13
03/09	Set 1	236	67	0.50	2.00	1.25
03/09	Set 2	57	67	2.00	6.00	4.00
03/09	Set 3	151	74	0.50	1.50	1.00
04/09	Set 1	268	58	0.60	2.00	1.30
04/09	Set 2	58	76	0.80	3.00	1.90
04/09	Set 3	133	60	2.50	6.00	4.25
05/09	Set 1	267	55	1.00	5.00	3.00
05/09	Set 2	56	78	0.50	3.00	1.75
05/09	Set 3	149	48	5.00	6.00	5.50
06/09	Set 1	246	58	1.90	5.00	3.45
06/09	Set 2	54	76	1.50	4.00	2.75
06/09	Set 3	147	71	5.00	6.00	5.50
08/09	Set 1	242	59	1.50	3.00	2.25
08/09	Set 2	40	62	1.00	2.00	1.50
08/09	Set 4	338	53	1.50	3.00	2.25
09/09	Set 1	249	61	1.50	2.25	1.88
09/09	Set 2	60	80	1.00	4.00	2.50
10/09	Set 1	254	48	1.50	4.00	2.75
10/09	Set 2	48	76	1.00	4.00	2.50

Table 5: Trace length of the fault planes (A_R: azimuth, FA: dip angle, l: fracture size, min.: minimum, max.: maximum)

Predrilling	Set	A_R	FA	l min [m]	l max [m]	l (Median)
09/08	Set 1	195	48	6.55		6.55
08/09	Set 2	252	78	6.00		6.00

5.3 Data Evaluation

5.3.1 Classification of Homogeneous Zones

After our intensive parameter studies we compared all results and tried to find homogeneous zones according all parameters along the exploratory region. Therefore, to model the 3D fracture systems of each zone and carry out the stability analysis. Finally, we defined four homogeneous zones. Accordingly, the results are shown in Table 6, Table 7 and Table 8. Further, we wanted to show our results on a map to gain a better overview along the exploratory region. Hence, we draw a geological map of the region per hand based on the results of previous investigations, which can be found in the Appendix.

Table 6: Homogeneous zones schistosity: (yellow: zone1, green: zone 2, orange: zone 3, blue: zone: 4), (A_R: azimuth, Φ: dip, P_{32}: volumetric fracture density, Re: equivalent radius)

Zone	Set	A_R	Φ	P_{32}	Concentration	*Re*	Length of advance [m]
Z1	set 1	112	35	2.187	14.06	0.55	1.7
Z2	set 1	173	30	1.740	21.17	0.45	3
Z2	set 2	51	27.5	0.469	38.14	0.15	3
Z3	set 1	137	28	9.375	38.64	0.87	2.2
Z4	set 1	72	35	2.122	58.00	1.50	1.7

Table 7: Homogeneous zones joints: (yellow: zone1, green: zone 2, orange: zone 3, blue: zone: 4), (A_R: azimuth, Φ: dip, P_{32}: volumetric fracture density, Re: equivalent radius)

Zone	Set	A_R	Φ	P_{32}	Concentration	*Re*	Length of advance [m]
Z1	set 1	228	47	0.887	10.670	0.95	1.7
Z2	set 1	265	43	0.074	12.430	1.13	3
Z2	set 2	86	72	0.093	24.860	0.88	3
Z2	set 4	326	76	0.028	75.110	1.06	3
Z3	set 2	56.5	76	0.525	28.965	1.16	2.2
Z3	set 3	148	65.5	0.333	20.825	2.44	2.2
Z4	set 1	249	59	0.282	10.5	1.13	1.7
Z4	set 2	48	76	0.157	34	1.25	1.7
Z4	set 4	338	53	0.304	10.47	1.13	1.7

Table 8: Homogeneous zones faults: (yellow: zone1, green: zone 2, orange: zone 3, blue: zone: 4), (A_R: azimuth, Φ: dip, P_{32}: volumetric fracture density, Re: equivalent radius)

Zone	Set	A_R	Φ	P_{32}	Concentration	*Re*	Length of advance [m]
Z1	set 1	195	48	0.021	33.54	4.50	1.7
Z2							3
Z3							2.2
Z4	set 2	252	78	0.012	54.00	3	1.7

5.3.2 FracMan – Generation of 3D Fracture System Models

After the classification of the homogenous zones, we started with the modelling of the 3D fracture system models of each zone. Therefore, to identify the unstable and stable blocks of each zone to further characterize rock mass.

First, we inserted a region box with the measures 20 m x 20 m x 20 m. Actually, we chose such a small box because of the low modelling capacity of the computers of the Institute of Applied Geosciences of the University of Technology Graz. Then, we modelled the fracture sets. Accordingly, we needed the following input parameters of the fracture planes:

- Intensity
- Orientation (Concentration)
- Size (Equivalent Radius)
- Shape (Elongation)
- Distribution of the Equivalent Radius
- Termination percentage

We already evaluated the one-dimensional fracture intensity P_{10} in equation 4. Additionally, we needed the volumetric fracture density P_{32} for the generation of our models. The P_{32} value is expressed by the sum of the fracture size of one set divided by the volume. However, it is extremely difficult to measure, thus we evaluated it based on P_{10}. That was possible because P_{10} is a linear function of P_{32} as you can see in Equation 6.

$$P_{32} = P_{10}(P_{32}^{*}/P_{10}^{*}) \qquad (6)$$

Equation 6: Function of the volumetric fracture density P_{32} (Dershowitz & Herda, 1992).

P_{32}...volumetric fracture density
P_{32}...assumed volumetric fracture density*
P_{10}...one-dimensional fracture intensity
P_{10}... simulated linear intensity in a certain direction*

Subsequently, we had to compute the P_{10}* values for each fracture set. First, we generated each fracture set with an assumed volumetric fracture intensity P_{32}* shown in Table 9. For example, we generated the schistosity planes of one zone with a P_{32}* value of 0.5 in the region box (Figure 42) and inserted a borehole. Latter intersected with the simulated fracture set (Figure 43) and P_{10}* could be determined in Equation 7. Whereas n is the number of intersections and L the borehole length, in this case 20 meters because of the assumed region box parameters. In the end, we evaluated the volumetric fracture intensities in Equation 6, which we needed later on for the generation of the final fracture sets shown in Figure 44.

$$P_{10}^{*} = \frac{n}{L} \qquad (7)$$

Equation 7: Simulated linear intensity in a certain direction.

P_{10}... simulated linear intensity in a certain direction*
n...number of intersections
L...borehole length

Table 9: Assumed P_{32}* values of the different fracture types (P_{32}*: assumed volumetric fracture density)

Type	P_{32}*
Schistosity	0.5
Joints	0.1
Faults	0.005

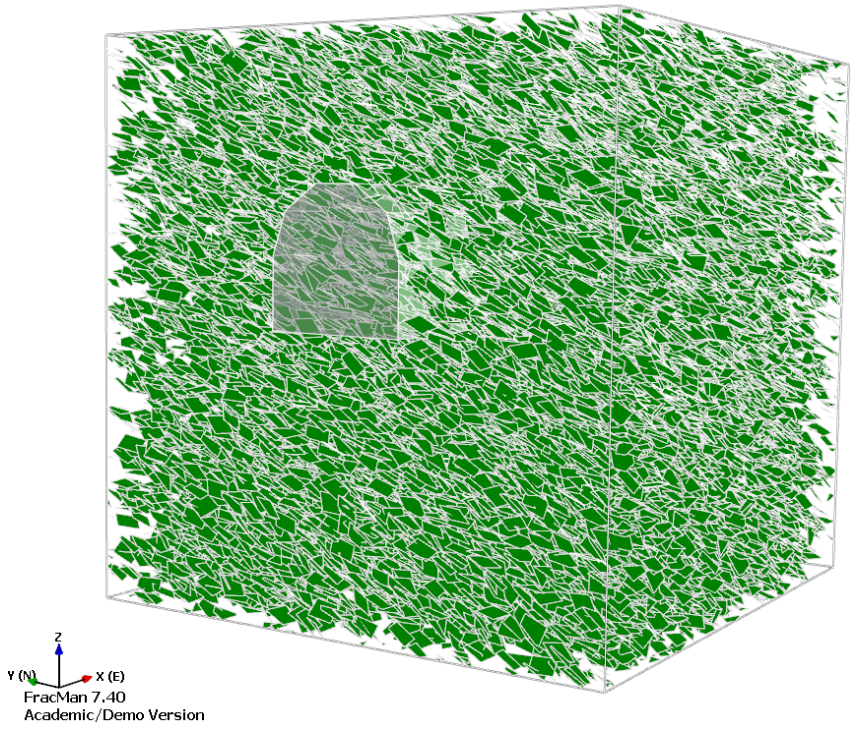

Figure 42: Schistosity set with assumed volumetric fracture intensity and a scaled virtual tunnel in the region box

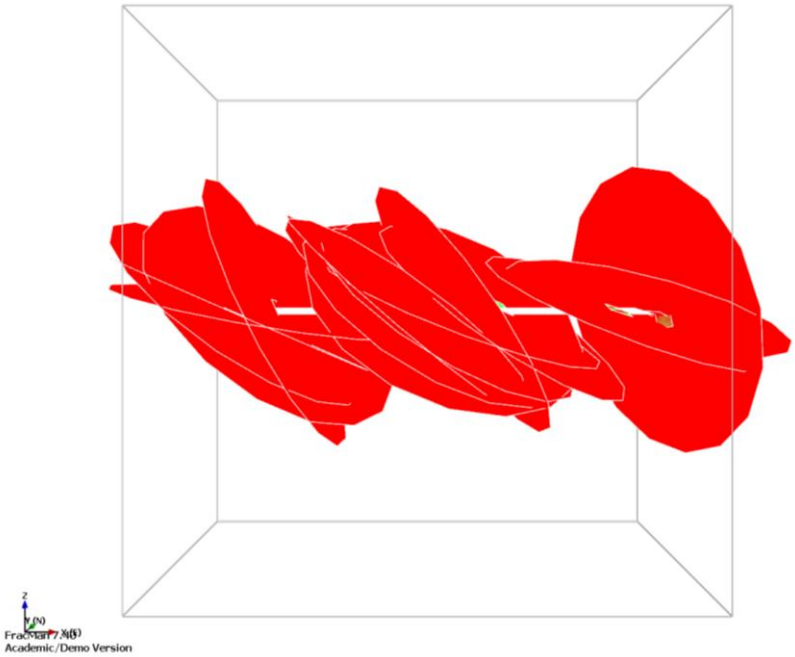

Figure 43: Fracture plane intersections on the simulated well in the region box

Accordingly, we needed to define all further parameters. Thus, we took the Enhanced Baecher model as generation model, where the location and arrangement in space is described. Therefore, the fracture centres are located uniformly in space using a Poisson process (Liu, 2012). In addition, we defined the geometry of the model and inputted the pole trend and plunge of the fracture set and the distribution type. In this case, we used the Fisher distribution, which is defined by the concentration parameter k. We evaluated the orientation and the concentration with the software Sphaira. Further, we had to define the fracture size, which is described by the equivalent radius (Table 6, Table 7 and Table 8). Hence, we also entered the distribution type. We used a constant distribution for the schistosity planes and an exponential distribution for the joint and fault planes.

Additionally, we defined the fracture shape, which is quantified by the aspect ratio. The aspect ratio is defined as the ratio between the major axis and the minor axis (Liu, 2012). We inputted the number of four sides. Another important parameter was the elongation of the fractures. To this end, we had to define the aspect ratio (short/long), we also chose a constant distribution for the schistosity planes and an exponential distribution for the others. Then, we defined the elongation axis with pole trend and plunge and took a constant distribution for all fracture types.

In the end, we defined a constant distribution for the aperture, transmissivity and storativity properties. Consequently, we entered a termination percentage of cero for the schistosity planes. Which means that no schistosity plane ends in one another. In contrast to that a percentage of hundred for the joint and fault planes, that means that all joints and faults end in each other. Finally, we generated our discrete fracture network (DFN) and a scaled virtual tunnel in Figure 44 to further analyse the rock mass stability behaviour.

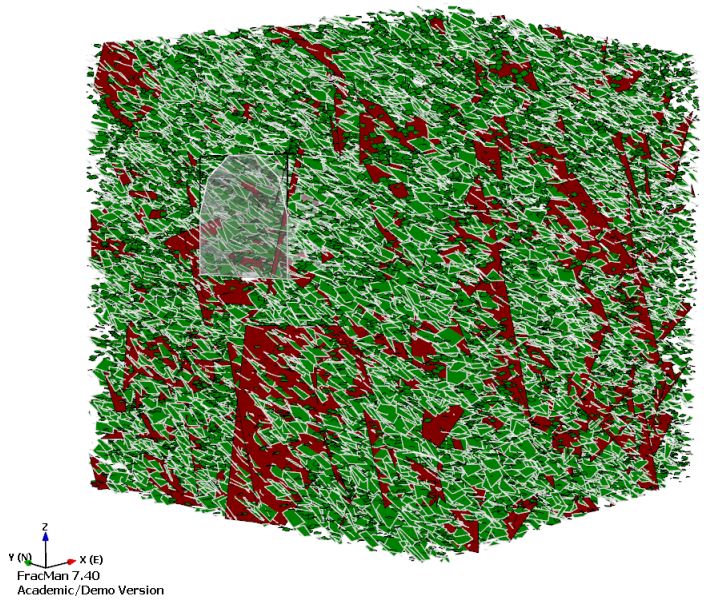

Figure 44: Final fracture sets and the scaled virtual tunnel

We accessed the analysis by selecting static analysis and chose geomechanics and further rock wedge. Then, we defined the rock wedge analysis parameters in the file menu. First, we specified the project settings. Thus, we selected a horseshoe sampling structure and six as a maximum level of connection from sampling object. We chose tunnel as the structure type. However, we took the standard input parameters for the loading conditions and the fracture properties. Therefore, we chose no support patterns. As output parameters, we selected post processing for composite blocks, display statistics, a factor of safety histogram, a weight and a volume histogram. Then, we were running the analysis and generated the rock blocks, which are shown in Figure 45. Additionally, Figure 46 shows the output statistics in numbers.

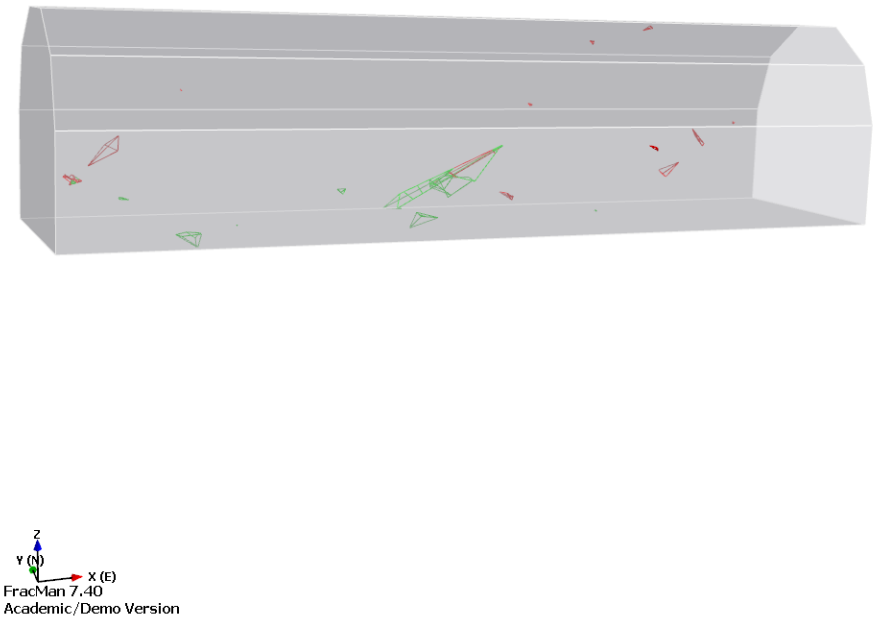

Figure 45: Tunnel simulation with stable (green) and unstable blocks (red)

Project Name:	RockBlock 1
Total Blocks	48
Stable Blocks	20
Unstable Blocks	28
Free Fall Blocks	0
Maximum block weight [t]	0.31828777
Average block weight [t]	0.015896764
Maximum block volume [m^3]	0.11788436
Average block volume [m^3]	0.0058876905
Maximum block height [m]	0.5763136
Average block height [m]	0.17069761
Maximum block width [m]	2.0051289
Average block width [m]	0.3942525
Maximum block surface area [m^2]	1.9022396
Average block surface area [m^2]	0.17375471
Maximum unstable block weight [t]	0.033780761
Average unstable block weight [t]	0.0036480357
Maximum freefall block weight [t]	0
Average freefall block weight [t]	0

Project Name:	RockBlock 1:Composite
Total Blocks	26
Stable Blocks	10
Unstable Blocks	16
Free Fall Blocks	0
Maximum block weight [t]	0.59348904
Average block weight [t]	0.029317926
Maximum block volume [m^3]	0.21981076
Average block volume [m^3]	0.010858491
Maximum block height [m]	0.5763136
Average block height [m]	0.16749053
Maximum block width [m]	5.5099315
Average block width [m]	0.54777702
Maximum block surface area [m^2]	4.3303093
Average block surface area [m^2]	0.27900692
Maximum unstable block weight [t]	0.028412325
Average unstable block weight [t]	0.0029712806
Maximum freefall block weight [t]	0
Average freefall block weight [t]	0

Figure 46: Rock blocks statistics

To receive significant statistical distributions we repeated the above-described process thirty times in each zone. The values not only rely on single blocks they further rely on block associations. Subsequently this is a purpose for the high maximum volumes we sometimes received which were partly caused by stable blocks. In contrast to stable blocks, unstable blocks have a failure mode that is called sliding. They can slide on two planes or just on a single plane. Additionally, free fall blocks are also unstable blocks, which do not slide on a plane, they free fall.

We utilized the block amount of all blocks and visualized them in diagrams. Figure 47 shows the mean block number of all zones. Therefore, we plotted the total, the stable, the unstable and the free fall blocks against each other. It is obvious that we have the maximum block number in zone three and the minimum block number in zone two. Figure 48 shows the same trends, only with a smaller number of total, stable, unstable and free fall blocks.

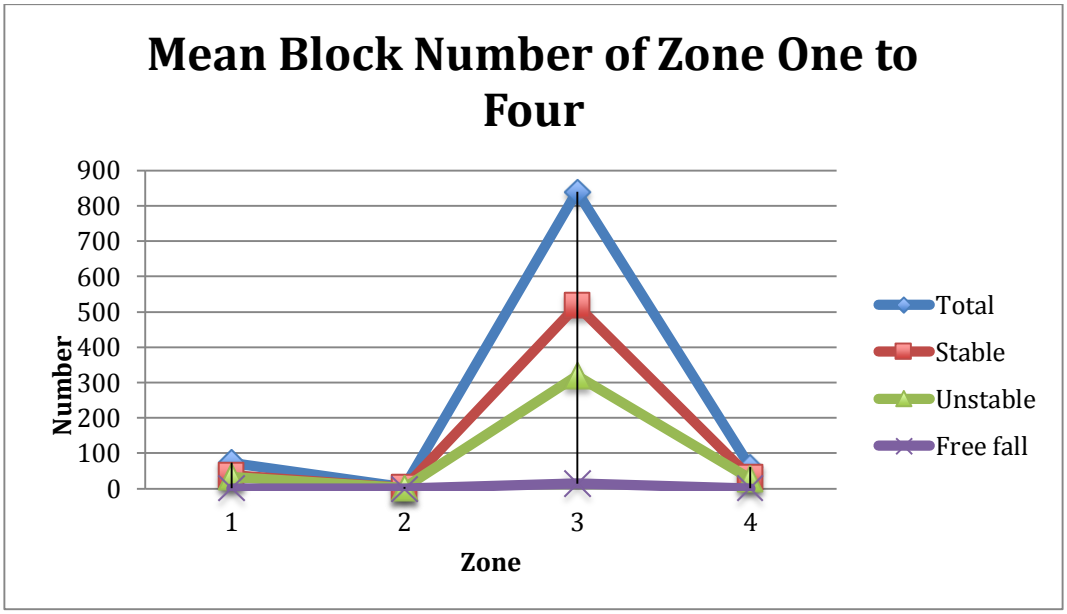

Figure 47: A comparison of the block amount of all zones

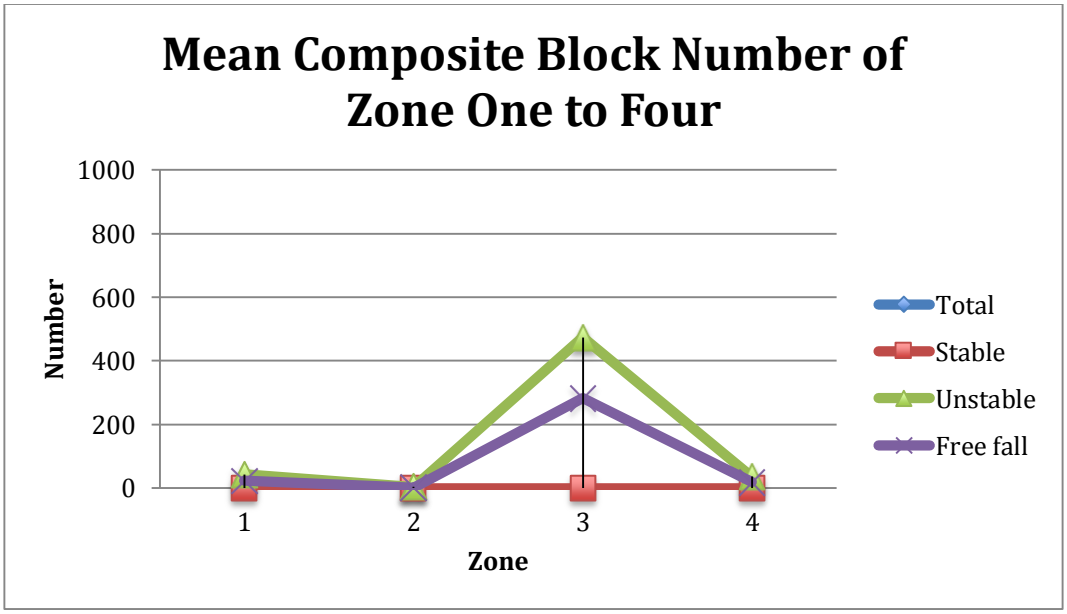

Figure 48: A comparison of the composite block amount of all zones

5.4 Data Analysis

5.4.1 Statistic Computer Software R

Moreover, we needed to analyse the received distribution of the volume and apex of the stable and unstable blocks in detail. To this end, we used the statistic computer software R. The input file is shown in Figure 49 and Figure 50 in addition the output file is displayed in Figure 51 and Figure 52.

```
# Katrin Masterprojekt: stab_z1.R
# Copyright Q.Liu & K.Hollersbacher, Jun.2014

library(e1071)

cat("Deskriptive Statistik von instablen Volumen, Zone1","\n")
# read in data
Temp <- read.table("stab_z1.txt", row.names=NULL, header=T)
v <- Temp$vol
a <- Temp$apex

cat("\nBlockvolumen:","\n")
print(v)

cat("\nStatistische Masszahlen:","\n")
cat("\nZusammenfassende mit der 'summary()'","\n")
print(summary(v))
cat("\nMittelungsmasse mit 'mean()' u. 'median()'")
cat("\n","Mittelwert =",mean(v))
cat("\n","Median =",median(v))

cat("\n\nLokalisationsmasse - Quantile mit den kumulativen
 Wahrscheinlichkeiten:","\n")
p <- c(0, 0.25, 0.5, 0.75, 1.0)
cat("Quantile von p = (0, 0.25, 0.5, 0.75, 1.0) mit
 'quantil()'","\n")
print(quantile(v, p))

cat("\nStreuungsmasse mit 'sd()', 'var()' u. 'IQR()':")
cat("\n","Standardabweischung =",sd(v))
cat("\n","Varianz =",var(v))
cat("\n","IQR =",IQR(v), "\n")

cat("\nEmpirische Verteilungsform: die Schiefe u. der Exzess:")
cat("\n", "Schiefe =", skewness(v))
cat("\n", "Exzess =", kurtosis(v), "\n")

cat("\nHaeufigkeitsverteilungen durch Funktionen 'hist()', 'plot()',
 'lines()', 'density()', 'rug()', 'ecdf()':","\n")
# stem-and-leaf plot
cat("\nStamm und Blatt Diagramm durch die Funktion 'stem()'","\n")
stem(v)

op<-par(mfrow = c(1,2), pty = "m")
cat("\nDie graphische Form von beschreibenden Statistiken
```

Figure 49: R input file of the stable blocks of zone one part one

```
 'boxplot()'","\n")
boxplot(v,ylab="Block Volume [m^3]", xlab="Total")
boxplot(v, ylim=c(0,0.065), ylab="Block Volume [m^3]", xlab="Main
 Area")
par(op)

readline("Tastedruecken")

cat("\nBloeckeHoehe:","\n")
print(a)

cat("\nStatistische Masszahlen:","\n")
cat("\nZusammenfassende mit der 'summary()'","\n")
print(summary(a))
cat("\nMittelungsmasse mit 'mean()' u. 'median()'")
cat("\n","Mittelwert =",mean(a))
cat("\n","Median =",median(a))

cat("\n\nLokalisationsmasse - Quantile mit den kumulativen
 Wahrscheinlichkeiten:","\n")
p <- c(0, 0.25, 0.5, 0.75, 1.0)
cat("Quantile von p = (0, 0.25, 0.5, 0.75, 1.0) mit
 'quantil()'","\n")
print(quantile(a, p))

cat("\nStreuungsmasse mit 'sd()', 'var()' u. 'IQR()':")
cat("\n","Standardabweischung =",sd(a))
cat("\n","Varianz =",var(a))
cat("\n","IQR =",IQR(a), "\n")

cat("\nEmpirische Verteilungsform: die Schiefe u. der Exzess:")
cat("\n", "Schiefe =", skewness(a))
cat("\n", "Exzess =", kurtosis(a), "\n")

cat("\nHaeufigkeitsverteilungen durch Funktionen 'hist()', 'plot()',
 'lines()', 'density()', 'rug()', 'ecdf()':","\n")
# stem-and-leaf plot
cat("\nStamm und Blatt Diagramm durch die Funktion 'stem()'","\n")
stem(a)

op<-par(mfrow = c(1,2), pty = "m")
cat("\nDie graphische Form von beschreibenden Statistiken
 'boxplot()'","\n")
boxplot(a,ylab="Block Height [m]", xlab="Total")
boxplot(a, ylim=c(0,1.35), ylab="Block Height [m]", xlab="Main
```

Figure 50: R input file of the stable blocks of zone one part two

```
R version 3.1.0 (2014-04-10) -- "Spring Dance"
Copyright (C) 2014 The R Foundation for Statistical Computing
Platform: x86_64-apple-darwin13.1.0 (64-bit)

R ist freie Software und kommt OHNE JEGLICHE GARANTIE.
Sie sind eingeladen, es unter bestimmten Bedingungen weiter zu verbreiten.
Tippen Sie 'license()' or 'licence()' für Details dazu.

R ist ein Gemeinschaftsprojekt mit vielen Beitragenden.
Tippen Sie 'contributors()' für mehr Information und 'citation()',
um zu erfahren, wie R oder R packages in Publikationen zitiert werden können.

Tippen Sie 'demo()' für einige Demos, 'help()' für on-line Hilfe, oder
'help.start()' für eine HTML Browserschnittstelle zur Hilfe.
Tippen Sie 'q()', um R zu verlassen.

[R.app GUI 1.63 (6734) x86_64-apple-darwin13.1.0]

[History restored from /Users/katrinhollersbacher/.Rapp.history]

> source("stab_z1.R")
Deskriptive Statistik von instablen Volumen, Zone1

Blockvolumen:
  [1] 7.000000 0.000126 0.000822 0.000869 0.000704 0.001891 0.000264 0.774000 0.146000 6.190000 1.560000 1.780000 0.010523 2.910000 0.002018 0.000186 0.000087 0.000026
 [19] 0.000335 0.005482 0.000433 0.003001 0.018833 0.002904 9.967810 0.000416 0.000128 0.001259 0.002154 0.000546 0.550696 0.000548 8.111840 0.000916 0.025137 0.016430
 [37] 0.000941 0.014934 0.040495 0.001421 0.006773 0.002318 0.000962 2.175590 0.000185 0.047835 0.000844 0.001769 3.510260 0.000296 0.046982 6.104050 0.280295 0.004055
 [55] 0.001479 3.549740 0.286630 0.000145 0.002615 0.000683 0.000328 0.005595 0.008399 0.059456 0.074650 2.221190 0.007087 3.093690 0.003850 6.159310 0.000124 0.000195
 [73] 0.000587 2.003730 0.000911 5.202110 1.877640 0.000787 5.658930 0.000911 5.202110 1.877640 0.000787 5.658930 0.000246 0.093482 0.003831 0.167198 0.030906 0.004900
 [91] 0.000267 0.000867 0.001023 0.000461 0.005671 1.637580 7.639290 0.000335 0.008724 0.029884 0.052625 0.000853 8.816280 0.006037 3.036880 0.008118 0.001940 0.007540
[109] 0.061687 0.000754 7.116270 0.000204 1.187060 0.000155 0.000126 3.993160 0.000000 3.877680 0.000327 0.000898 0.087497 0.734034 0.000953 8.201240 2.471620 0.000399
[127] 0.025308 0.000190 0.024105 0.000179 0.006449 0.000516 0.072477 0.001011 8.709460 0.297518 0.001909 0.004481 0.000291 0.001881 6.225070 0.509528 0.000400 6.449460
[145] 0.002311 0.041106 0.122520 8.549880 0.000689 0.013004 0.041476 2.178370 0.047370 0.236688 0.000621 6.723460 0.010990 0.000451 0.241360 0.107686 0.782702 0.002833
[163] 0.000947 0.717091 0.985561 1.582560 0.008013 0.000501 0.294968 0.002442 1.625740 0.012470 0.000205 0.001408 0.000702 0.002248 0.001824 7.080250 0.128433 0.000653
[181] 0.000414 0.001412 0.032086 0.712199 0.002351 0.002712 0.000359 0.066633 0.004792 0.002390 0.011581 0.001188 0.000346 0.000063 0.007085 0.001154 0.002820 0.000004
[199] 0.000048 0.000013 0.016917 0.000092 0.001099 0.000257 0.000129 0.003292 0.000283 0.000394 0.000078 0.000313 0.000073 0.000003 0.000054 0.020513 0.001570 0.000010
[217] 0.001390 0.000209 0.000074 0.000041 0.017102 0.000344 0.006599 0.035712 0.007129 0.027878 0.000440 0.013939 0.007587 0.000002 0.000032 0.000054 0.000044 0.001388
[235] 0.000001 0.002995 0.000128 0.001115 0.002198 0.000008 0.000001 0.005601 0.000011 0.000705 0.000990 0.000192 0.000012 0.002493 0.004108 0.000002 0.028560 0.000326
[253] 0.000577 0.000527 0.001802 0.000159 0.001175 0.000830 0.000865 0.003888 0.025176 0.006841 0.001009 0.000980 0.001185 0.016142 0.019109 0.000666 0.065508 0.000829
[271] 0.012786 0.000030 0.000685 0.002789 0.013531 0.005057 0.006030 0.012742 0.009716 0.005937 0.252813 0.000265 0.043477 0.007697 0.000909 0.000433 0.000016 0.000000
[289] 0.031244 0.000013 0.001868 0.005341 0.000245 0.000064 0.000372 0.000012 0.001144 0.000289 0.000059 0.000103 0.000048 0.000039 0.000359 0.000161 0.000254 0.000464
[307] 0.005491 0.001709 0.000546 0.000505 0.000008 0.036664 0.000004 0.001942 0.001637 0.060835 0.000084 0.000002 0.000021 0.001720 0.005018 0.005661 0.041287 0.053776
[325] 0.004672 0.002898 0.000313 0.000110 0.000547 0.006363 0.003176 0.019531 0.206065 0.709403 0.007148 0.002284 0.000025 0.054208 0.001721 0.000152 0.036527 0.000157
[343] 0.000029 0.000910 0.000015 0.000005 0.020910 0.000007 0.002886 0.002640 0.000005 0.043537 0.000513 0.000165 0.009271 0.000026 0.000002 0.000021 0.005903 0.000151
[361] 0.000033 0.000324 0.000019 0.000429 0.000052 0.001133 0.000037 0.005286 0.000012 0.002894 0.002821 0.000052 0.000015 0.000061 0.000775 0.004523 0.003358 0.000684
[379] 0.000001 0.000577 0.000120 0.000034 0.000009 0.000013 0.014197 0.066837 0.000001 0.000049 0.000017 0.000003 0.002364 0.000605 0.000598 0.009381 0.007401 0.001312
[397] 0.033027 0.000471 0.002770 0.007795 0.085381 0.005660 0.008739 0.000265 0.017430 0.010623 0.007648 0.000057 0.038604 0.000234 0.034720 0.010372 0.004617 0.000106
[415] 0.000685 0.000275 0.012537 0.001135 0.000130 0.000019 0.023561 0.038224 0.001511 0.000102 0.000464 0.000259 0.000328 0.000693 0.000385 0.000191 0.000736 0.000924
[433] 0.011023 0.000487 0.011714 0.003150 0.002887 0.000123 0.000473 0.000406 0.000134 0.000008 0.007939 0.000007 0.026443 0.000999 0.052608 0.006834 0.001090 0.000022
[451] 0.000491 0.000196 0.000025 0.010485 0.006499 0.000002 0.000176 0.000502 0.007960 0.107320 0.000197 0.001878 0.000028 0.000304 0.000811 0.007311 0.152872 0.000295
[469] 0.006479 0.017541 0.000547 0.018847 0.003724 0.002959 0.053984 0.000006 0.001124 0.007100 0.000007 0.000147 0.000734 0.000001 0.000017 0.000041 0.000343 0.011289
[487] 0.000098 0.000054 0.004161 0.001458 0.000081 0.001314 0.000192 0.000105 0.002027 0.000210 0.000212 0.000036 0.000045 0.000027 0.001187 0.000084 0.000006 0.001509
[505] 0.014108 0.000577 0.000175 0.000426 0.000062 0.000053 0.000005 0.000233 0.000862 0.040063 0.000166 0.021076 0.009840 0.000700 0.049388 0.006273 0.001076 0.001407
[523] 0.024901 0.001443 0.017074 0.002746 0.000008 0.000045 0.000002 0.000129 0.000054 0.001226 0.008700 0.000018 0.000055 0.005636 0.003531 0.002903 0.000003 0.127193
[541] 0.000012 0.001058 0.000284 0.000087 0.000046 0.000234 0.001366 0.001621 0.000004 0.000003 0.000281 0.000027 0.000007 0.011702 0.000044 0.000007 0.007163 0.004801
[559] 0.005779 0.003537 0.002386 0.006934 0.001094 0.052512 0.033111 0.024456 0.005585 0.001378 0.000052 0.000422 0.000571 0.002440 0.000036 0.001264 0.000077 0.000005
[577] 0.000032 0.002009 0.010551 0.000388 0.000099 0.000042 0.272017 1.071200 0.000027 0.000900 0.002978 0.011115 0.000017 0.002024 0.000198 0.000714 0.000084 0.001068
[595] 0.000850 0.001183 0.000128 0.000033 0.000003 0.003532 0.000013 0.000281 0.000011 0.000196 0.000083 0.001018 0.001007 0.000316 0.000030 0.000395 0.001360 0.000001
[613] 0.001308 0.000024 0.000059 0.000015

Statistische Masszahlen:

Zusammenfassende mit der 'summary()'
    Min.  1st Qu.   Median     Mean  3rd Qu.     Max.
0.000000 0.000184 0.001128 0.330200 0.009747 9.968000

Mittelungsmasse mit 'mean()' u. 'median()'
 Mittelwert = 0.3301639
 Median = 0.0011285

Lokalisationsmasse - Quantile mit den kumulativen Wahrscheinlichkeiten:
Quantile von p = (0, 0.25, 0.5, 0.75, 1.0) mit 'quantil()'
       0%       25%       50%       75%      100%
0.0000000 0.0001835 0.0011285 0.0097470 9.9678100

Streuungsmasse mit 'sd()', 'var()' u. 'IQR()':
 Standardabweischung = 1.333601
 Varianz = 1.77849
 IQR = 0.0095635

Empirische Verteilungsform: die Schiefe u. der Exzess:
 Schiefe = 4.784336
 Exzess = 23.23203

Haeufigkeitsverteilungen durch Funktionen 'hist()', 'plot()', 'lines()', 'density()', 'rug()', 'ecdf()':

Stamm und Blatt Diagramm durch die Funktion 'stem()'

  The decimal point is at the |

  0 | 000000000000000000000000000000000000000000000000000000000000000000000000000000000000000000+486
  0 | 56777788
  1 | 012
  1 | 6666899
  2 | 0222
  2 | 59
  3 | 01
  3 | 559
  4 | 0
  4 |
  5 | 22
  5 | 77
  6 | 12224
  6 | 7
  7 | 011
  7 | 6
  8 | 12
  8 | 578
  9 |
  9 |
  10 | 0
```

Figure 51: R output file of the stable blocks of zone one part one

```
Die graphische Form von beschreibenden Statistiken 'boxplot()'
Tastedruecken

BloeckeHoehe:
  [1] 0.049767 0.115828 0.278901 0.323007 0.123204 0.234153 0.084600 0.025138 0.015318 0.123204 0.065623 0.118257 0.264763 0.077621 0.158862 0.084076 0.052707 0.036833
 [19] 0.074131 0.293909 0.121555 0.312459 0.477674 0.326819 0.111082 0.124204 0.263942 0.143016 0.368703 0.205900 0.016001 0.171716 0.114575 0.387397 0.087518 0.389839
 [37] 0.146457 0.287184 0.430994 0.189292 0.593989 0.325531 0.346203 0.053892 0.121271 0.721048 0.171610 0.258101 0.059613 0.091342 0.496479 0.133042 0.028233 0.491685
 [55] 0.173905 0.074685 0.086426 0.094062 0.283449 0.286594 0.149330 0.251046 0.403951 0.654564 0.108316 0.113553 0.485640 0.046657 0.337942 0.043212 0.102491 0.096016
 [73] 0.106515 0.041353 0.113340 0.041656 0.026321 0.238589 0.077906 0.113340 0.041656 0.026321 0.238589 0.077906 0.055450 0.524933 0.224649 0.971180 0.485564 0.199426
 [91] 0.117308 0.143762 0.213338 0.185589 0.399255 0.084665 0.062968 0.100582 0.571910 0.387482 0.511154 0.092348 0.089989 0.412294 0.051212 0.648976 0.252705 0.693810
[109] 0.617963 0.119892 0.030029 0.081432 0.038687 0.033214 0.112379 0.063175 0.000000 0.110344 0.167776 0.163683 0.032663 0.023746 0.125402 0.045531 0.045795 0.103047
[127] 0.449417 0.107237 0.428094 0.039401 0.351426 0.135590 0.407135 0.100230 0.039368 0.008008 0.200829 0.261199 0.076530 0.232718 0.085286 0.026555 0.168105 0.048152
[145] 0.243847 1.896090 0.064978 0.173307 0.248775 0.305053 0.009760 0.022483 0.012606 0.017095 0.170162 0.048722 0.651938 0.234906 0.045130 0.014996 0.053357 0.357317
[163] 0.108373 0.036903 0.027245 0.032149 0.212627 0.153010 0.020654 0.154805 0.109319 0.256935 0.198258 0.179072 0.141050 0.378268 0.418901 0.091471 0.019409 0.212610
[181] 0.329002 0.281606 0.496554 0.072764 0.171546 0.219561 0.219255 0.500912 0.219234 0.351446 0.511151 0.111196 0.075369 0.128274 0.304799 0.130198 0.145957 0.053739
[199] 0.090025 0.095670 0.446649 0.077303 0.226425 0.154607 0.208172 0.317222 0.296694 0.241552 0.059364 0.149799 0.047185 0.023697 0.073052 0.313475 0.282652 0.049115
[217] 0.160275 0.098815 0.112587 0.059826 0.517693 0.100918 0.315041 0.524375 0.257371 0.605566 0.112452 0.414023 0.512370 0.011353 0.027922 0.060288 0.046126 0.107452
[235] 0.017059 0.184668 0.062810 0.288380 0.270547 0.028749 0.033927 0.144437 0.046057 0.156376 0.212820 0.194864 0.081697 0.177541 0.242288 0.020592 0.355854 0.118433
[253] 0.050759 0.070608 0.094731 0.112614 0.063008 0.107037 0.162462 0.142381 0.525066 0.652618 0.098654 0.160893 0.145006 0.145066 0.368863 0.159141 0.127407 0.143530
[271] 0.404888 0.038825 0.220179 0.174413 0.430015 0.165814 0.438100 0.310810 0.292658 0.719262 1.653700 0.109358 0.506372 0.422914 0.168032 0.123208 0.056045 0.000000
[289] 0.692415 0.026472 0.200836 0.845028 0.162533 0.058765 0.107596 0.025478 0.081980 0.142668 0.126040 0.063148 0.065822 0.100795 0.046335 0.061034 0.069405 0.094216
[307] 0.338985 0.187275 0.127531 0.076441 0.052407 0.347927 0.050306 0.575074 0.121199 0.914584 0.278406 0.014057 0.029463 0.209789 0.245484 0.376427 0.399126 0.399734
[325] 0.252252 0.106005 0.140380 0.111436 0.217695 0.103261 0.135960 0.222213 0.581169 1.049670 0.315957 0.105071 0.045994 0.998217 0.239790 0.129298 0.465007 0.051346
[343] 0.047176 0.256403 0.009185 0.013506 0.487307 0.019002 0.138520 0.112031 0.008995 0.607185 0.122582 0.068323 0.269293 0.068959 0.017179 0.053947 0.274963 0.178193
[361] 0.093676 0.285554 0.059339 0.193483 0.094907 0.169744 0.069887 0.268137 0.028538 0.204860 0.140179 0.019907 0.016430 0.084035 0.140333 0.450947 0.149573 0.082681
[379] 0.007441 0.070508 0.033843 0.060845 0.033175 0.112464 0.400036 0.529407 0.020445 0.064654 0.168163 0.040454 0.105573 0.057504 0.191750 0.749368 0.127492 0.137640
[397] 0.387096 0.218832 0.412083 0.306196 0.438376 0.248146 0.298699 0.083570 0.304285 0.250740 0.258930 0.061310 0.740408 0.045949 0.599082 0.597691 0.139838 0.030203
[415] 0.092448 0.069947 0.597690 0.296061 0.118092 0.037170 0.362598 0.840848 0.173205 0.083477 0.283058 0.209558 0.115193 0.166494 0.096769 0.157922 0.123588 0.177671
[433] 0.450138 0.114791 0.267911 0.263550 0.181169 0.075857 0.148144 0.090576 0.190295 0.045028 0.331226 0.041040 0.566679 0.141889 0.205783 0.484785 0.121332 0.020937
[451] 0.161654 0.089834 0.020558 0.363393 0.256428 0.031363 0.124260 0.088459 0.123073 0.424827 0.127439 0.114335 0.060644 0.163755 0.213012 0.325467 1.209370 0.169911
[469] 0.209834 0.377099 0.327387 0.412131 0.391615 0.219340 0.476027 0.025284 0.178303 0.598500 0.044186 0.171721 0.209712 0.027561 0.026320 0.019666 0.199979 0.410015
[487] 0.038802 0.095992 0.279883 0.566309 0.067527 0.197034 0.105282 0.064056 0.101378 0.066569 0.093195 0.057485 0.038071 0.116995 0.135058 0.045977 0.034085 0.293031
[505] 0.434328 0.136232 0.090732 0.076010 0.103591 0.358678 0.025195 0.101990 0.197562 0.393382 0.030196 0.769176 0.298321 0.232345 0.840950 0.141724 0.234347 0.153653
[523] 0.316143 0.267491 0.338357 0.160673 0.073814 0.040257 0.030107 0.182921 0.026122 0.185665 0.257160 0.063743 0.078600 0.403326 0.243881 0.224970 0.048106 1.172550
[541] 0.099247 0.327328 0.318161 0.066932 0.092312 0.087576 0.234746 0.247646 0.018241 0.022529 0.132139 0.045483 0.040499 0.600164 0.089454 0.018300 0.618036 0.280335
[559] 0.260020 0.643168 0.194155 0.522012 0.194403 0.764924 0.812531 0.161759 0.250682 0.236966 0.024373 0.312280 0.221233 0.118835 0.091133 0.597442 0.098854 0.039943
[577] 0.311993 0.493128 0.515409 0.205200 0.167472 0.075340 1.408460 2.559370 0.081771 0.137557 0.273087 0.358731 0.100109 0.179269 0.090918 0.127636 0.054635 0.107154
[595] 0.069724 0.089296 0.073163 0.045143 0.042763 0.327095 0.168808 0.598385 0.053705 0.111190 0.061892 0.237672 0.146158 0.108997 0.062747 0.110406 0.119472 0.023601
[613] 0.157626 0.043865 0.046448 0.105064

Statistische Masszahlen:

Zusammenfassende mit der 'summary()'
   Min. 1st Qu.  Median    Mean 3rd Qu.    Max.
0.00000 0.07037 0.14140 0.21510 0.28190 2.55900

Mittelungsmasse mit 'mean()' u. 'median()'
 Mittelwert = 0.2151434
 Median = 0.141387

Lokalisationsmasse - Quantile mit den kumulativen Wahrscheinlichkeiten:
Quantile von p = (0, 0.25, 0.5, 0.75, 1.0) mit 'quantil()'
        0%        25%        50%        75%       100%
0.00000000 0.07036775 0.14138700 0.28186750 2.55937000

Streuungsmasse mit 'sd()', 'var()' u. 'IQR()':
 Standardabweischung = 0.2352319
 Varianz = 0.05533405
 IQR = 0.2114998

Empirische Verteilungsform: die Schiefe u. der Exzess:
 Schiefe = 3.643456
 Exzess = 23.42752

Haeufigkeitsverteilungen durch Funktionen 'hist()', 'plot()', 'lines()', 'density()', 'rug()', 'ecdf()':

Stamm und Blatt Diagramm durch die Funktion 'stem()'

  The decimal point is 1 digit(s) to the left of the |

   0 | 00111111111222222222222222222222333333333333333333333333334444+301
   2 | 000000001111111111112222222222333333344444444555555556666666666+62
   4 | 000000011111122233334455557888999990001111222223377788 9
   6 | 00000001122455559922456 7
   8 | 144517
  10 | 057
  12 | 1
  14 | 1
  16 | 5
  18 | 0
  20 |
  22 |
  24 | 6


Die graphische Form von beschreibenden Statistiken 'boxplot()'
>
```

Figure 52: R output file of the stable blocks of zone one part two

Hence, we obtained the statistic distribution of the mean, the quantiles with the cumulative probabilities, the standard deviation, the variance and the interquartile range (IQR). Additionally, we displayed the values of each zone in boxplots (Figure 53 to Figure 56). Then, we listed all results in Table 10 and Table 11.

5.4.2 Volume and Apex Distributions of the Rock Blocks

Zone 1

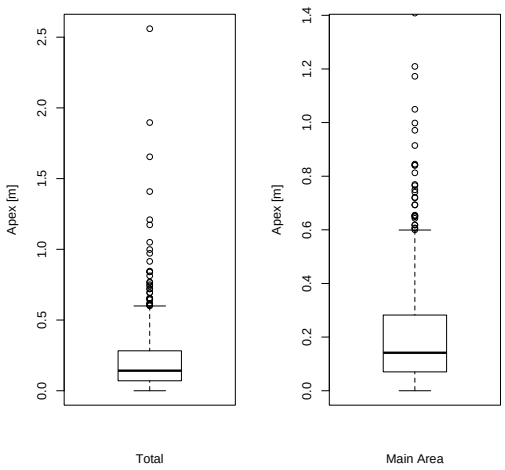

Zone 2

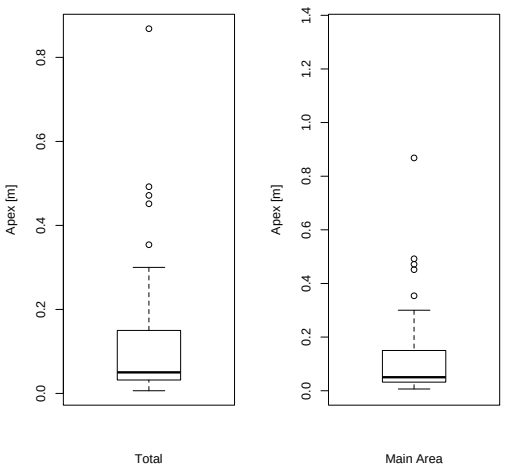

Zone 3

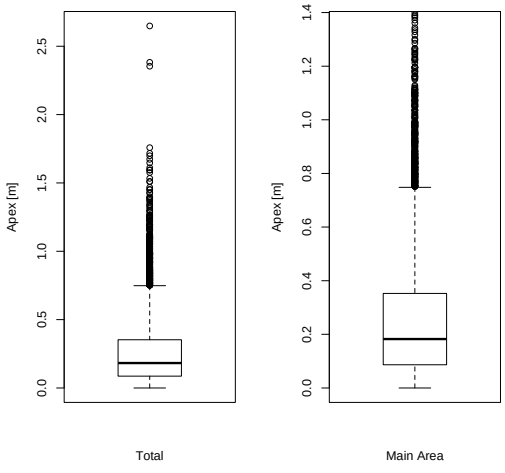

Zone 4

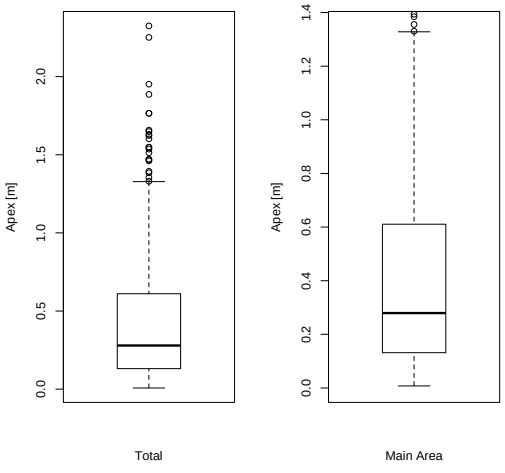

Figure 53: Apex boxplots of the stable blocks

Zone1

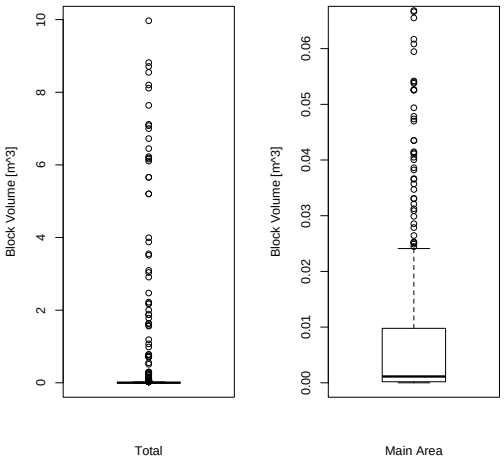

Zone 2

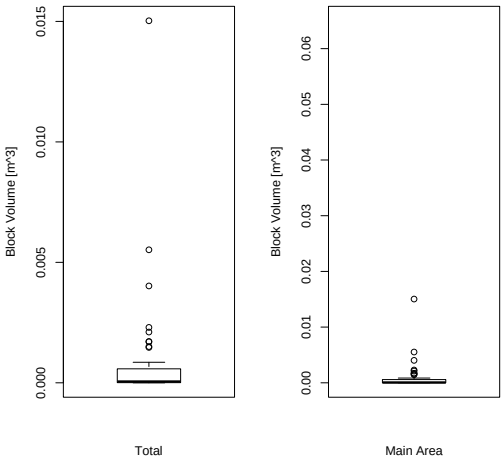

Zone 3

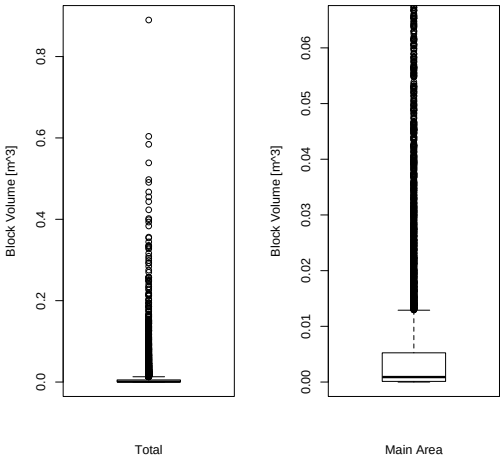

Zone 4

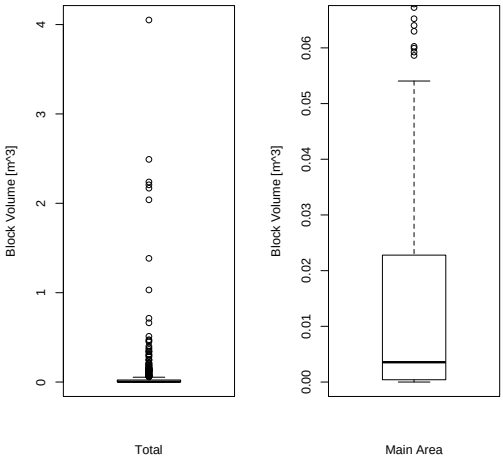

Figure 54: Volume boxplots of the stable blocks

Zone 1

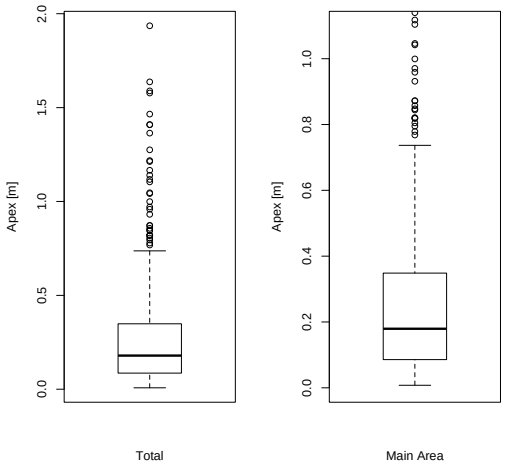

Zone 2

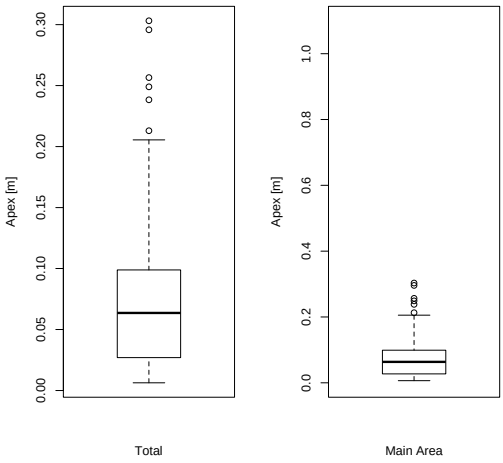

Zone 3

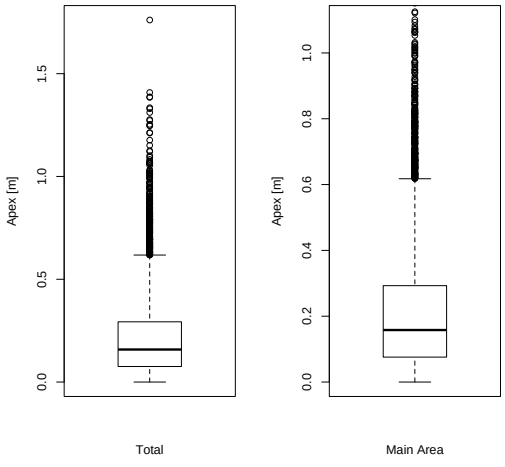

Zone 3

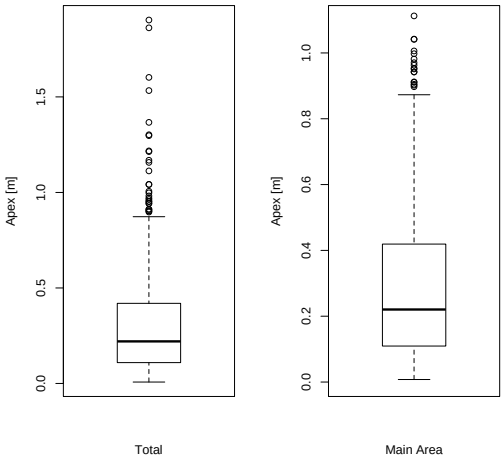

Figure 55: Apex boxplots of the unstable blocks

Zone 1

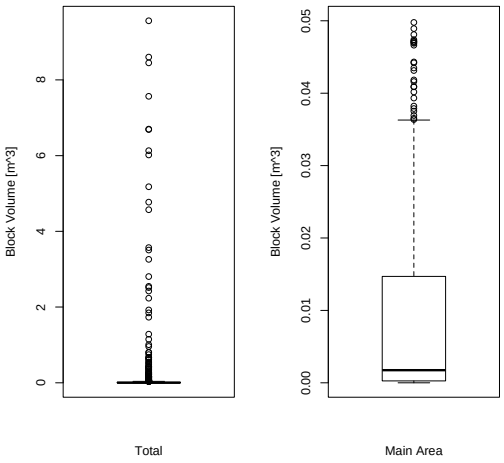

Zone 2

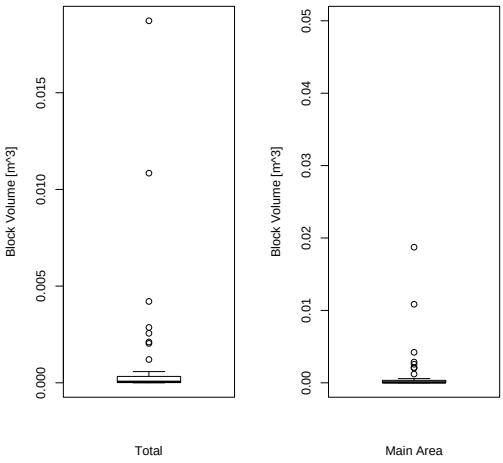

Zone 3

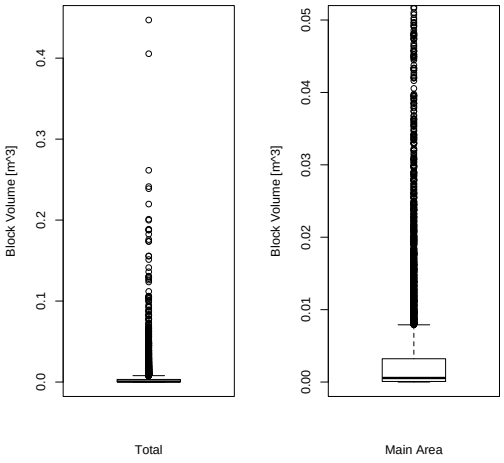

Zone 4

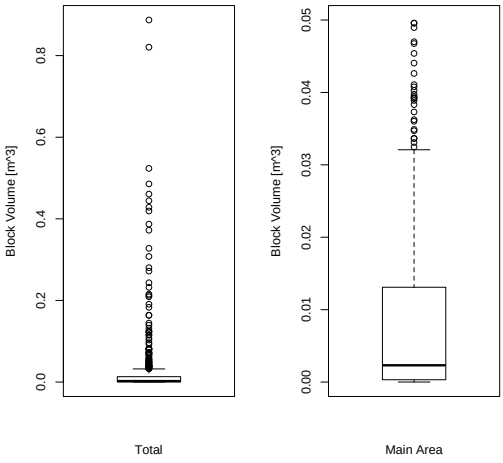

Figure 56: Volume boxplots of the unstable blocks

Table 10: Statistical values of the block volume [dm^3] (max.: maximum, sd: standard deviation; Var.: variance, IQR: interquartile range)

Zone	stable/ unstable	1st Quantile at 25%	Median	Mean	Max.	sd	Var.	IQR
1	stable	0.2	1.1	330.2	9968.0	1333.6	1778.5	9.6
1	unstable	0.3	1.7	219.6	9562.0	1012.1	1024.3	14.4
2	stable	0.0	0.1	0.8	15.0	2.2	0.0	0.5
2	unstable	0.0	0.0	0.9	18.7	2.9	0.0	0.3
3	stable	0.1	0.9	9.8	889.8	34.0	1.2	5.1
3	unstable	0.1	0.6	5.1	447.0	17.1	0.3	3.1
4	stable	0.4	3.6	62.9	4051.0	283.0	80.1	22.4
4	unstable	0.3	2.3	27.3	887.1	85.1	7.2	12.8

Table 11: Statistical values of the block apex [cm] (max.: maximum, sd: standard deviation; Var.: variance, IQR: interquartile range)

Zone	stable/ unstable	1st Quantile at 25 %	Median	Mean	Max.	sd	Var.	IQR
1	stable	7.0	14.1	21.5	255.9	23.5	5.5	21.1
1	unstable	8.6	17.9	26.6	193.6	27.5	7.6	26.3
2	stable	3.3	5.0	11.7	86.8	15.7	2.5	11.6
2	unstable	2.7	6.4	8.2	30.3	7.8	0.6	7.1
3	stable	8.6	18.2	25.5	264.8	23.7	5.6	26.6
3	unstable	7.6	15.8	21.7	176.1	19.7	3.9	21.7
4	stable	13.2	27.9	42.0	232.4	39.9	15.9	47.8
4	unstable	10.9	22.0	31.7	190.2	29.6	8.8	31.0

To point out the differences between the statistical values we visualized the results in a point diagram with interpolated lines shown in Figure 57 to Figure 68. In all visualisations of stable and unstable blocks, we can see that zone two shows the lowest statistical apex and volume values. Further zone three has the highest amount of outliers compared to the other zones. Zone one actually shows the maximum apex and volume. The other maximum statistical values vary between zones one and four. Therefore, the median, the interquartile range, the mean, the standard deviation, the variance and the quantile at 25 % of the stable and unstable blocks reach a maximum apex in zone four. The mean, the standard deviation and the variance of the stable and unstable blocks also have a maximum volume in zone four. In contrast, the median, the interquartile range and the quantile at 25 % have the highest volumes in zone one.

5.4.2.1 Volume Statistics

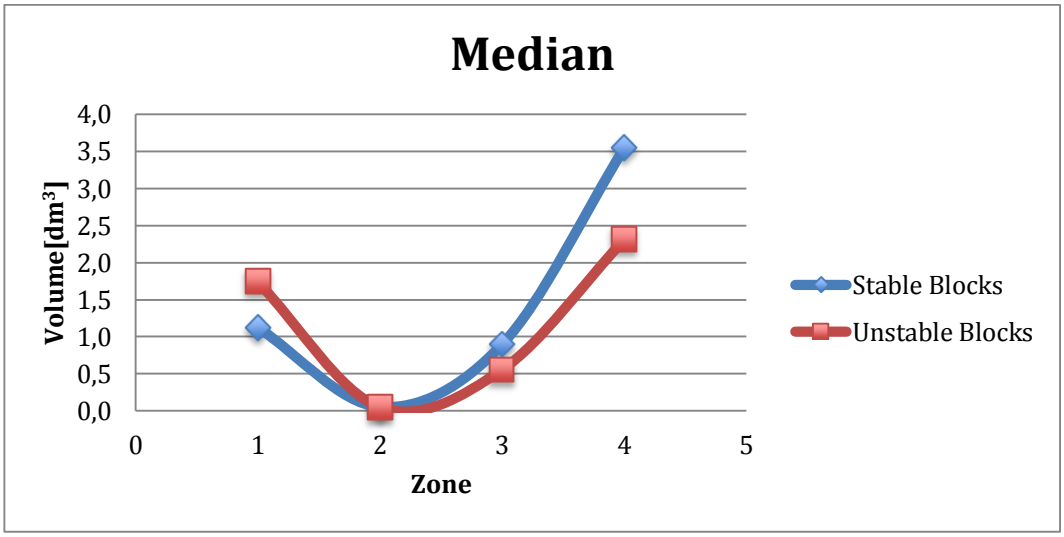

Figure 57: Volume median of the rock blocks

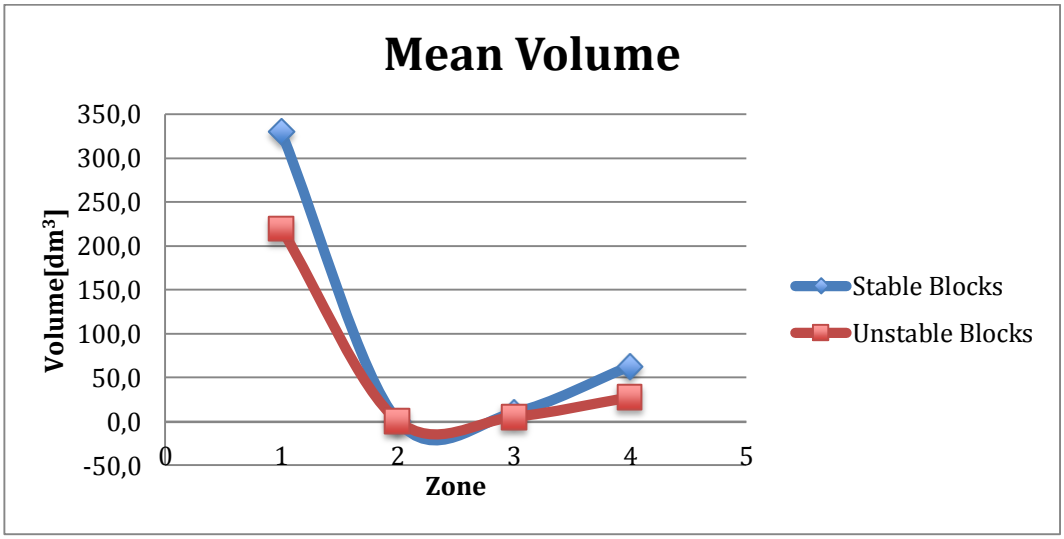

Figure 58: Mean volume of the rock blocks

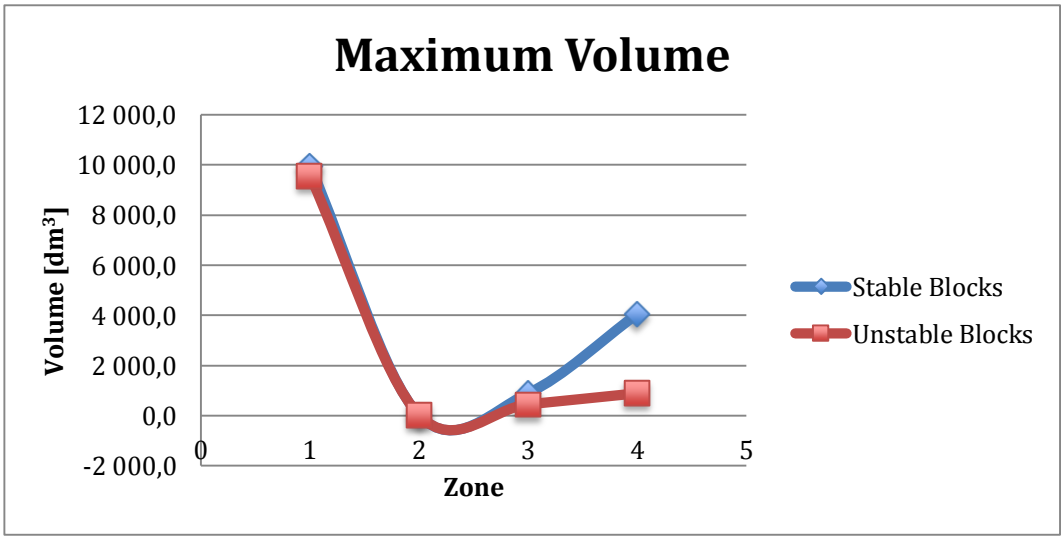

Figure 59: Maximum volume of the rock blocks

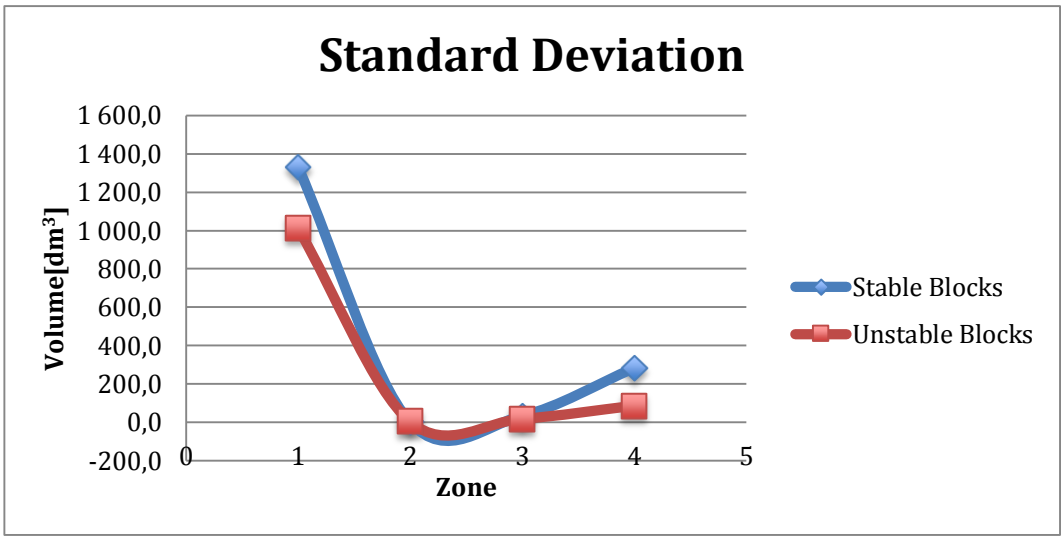

Figure 60: Standard deviation of the volume of the rock blocks

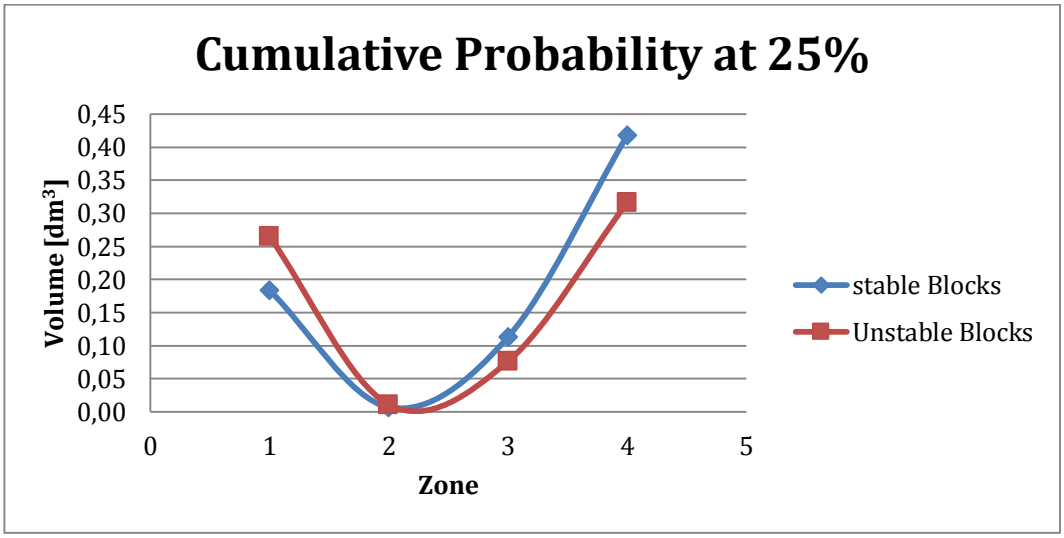

Figure 61: Volume quantile at 25%

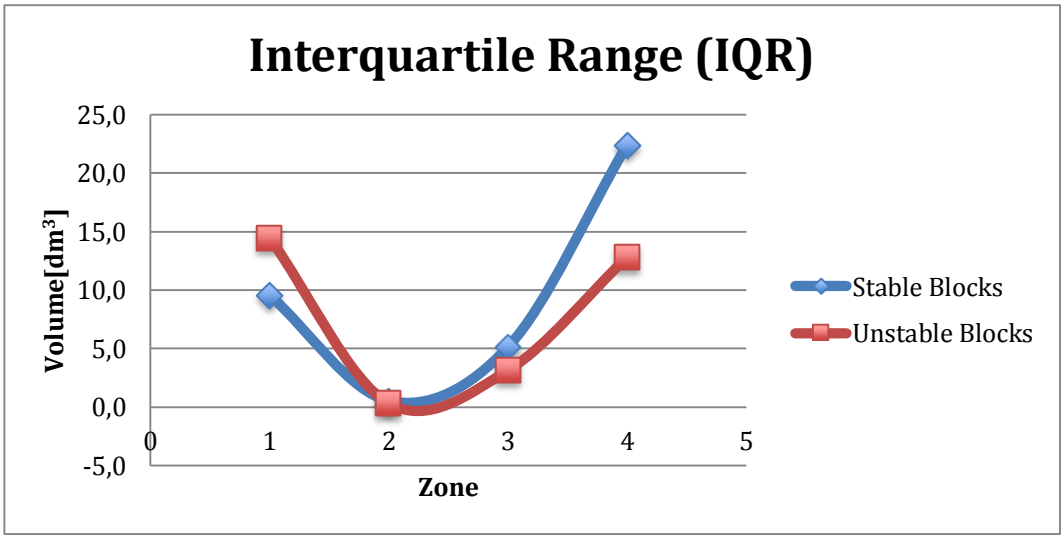

Figure 62: Interquartile range of the volume of the rock blocks

5.4.2.2 Apex Statistics

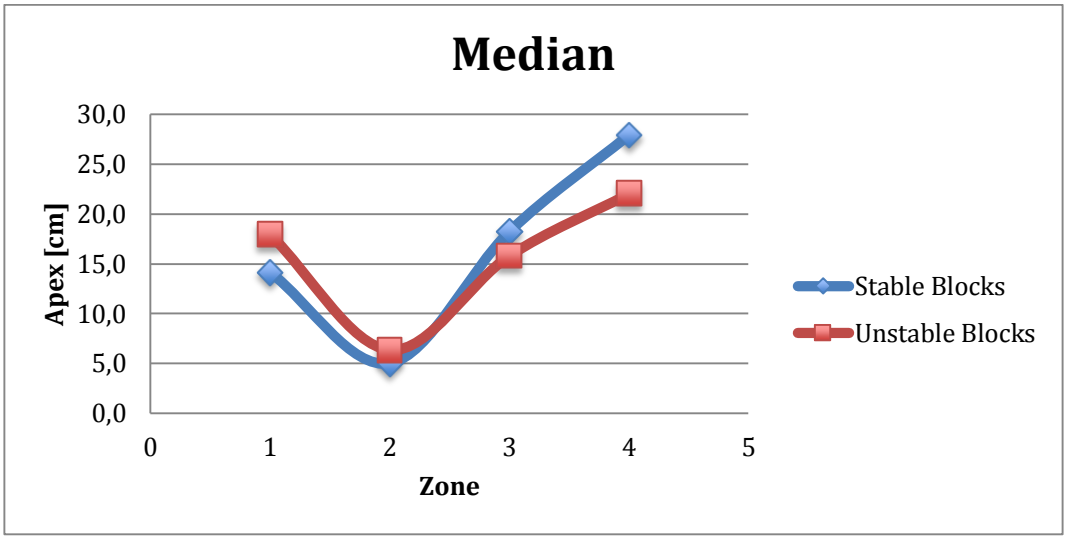

Figure 63: Apex median of the rock blocks

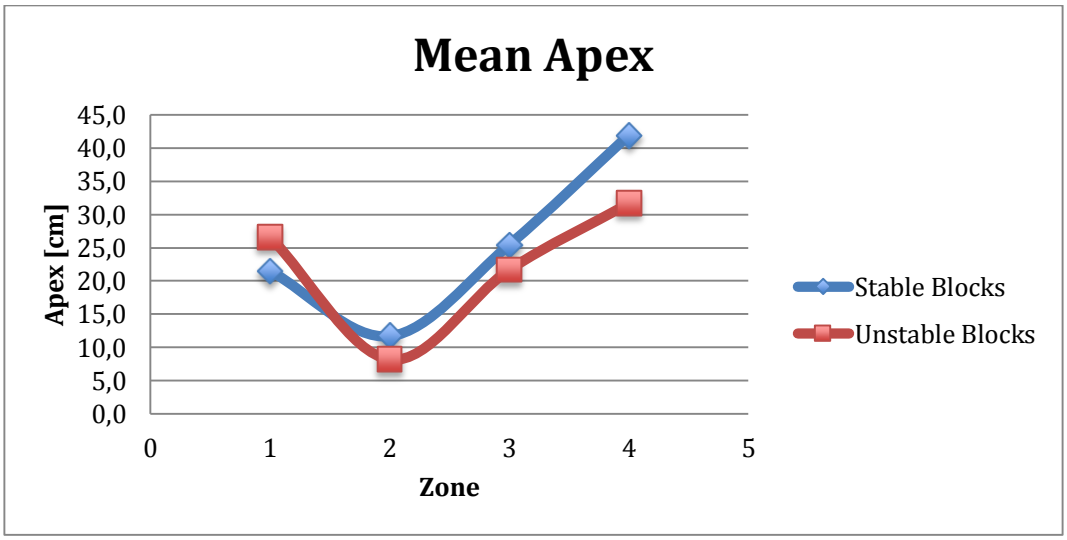

Figure 64: Mean apex of the rock blocks

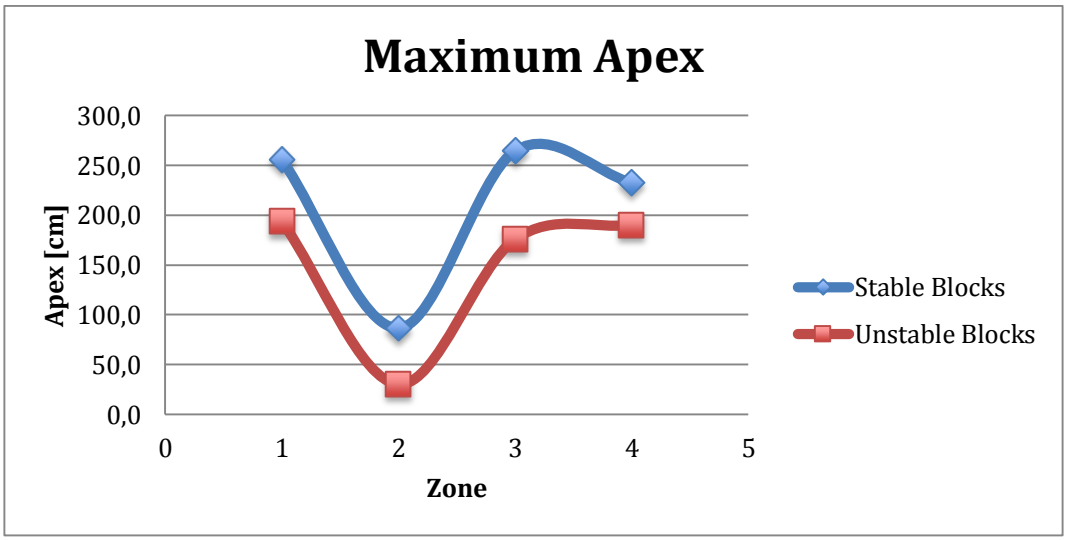

Figure 65: Maximum apex of the rock blocks

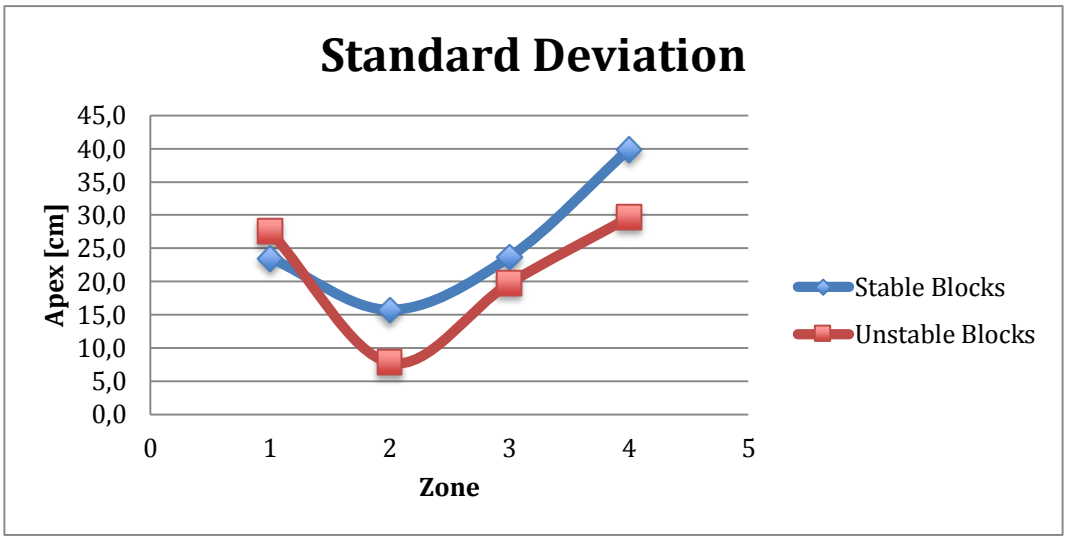

Figure 66: Standard deviation of the apex of the rock blocks

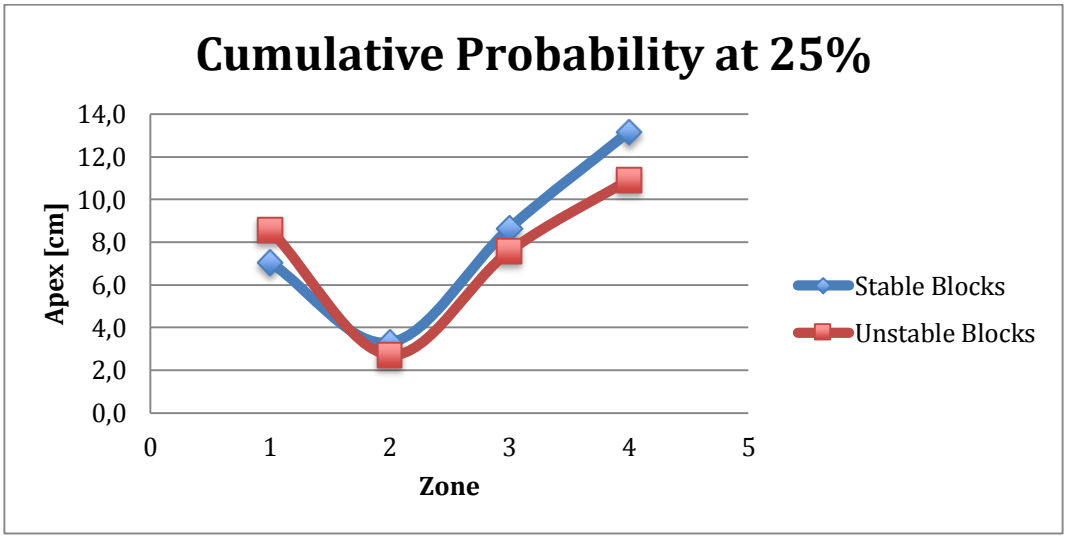

Figure 67: Volume quantile at 25%

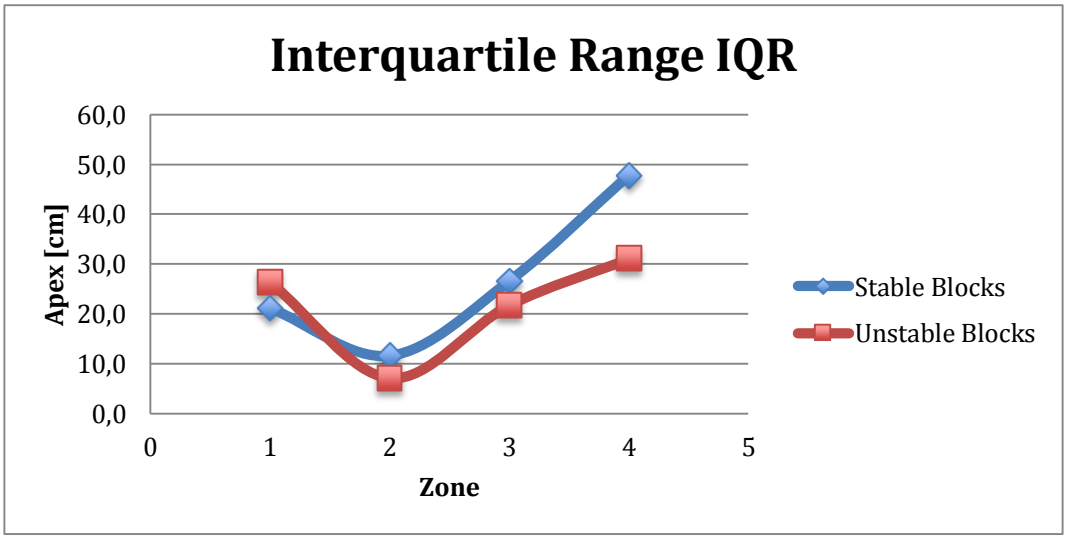

Figure 68: Interquartile range of the apex of the rock blocks

6 Discussion

We modelled three-dimensional fracture systems of the surrounding rock mass in the region of the exploratory tunnel Paierdorf, which is located on the western side of the Koralm near the Tertiary brittle Lavanttal fault system, to characterise rock mass. Therefore, we analysed the rock mass in the region and identified four homogeneous zones based on similarities in lithology, fracture orientation pattern, fracture intensity and -size. Within these zones, we carried out a static rock wedge analysis with the computer software program FracMan. Our results are presented and visualized in chapter 5. Additionally, we will compare the results, point out the similarities as well as the differences, and identify general trends.

First, what are the most important steps of data preparation, processing, evaluation and analysis? Thus, why were they carried out in such a manner? At the beginning, we made intensive desk studies to become an overall impression of the geological and tectonical situation in the exploratory are. Afterwards we started our intensive borehole image analysis. First, we did a kind of data clustering. That means we started to investigate rock mass parameters e.g. lithology, fracture orientation, -apertures, -trace length and -intensity. The purpose of this classification was that we needed the parameters for the modelling of the three-dimensional fracture systems. We obtained the fracture position, -size, -intensity and -network in 3D through discrete fracture network modelling (Liu, 2012). Further, we deceived the volume and the size of the distinct blocks. Afterwards, we processed the gathered results and started the evaluation with the computer software R.

What was our first evaluation result? It was the estimation of the lithology and the results are shown in Table 1. We started with the lithology because of their high importance in rock mass classification. In the first 1052 explored meters, the main rock type is schistgneiss. From the station in 2550 m to the station in 3743 m, the main lithology is micaschist. Marble and micaschist dominate the last explored 309 meters. Further rock types are amphibolite, quartzite and different gneiss types. Marble-, quartz- and calcite bands as well as cataclasitic and clay covered discontinuity planes partially occurred along the exploratory region. From the station in 2765 m, folding structures appear and become more and more intensive to the east.

Which part of the evaluation process took the longest? Our completed orientation studies because every single fracture had to be analysed in detail. Further, the subdivision into distinct discontinuity classes took much time. The results are represented in Figure 29. The visualisation shows that we have two perceivable schistosities. Schistosity one is trending to the southeast and schistosity two is trending to the northeast. Additionally, we found four conjugated joint sets. Therefore, joint set one is trending to the southwest or rather to the south-southwest, joint set two to the northeast or rather to the east-northeast, joint set three to the southeast and joint set four to the northwest or rather to the west-northwest. Subsequently, we have also found a fault set trending to the southwest. We analysed the orientation pattern of the different zones and assigned them to the six tectonic regimes after Pischinger et al. 2007 described in chapter 3.3. Therefore zone one shows orientation pattern signifying NNW-SSE compression in the Karpatium (<18 Ma) (D1-1). Late Karpatian to early Badenian (17-16 Ma) E-W-directed extension (D2) caused orientation pattern were found in all zones but mainly in zones two and three. In zone four the orientation patterns also signify Sarmatian/Pannonian (13-10 Ma) NE-SW compression (D3-1) and additionally marks of Pliocene (9-6 Ma) E-W compression (D4).

How did we receive the classification of the homogeneous zones shown in Table 6, Table 7 and Table 8? Hence, we looked at the lithology, the orientation, the intensity, the volumetric fracture density P_{32}, the concentration, the equivalent radius, the length of advance and further parameters to define the homogeneous zones. In addition, we can see that all fracture sets show a remarkably high volumetric fracture density in zone three. A purpose for this may be the high intensive folding structures in the region. The depth of advance is 2.2 m in the mentioned area and therefore signifies a good rock quality. That may be the reason why we have a high number of rock blocks in zone three, fortunately with a low volume and apex. Zones one and four show similar volumetric fracture densities (P_{32}) of the schistosity planes and have the same depth of advance. Contrary, the volumetric fracture densities of the joint planes and the equivalent radii are different. Therefore, the volumetric fracture density is higher in zone one but the equivalent radius is higher in zone four. Further, both zones have fault zones with low volumetric fracture densities and high equivalent radii. That may be the reason why both zones have a similar number of stable and unstable rock blocks with a similar apex and volume. Zone two shows the lowest values in all categories, the purpose of this is a massive rock mass and a small number of fractures with a low trace length.

What can be said about the stability in each zone? To become an impression about the rock mass behaviour with regard to the stability, we established the stable and unstable blocks of each zone. Table 12 shows the results of our studies of the unstable blocks. Therefore, we received the maximum block number in zone three, which depends on noticeable fracture intensity with a high trace length. Contrary, the volume with 9.56 m^3 and the apex with 1.94 m are on a maximum in zone one but neither is the trace length. That depends on the poorer rock quality of the rock mass near the Lavanttal fault. In contrast, the rock quality in the crystalline region is better. Hence, the trace length increases from the west to the east and more blocks could be built. However, the rocks in the crystalline basement are thickly bedded to massive and slightly jointed. Fortunately, the schistosity has just low mechanical effects and most of the discontinuities are healed. In regions with partly open joints weathering like discoloured discontinuity surfaces, alteration of rock material and reduction of rock strength occur. Problems may be caused by local faults or fractured zones and rock bursts in sections with massive rock and high overburden.

Zone	Max. Volume [m^3]	Max. Apex [m]	Total Blocks	Total Composite Blocks
1	9.56	1.94	34	20
2	0.02	0.30	2	2
3	0.45	1.76	334	191
4	0.89	1.90	29	17

Table 12: Unstable block results

Summarized, the results of our investigations are satisfying and we can use them for a basic structural characterization of the rock mass. Additionally, this method could build a foundation for further investigations in the engineering geology sector. Hence, it is a very new method and therefore needs future development.

7 Conclusion

At the beginning of this thesis, we wanted to find a method to characterize rock mass based on imaging borehole analysis the subsequent modelling of three-dimensional fracture systems of the rock mass in the exploratory region Paierdorf. Actually, it has proved to be a promising approach for the determination of spatial fracture patterns. In comparison to the initial assumptions, the obtained results led to a more complex view of the rock mass quality and stability behaviour.

We started to examine the exploratory region through intensive desk studies and build up a basic geological model of the region. Further to obtain important knowledge of the geological and tectonic setting. Additionally, we wanted to identify common geological hazards and risks in the area.

To support the theory, we started with the main part, the prolonged studies of the imaging borehole measurements. First, we started to analyse the lithological differences in the exploratory area. Then, we characterized all fracture planes and divided them into three distinct classes (e.g. schistosity, joint and fault planes). Hence, the representation of the orientation data with the computer software Sphaira was very helpful. Afterwards we evaluated the most important fracture parameters, which are listed below:

- Orientation (Concentration)
- Volumetric fracture density (P_{32})
- Size (Equivalent Radius *Re*)
- Shape (Elongation)
- Distribution of the Equivalent Radius (*Re*)
- Termination percentage

Based on the obtained parameters we divided the exploratory region in four homogeneous zones. Then, we started to model three-dimensional fracture systems of each zone to characterize the stable and unstable rock mass in the area. We analysed the stability behaviour of the rock blocks with the computer software FracMan. The representation of the stable and unstable blocks in boxplots was implemented with the statistical computer software R.

Now a short description of the gained results follows. We obtained a maximum volume of 9.56 m^3 and a maximum apex of 1.94 m of the unstable blocks in zone one. A purpose for this may be that zone one is located near the Lavanttal fault system. It is a distinct northwest southeast trending tertiary fault zone dipping steeply towards the Lavanttal Tertiary basin (Steidl et al., 2001). Thus, the fracture intensity is higher near a fault zone and consequently the rock quality is deteriorated. An interesting result was that we also have an impressive maximum volume of 0.89 m^3 and an apex of 1.90 m of the unstable rock blocks in zone four and high schistosity intensities in zone three and four. That seems to be very surprising but the purpose for this may be that the trace length of the fractures are higher in a rock mass with a better quality. As a result, the better rock quality in the Koralm crystalline region provides lower mechanical effects of the schistosity planes. To this end, a rock failure in the area of zones three and four is more unlikely. Additionally, we analysed the tectonic setting in the exploratory area. Therefore, we compared our obtained orientation patterns to the results of neogene tectonic evolution studies in the area after Pischinger et al. 2007. Although the whole area shows remarkable signs of E-W extension, a NNW-SSE compression as well as NE-SW compression had left their marks. Orientation patterns signifying the Pliocene compression in E-W direction were also found in one zone.

In summary, we can say that the rock mass characterization method based on three-dimensional fracture system models represents an excellent support and supplement for other geological, geotechnical and mechanical investigations. Consequently, it is a first estimation of the rock mass behaviour based on a stability analysis with the software FracMan. Actually, it could build the fundamentals of a first risk and danger analysis and assessment. Unfortunately, a detailed rock mass characterization based on the international or regional standards could not be avoided but our method could be very helpful to improve the standard investigations.

8 Appendix

8.1 List of Figures

Figure 1: A three-dimensional display of a fault and a joint (Newman, 2007) 5
Figure 2: Types of fractures developed during experiments on rocks in the brittle field at increasing environmental pressure from A to D. (Kurz, 2011) 7
Figure 3: Estimated behaviour: a) tunnel below a fault b) fault crossing the tunnel axis c) tunnel above a fault (Daller et al., 1994) 8
Figure 4: The red circles indicate the piercing points and the yellow arrow shows the offset (slip vector) (Martel, 2011). 9
Figure 5: Explanation of a strike-slip fault (Martel, 2011) 9
Figure 6: Explanation of dip-slip faults (Martel, 2011) 10
Figure 7: Explanation of an oblique fault (Myers, 2010) 10
Figure 8: Plate boundaries and their sense of motion illustrating plate tectonic processes (U.S. Geological Survey, 2004) 11
Figure 10: A part of the geological overview map of the republic of Austria enlarged by a factor of 500 000 (Geologische Bundesanstalt, 2014) 15
Figure 11: Chart of the deformation regimes D1-1 and D1-2 (Pischinger et al., 2007) 16
Figure 12: Chart of the deformation regime D2 (Pischinger et al., 2007) 16
Figure 13: Chart of the deformation regimes D3-1 and D3-2 (Pischinger et al., 2007) 17
Figure 14: Chart of the deformation regime D4 (Pischinger et al., 2007) 17
Figure 15: Overview of a part of the Pontebbana axis with the Koralm railway between Graz and Klagenfurt (Harer, 2009) 18
Figure 16: 3D model of the exploratory region “Stullneggbachgraben” (brown: gneiss-micaschist, dark red: “Plattengneis”, red: faults, blue: “Stullneggbach) (Harer & Otto, 1999) 19
Figure 17: FracMan chart of the axis of the exploratory tunnel Paierdorf with the eleven predrillings from the west to the east. 20
Figure 18: Kinematic Discontinuity Analysis results carried out by Vanek et al., 2001 21
Figure 19: left: Final 3D geological model of the Koralm, right: western, fault bounded transition zone between the crystalline basement and the Tertiary basin (Harer, 2009) 22

Figure 20: (left) VB-09/08: schistosity plane pole point projection and concentration at a confidence level of 95% (right) according statistic parameters (e.g. confidence level, data number, degree of preferred orientation, concentration, cone of confidence, spherical aperture, high density region, eigenvalue, eigenvectors and the distribution of cylindricity and small circle arrangement) 23
Figure 21: Simplified depiction of the equivalent radius (Liu, 2012)..... 26
Figure 22: The main features of a boxplot (Hawkins et al.) 29
Figure 23: VB-UT 02/09 image of an optical borehole measurement (AZI.: Azimuth (drilling direction refers to geographic north), INC.: Inclination (borehole inclination refers vertically). OBI.: Optical Borehole Imager, ABI.: (Acoustic Borehole Imager), TIME.: ABI, run time, STRUKTUR.: , discontinuities from OBI/ABI, (with reference to the borehole axis, no correction) classification: green: bedding or foliation planes, magenta: indefinite, POLAR: polar diagram (Schmidt net southern hemisphere)) 33
Figure 24: Geological documentation of the 3G geotechnical group in the exploratory tunnel Paierdorf at Station: 1.502,60 m, investigated in predrilling VB-UT09/08, (GA: rock mass type; SF: schistosity; ST: fault; H: slickenside; K: joint)..... 34
Figure 25: VB-UT 01/09, Stereographic projections (left) the results of the geological documentation of the 3G geotechnical group (green: schistosity, dark red: joints, purple: joint set one, yellow: joint set two, pink: joints set three, dark blue: slickenside, light blue: slickenside 1, bluish green: slickenside is equal to schistosity, light red: faults); (right) our first results (green: schistosity, red: joints) 34
Figure 26: VB-UT 01/09, (left) Fracture pole projection received from the geological documentation of the 3G Geotechnical group (green: schistosity, dark red: joints, purple: joint set one, yellow: joint set two, pink: joints set three, dark blue: slickenside, light blue: slickenside 1, bluish green: slickenside is equal to schistosity, light red: faults); (right) Our fracture pole projection results (green: schistosity, red: joints) 35
Figure 27: Pole projections of all exploratory predrillings from the west to the east (red: joints, green: schistosity) 36
Figure 28: Contour line projections of the schistosity planes in all exploratory predrillings from the west to the east, produced with the software program FracMan. 37
Figure 29: Great circle and pole point projections of the homogeneous oriented zones one to four (dark red: joints, light red: faults, green: schistosity) 38
Figure 30: FracMan representation of the tunnel axis with all eleven exploratory predrillings from the west to the east..... 39
Figure 31: FracMan representation of the exploratory predrillings VB-UT 01/09 with their schistosity planes (green) and their joint planes (red) 40
Figure 32: Acoustical borehole image of the exploratory predrilling VB-UT 02/09. Discontinuity 715 is an open joint, which displays the approximate aperture of 2 centimetres. The measurement tool shows the aperture in pixels, which is

displayed in centimetres in Figure 33. (Lighter colours: dense, homogeneous polymetamorphic rock mass, Darker colours: opened single fractures and destrengthened zones (brittle) Classification: green: bedding or foliation planes, blue: joints POLAR: polar diagram (Schmidt net southern hemisphere))..... 41
Figure 33: Fracture apertures along the exploratory predrilling VB-UT 02/09 with a maximum peak at approximately 3,5 centimetres at a depth of approximately 170 meters..... 42
Figure 34: Fracture apertures along the exploratory predrilling VB-UT 10/09 with a maximum peak at approximately 4 centimetres at a depth of approximately 125 meters..... 42
Figure 35: Cumulative fracture frequency along the predrilling VB-UT 09/08..... 44
Figure 36: Cumulative frequency along the predrilling VB-UT 10/09..... 44
Figure 37: Cumulative schistosity frequency along the predrilling VB-UT 09/08..... 45
Figure 38: Cumulative schistosity frequency along the predrilling VB-UT 10/09..... 45
Figure 39: Cumulative joint frequency along the predrilling VB-UT 09/08..... 46
Figure 40: Cumulative joint frequency along the predrilling VB-UT 10/09..... 46
Figure 41: One-dimensional fracture intensity P10 along the exploratory region from the west to the east..... 47
Figure 42: Schistosity set with assumed volumetric fracture intensity and a scaled virtual tunnel in the region box 52
Figure 43: Fracture plane intersections on the simulated well in the region box 53
Figure 44: Final fracture sets and the scaled virtual tunnel..... 54
Figure 45: Tunnel simulation with stable (green) and unstable blocks (red) 55
Figure 46: Rock blocks statistics 55
Figure 47: A comparison of the block amount of all zones..... 56
Figure 48: A comparison of the composite block amount of all zones..... 56
Figure 49: R input file of the stable blocks of zone one part one 57
Figure 50: R input file of the stable blocks of zone one part two 58
Figure 51: R output file of the stable blocks of zone one part one 59
Figure 52: R output file of the stable blocks of zone one part two 60
Figure 53: Apex boxplots of the stable blocks..... 61
Figure 54: Volume boxplots of the stable blocks 62
Figure 55: Apex boxplots of the unstable blocks..... 63
Figure 56: Volume boxplots of the unstable blocks..... 64
Figure 57: Volume median of the rock blocks..... 66
Figure 58: Mean volume of the rock blocks..... 66
Figure 59: Maximum volume of the rock blocks..... 66
Figure 60: Standard deviation of the volume of the rock blocks..... 67
Figure 61: Volume quantile at 25% 67
Figure 62: Interquartile range of the volume of the rock blocks 67
Figure 63: Apex median of the rock blocks..... 68
Figure 64: Mean apex of the rock blocks 68
Figure 65: Maximum apex of the rock blocks..... 68

Figure 66: Standard deviation of the apex of the rock blocks 69
Figure 67: Volume quantile at 25% 69
Figure 68: Interquartile range of the apex of the rock blocks..... 69

8.2 List of Tables

Table 1: Lithological classification 32
Table 2: One-dimensional fracture frequency P10 of all examined predrillings according to Figure 41 and homogeneous intensity zones (yellow: zone 1, green: zone 2, orange: zone 3 and blue: zone 4) 47
Table 3: Trace length of the schistosity planes (A_R: azimuth, FA: dip angle, l: fracture size; min.: minimum, max.: maximum) 48
Table 4: Trace length of the joint planes (A_R: azimuth, FA: dip angle, l: fracture size, min.: minimum, max.: maximum) 49
Table 5: Trace length of the fault planes (A_R: azimuth, FA: dip angle, l: fracture size, min.: minimum, max.: maximum) 49
Table 6: Homogeneous zones schistosity: (yellow: zone1, green: zone 2, orange: zone 3, blue: zone: 4), (A_R: azimuth, Φ: dip, P_{32}: volumetric fracture density, Re: equivalent radius) 50
Table 7: Homogeneous zones joints: (yellow: zone1, green: zone 2, orange: zone 3, blue: zone: 4), (A_R: azimuth, Φ: dip, P_{32}: volumetric fracture density, Re: equivalent radius) 50
Table 8: Homogeneous zones faults: (yellow: zone1, green: zone 2, orange: zone 3, blue: zone: 4), (A_R: azimuth, Φ: dip, P_{32}: volumetric fracture density, Re: equivalent radius) 50
Table 9: Assumed P_{32}* values of the different fracture types (P_{32}*: assumed volumetric fracture density) 52
Table 10: Statistical values of the block volume [dm^3] (max.: maximum, sd: standard deviation; Var.: variance, IQR: interquartile range) 65
Table 11: Statistical values of the block apex [cm] (max.: maximum, sd: standard deviation; Var.: variance, IQR: interquartile range) 65
Table 12: Unstable block results 73

8.3 List of References

ÖBB Infrastruktur AG. (2014). ÖBB INFRA. Retrieved: October 2014 from http://www.oebb.at/infrastruktur/de/

Aßmann, K., Dörrer, T., Lehmann, B., Lux, K.-N., Seren, S., & Schön, J. (2001). Geophysical Investigations at differnet Parts of the planned Koralm Tunnel. Felsbau 19 .

British Geological Survey. (2014). BGS. Retrieved: July 2014 from British Geological Survey: http://www.bgs.ac.uk/home.html?src=topNav

Brosch, F., Pischinger, G., Steidl, A., Vanek, R., & Decker, K. (2001). Improved site investigation results by kinematic discontinuity analysis on drill cores. (P. S. Elorante, Hrsg.) Espoo, Finland: Taylor & Francis.

Brosch, F.-J. (2011). Engineering Geological Investigation, GEO.708. Graz, Styria, Austria: University of Technology.

Brosch, F.-J. (2011). Rock Mass Characterization, GEO.710. Graz, Styria, Austria: University of Technology.

Burg, J.-P. (2011). Einführung in die Strukturgeologie. Zürich: Eidgenössische Technische Hochschule Zürich, Geologisches Institut.

Dörrer, T., Harer, G., Lehmann, B., Lux, K.-N., Riedmüller, G., Schön, J., et al. (2000). Combined Application of geophysical Measurements - Case History Koralm Tunnel. Felsbau 18.

Daller, J., Riedmüller, G., & Schubert, W. (1994). Zur Problematik der Gebirgsklassifizierung im Tunnelbau. 12. (Felsbau, Hrsg.)

Dershowitz, W., & Carvalho, J. (1996). Key-Block Tunnel Stability Analysis using realistic Fracture Patterns in Rock Mechanics Tools and Techniques Proceedings of the 2nd North American Rock Mechanics Symposium: NARMS´96. Montreal, Quebec, Canada.

Dershowitz, W., & Herda, H. (1992). Interpretation of Fracture Spacing and Intensity. Proceedings of the 33rd U.S. Symposium on Rock Mechanics. Santa Fe.

DSSC IRIS. (March 2014). Incorporated research Institutions for Seismology. Retrieved: October 2014 from http://www.iris.edu/hq/about_iris/governance/ds

Frisch, W., Dunkl, I., & Kuhlemann, J. (2000). Post-collosional orogen-parallel large-scale extension in the Eastern Alps. Tectonophysics .

Gentleman, R., & Ihaka, R. (1997). The R Project for Statistical Computing. (Statistics Departement of the University of Auckland) Retrieved: September 2014 from http://www.r-project.org

Geoconsult ZT GmbH. (2014). Koralmbahn Graz-Klagenfurt. Salzburg, Österreich.

Geologische Bundesanstalt. (2014). Geologische Bundesanstalt. Retrieved: September 2014 from http://www.geologie.ac.at/produkte-shop/karten/bersichtskarten_2/

Golder Associates Inc. (2010). FracMan® User´s Manual (Bd. 7.3). NE Union Hill Road Redmond, Washington, USA.

Graf, F., Kohl, T., Mégel, T., Rybach, L., & Fuchs, R. (2001). Hydraulic-Geothermal Modelling of Koralm Tunnel into Rock Mass Classification. Felsbau 19.

Harer, G. (2009). Koralm Tunnel - Benefits of a structured investigation process for a large tunnel project - the clients view. (Ö. -A. Railways, Hrsg.) Graz.

Harer, G., & Otto, R. (1999). Koralmtunnel: Methodische Erkenntnisse aus der Projektvorbereitung. Baugeologisches Seminar , 10 . (B. M. Schwaighofer, Hrsg., & F. P.-S. Hintermüller, Redakteur) Riegelnik Ges. m. b. H., Wien.

Harer, G., & Riedmüller, G. (1999). Assessment of ground condition for the Koralm tunnel during the early stages of planing. Felsbau 17.

Harer, G., & Vavrovsky, M. (1998). Hochleistungsstrecke Koralmbahn Graz-Klagenfurt.

Hawkins, D., Carter, T., & McCary, J. (2014). NuMBerS - numerical methods for biosciences students. Retrieved: September 2014 from http://web.anglia.ac.uk/numbers/project.html

Kurz, W. (2011). Upper crust structures, GEO.702. Graz, Styria, Austria: Karl-Franzens University.

Leitner, J. (2011). regionalentwicklung.at. Retrieved: September 2014 from http://www.regionalentwicklung.at/192-0-DEMO-WebMapping-Koralmbahn.html

Liu, Q. (2012). Modelling Engineering Geology, GEO.941. Graz, Styria, Austria: University of Technology.

Liu, Q. (2014). Rock Mass Characterization. Graz, Styria, Austria: University of Technology.

Liu, Q. (2012). Statistical Methods in Earth Sciences. Graz, Styria, Austria: University of Technology.

Loew, S., Barla, G., & Diederichs, M. (2010). Engineering geology of Alpine tunnels: Past, present and future. Taylor & Francis Group, London.

Mandl, G. (2005). Rock Joints-The Mechanical Genesis. Feldkirch, Austria: Springer.

Martel, S. J. (2011). Structural Geology. University of Hawaii at Manoa, School of Ocean and Earth Science and Technology, Hawaii.

Myers, J. D. (2010). GeoWeb. (D. o. Geophysics, Produzent, & University of Wyoming) Retrieved: July 2014 from http://www.gg.uwyo.edu

Newman, L. E. (2007). Crustal Deformation (folding/faulting) and Earthquakes. Retrieved: July 2014 from GPH 111 - Introduction to Physical Geography: http://web.gccaz.edu/~lnewman/gph111/topic_units/Fold_fault_eq/Fold_fault_eq2.html

Park, R. G. (2013). Foundations of Structural Geology. Routledge.

Pischinger, G., Kurz, W., Fritz, H., & Brosch, F. (2007). Neogene tectonic evolution of Austroalpine basement and the final uplift of "cold spots" in the eastern part of the Eastern Alps. (D. Alpine Workshop, Hrsg.)

Reichl, P., Probst, G., Erhard-Schippek, W., Goldschmidt, F., & Riepler, F. (2001). Initial hydrogeological and Hydrological Field Investigations for the Koralm Tunnel. Felsbau 19.

Riedmüller et al. (1998). Baugeologische Bewertung des Trassenkorridors Koralmtunnel - unveröffentlichtes Gutachten. (U. o. Institute of Applied Geology, Hrsg.)

Schmid, S., Fügenschuh, B., Kissling, E., & Schuster, R. (2004). Tectonic map and overall architecture of the Alpine orogen. Basel-Stadt, Schweiz: Birkhäuser.

Skalla. (1998). Auswertung der Kernbohrung KB-D0,2/98 Stullneggbachgraben, Koralm. (U. o. Institute of rock mechanics & tunneling, Hrsg.)

Steidl, A., Goricki, A., & Schubert, W. (2001). Geological and Geotechnical Ground Characterisation for the Koralm Tunnel Route Selection. Felsbau 19.

U.S. Geological Survey. (2004). USGS science for a changing world. Retrieved: July 2014 from http://geomaps.wr.usgs.gov/parks/pltec/vigilim.html

Vanek, R., Pischinger, G., & Brosch, F.-J. (2001). Kinematic Discontinuity Analysis - Results and Implications of Structural Geological Investigations on Drill Cores. Felsbau 19.

Vavrovsky, G., Schneider, K., & Harer, G. (2001). "Koralmbahn - A new Railway Line in the South of Austria". Felsbau 19.

Wallbrecher, E. (1986). Tektonische und gefügeanalytische Arbeitsweisen.

8.4 Geological map